Measurement of light isotopes ratios in the cosmic rays with the IMAX balloon experiment

DISSERTATION
zur Erlangung des Grades eines Doktors
der Naturwissenschaften

vorgelegt von
Dipl.-Phys. Dragoş Vasilas
geb. am 26 Juli 1973 in Râmnicu-Vâlcea (Rumänien)

eingereicht beim Fachbereich 7
der Universität Siegen

Siegen 2004

Gutachter der Dissertation: Prof. Dr. Manfred Simon
Prof. Dr. Claus Grupen

Datum der Disputation: 9. Juni 2004

Prüfer: Prof. Dr. Hans-Dieter Dahmen
Prof. Dr. Claus Grupen
Prof. Dr. Manfred Simon

Internetpublikation der Universitätsbibliothek Siegen: urn:nbn:de:hbz:467-803

Abstract

Diese Arbeit widmet sich der Messung der Wasserstoffisotopenhäufigkeit in der kosmischen Strahlung im Energiebereich von 0.2 bis 1.8 GeV/nuc. Die analysierten Daten stammen von dem Flug des Ballonexperimentes IMAX (Isotope Matter Antimatter eXperiment) vom 16-17 Juli 1992 in Lynn Lake, Kanada. Die Ergebnisse dieser Arbeit sollen einen zusätzlichen Beitrag zu den bereits vorhandenen Daten liefern, um so besser zwischen den heutigen Propagationsmodellen der galaktischen kosmischen Strahlung unterscheiden zu können. Dazu wurden in der Datenanalyse das $^2H/He$ und das $^2H/^1H$-Verhältnis bestimmt, weil nach dem heutigen Wissensstand angenommen wird, dass die kosmischen Deuteronen hauptsächlich aus Wechselwirkungen von Helium und Protonen mit dem interstellaren Medium stammen. Ein weiteres signifikantes Ergebnis dieser Arbeit ist das Verhältnis $^3H/^4He$, gemessen bei 5 $g \cdot cm^{-2}$ Restatmosphäre, da das gemessene Tritium rein sekundär überwiegend durch die Spaltung von Heliumkernen gebildet wird. Das gemessene Verhältnis kann dann als Test von theoretischen Berechnungen des atmosphärischen sekundären Tritium benutzt werden. Das Messprinzip von IMAX basiert auf der gleichzeitigen Bestimmung von Ladung, Geschwindigkeit und Steifigkeit der einfallenden Teilchen. Die Analyse der einzelnen Detektoren konzentriert sich in dieser Arbeit auf die Steifigkeitsbestimmung, die Kalibrierung der Flugzeitmessung und der Ladungsselektion. Um die Verhältnisse der leichten Isotope im Instrument zu erhalten, wird eine Instrumentsimulation durchgeführt. Nach weiteren instrumentellen und atmosphärischen Korrekturen der gemessenen Verhältnisse werden die so erhaltenen Ergebnisse am Rand der Atmosphäre mit den theoretischen Vorhersagen verglichen.

This thesis is dedicated to the measurement of hydrogen isotopic abundances in the cosmic rays with energies between 0.2 to 1.8 GeV/nuc. The data for the analysis discussed here were obtained during a high-altitude balloon flight of the Isotope Matter Antimatter eXperiment (IMAX), on 16-17 July 1992 from Lynn Lake, Canada. The results that this analysis aims to provide should enlarge the data basis for distinguishing among various models about galactic cosmic rays propagation. From this perspective, the deuteron-to-helium and deuteron-to-proton ratios are resolved from the flight data, as it is generally believed that the cosmic deuterons are mainly created from the interaction of the helium and proton nuclei with the interstellar medium. Another result of interest provided by this work is the ratio triton-to-helium, measured at 5 $g \cdot cm^{-2}$ atmospheric overburden. Tritium is considered as being produced in the atmosphere mainly from the spallation of helium nuclei. Thus, the $^3H/^4He$ ratio can serve as test for the present calculations about atmospheric secondary tritons. IMAX measurement technique employs a simultaneous determination of charge, velocity and magnetic rigidity. The analysis of the separate detectors is concentrated on rigidity determination, Time-of-Flight calibration and charge selection. Ratios of the light isotopes in the instrument are obtained by means of mass histograms simulations. Further instrumental and atmospheric corrections are applied to the measured ratios and the results at the top of the atmosphere are compared with predictions from theoretical models.

Contents

List of Figures i

List of Tables v

1 Introduction 1

2 The Isotope Matter Antimatter Experiment (IMAX) 4
2.1 Introduction 4
2.2 Spectrometer 7
2.2.1 Magnet 7
2.2.2 Drift Chambers 7
2.2.3 Multiwire Proportional Counters 11
2.3 Time-of-Flight System 12
2.4 Scintillator Counters 13
2.5 Cherenkov Counters 14

3 Mass Separation 16
3.1 Rigidity Determination 16
3.1.1 Position Measurement 16
3.1.2 Rigidity Determination using an Iterative Fitting Procedure 21
3.1.3 χ^2-Distribution 22
3.1.4 The Maximum Detectable Rigidity (MDR) 26
3.2 Velocity Measurement 30
3.2.1 The Time-of-Flight Measurement Principle 30
3.2.2 Time-of-Flight Calibration 35
3.3 Charge Separation 40
3.3.1 Charge Determination 40
3.3.2 Efficiency and Contamination of the Charge Selection . . . 49

4 Hydrogen Isotopic Ratios in the Instrument 53
4.1 Mass Resolution for Singly Charged Isotopes with IMAX 53
4.2 Influence of Track Quality and Geometry Cuts on the Isotopic Ratios 59
4.3 Simulation Inputs Based on the Detector Performances 68

4.4 Simulations of Mass Histograms 73
4.4.1 Simulation Using Deterioration Factors 73
4.4.2 D/P and T/P Ratios Determined with Deterioration Factors 75
4.4.3 Empirical Determination of Background Shapes 81
4.4.4 D/P and T/P Ratios Determined with a Simulation Using the Background Shapes 85

5 The Isotopic Ratios at the Top of the Atmosphere 89
5.1 Instrumental Corrections 89
5.1.1 Corrections due to Total Inelastic Interactions in the Instrument 90
5.1.2 Energy Loss Correction 93
5.1.3 Geometrical Factor of the Experiment 96
5.1.4 The Isotopic Ratios at the Top of the Instrument 97
5.2 Atmospheric Corrections 99
5.2.1 The Atmospheric Secondary Deuterons 99
5.2.2 Attenuation and Energy Loss Correction 101
5.2.3 The D/He_{tot} and D/P Ratios at the TOA 101
5.2.4 The Ratio $T_{TOI}/^4He_{TOA}$ 104

6 Conclusions 106

A Iterative Procedure for Determining the Rigidity 112

B Simulation-related Plots 115

C IMAX Detector Grammages 121

D Cross-Section Compilation 123

E Climax Neutron Monitor Flux 136

Acknowledgements 144

List of Figures

2.1 IMAX Payload schematics 6
2.2 IMAX magnetic field and isomagnetic lines 8
2.3 IMAX Drift Chamber 9
2.4 IMAX Drift Chamber cell structure 9
2.5 IMAX Drift Chamber cell electric field 10
2.6 Functioning principle of MWPCs 11
2.7 IMAX Time-of-Flight System (TOF) 12
2.8 IMAX Scintillator Counter S1 13
2.9 IMAX Scintillator Counter S2 14

3.1 Drift-time to Path scatter plot 17
3.2 Definition of the residual 18
3.3 Residual Distribution as a function of the drift path 19
3.4 Position resolution of IMAX Drift Chambers 20
3.5 The χ^2-distribution with degrees of freedom varying up to 16 . . . 23
3.6 The normalized χ^2-distribution with degrees of freedom varying up to 16 23
3.7 The usual and normalized χ^2 histograms for a) $N_x = 16$ and b) $N_y = 8$ 25
3.8 Distribution of the hit measurement layers 27
3.9 IMAX magnetic field integral 29
3.10 The sigma-deflection distribution for a sample of events with $R > 20\ GV$ 29
3.11 Schematical picture of IMAX TOF 31
3.12 The measurement principle of TOF 33
3.13 Difference-of-Sums scatter plot for paddle combination 2 35
3.14 Proton band from paddle combination 2, selected for the calibration line of TOF 37
3.15 Time resolution with the IMAX instrument for singly charged particles 38
3.16 Position resolution in the top-TOF 39
3.17 The energy loss in the scintillator S2 versus squared beta and squared deflection 42

3.18 Schematic representation of the interpolation for ascribing a "real" charge to an ADC measurement 43
3.19 Energy loss scatter plots used for charge sample determination . . 44
3.20 Scatter plots of energy loss scaled with squared beta used for determining charge samples 45
3.21 Samples chosen for charge bands fitting in all four scintillators . . 46
3.22 Charge histograms in all four scintillators 48
3.23 Charge efficiency in all four scintillators for protons with a charge cut $1 \pm 0.6\bar{e}$ 50
3.24 Contamination of the proton band with helium, in case of a charge cut $1 \pm 0.6\bar{e}$ in all four scintillators 51

4.1 Beta vs. rigidity representation for singly charged particles 54
4.2 Expected proton and deuterium mass resolutions vs. kinetic energy with the IMAX instrument 57
4.3 Singly charged mass histograms obtained with geometrical and position agreement cuts 60
4.4 Surviving fraction histograms obtained with χ^2_x cuts 62
4.5 Surviving fraction histograms obtained with χ^2_y cuts 63
4.6 Surviving fraction histograms obtained with N_x cuts 64
4.7 Surviving fraction histograms obtained with N_y cuts 65
4.8 Surviving fraction histograms obtained with $\sigma(\eta)$ cuts 66
4.9 Velocity distribution of singly charged particles in the IMAX instrument 69
4.10 Averaged position resolution for protons as a function of energy . 71
4.11 Normalized sigma-deflection distributions for high and low energies 71
4.12 Simulated sigma-deflection distribution for low energies 72
4.13 The analytical behavior of the α-factors 74
4.14 The α-factors of protons, deuterons and tritons 76
4.15 Determination of the ratio D/P and its error according to the χ^2-minimization method 77
4.16 The measured and simulated mass histograms using deterioration factors for the energy range $0.2 \div 1$ GeV/nuc 79
4.17 The χ^2 dependency on the ratio D/P of the simulated mass histograms for the energy range $200 \div 1000$ MeV/nuc 80
4.18 Background shape of the measured mass distribution for the energy bin $1000 \div 1200$ MeV/nuc. 84
4.19 The measured and simulated mass histograms using a simulation with background for the energy range $200 \div 1000$ MeV/nuc . . . 87
4.20 The measured and simulated mass histograms using a simulation with background for the energy range $1000 \div 1800$ MeV/nuc . . . 88

5.1 Spectral shapes of the proton, deuteron and triton fluxes measured in the instrument 90
5.2 Survival probability in the IMAX instrument for protons, deuterons and tritons 92
5.3 Dependence of the kinetic energy per nucleon in the middle of the instrument on the same quantity at the top of the instrument, in the case of protons, deuterons and tritons 94
5.4 Displacement of the energetic spectral shape of protons due to the energy loss correction 95
5.5 Geometrical factor of the IMAX experiment 97
5.6 Dependence of the kinetic energy per nucleon at the top of the instrument on the same quantity at the top of the atmosphere, in the case of deuterons 102

6.1 Differential energy spectrum of cosmic-ray deuterons measured by IMAX at the top of the atmosphere 107
6.2 D/He_{tot} ratio measured by IMAX at the top of the atmosphere . 108
6.3 D/P ratio measured by IMAX at the top of the atmosphere . . . 109
6.4 $T_{TOI}/^4He_{TOA}$ ratio measured by IMAX 110

B.1 The χ^2 dependency on the ratio D/P of the simulated mass histograms for the energy range $0.2 \div 1.0$ GeV/nuc 115
B.2 The χ^2 dependency on the ratio D/P of the simulated mass histograms for the energy range $1.0 \div 1.8$ GeV/nuc 116
B.3 The measured and simulated mass histograms using deterioration factors for the energy range $200 \div 1000$ MeV/nuc 117
B.4 The measured and simulated mass histograms using deterioration factors for the energy range $1000 \div 1800$ MeV/nuc 118
B.5 Background shapes of the measured mass distributions for the energy range $200 \div 1000$ MeV/nuc 119
B.6 Background shapes of the measured mass distributions for the energy range $1000 \div 1800$ MeV/nuc 120

D.1 Total reaction cross-sections for ^{1}H projectiles on ^{1}H,^{12}C,^{14}N and ^{16}O targets 130
D.2 Total reaction cross-sections for ^{1}H projectiles on ^{19}F,^{27}Al,^{28}Si and ^{40}Ar targets 131
D.3 Total reaction cross-sections for ^{1}H projectiles on ^{56}Fe and ^{63}Cu targets 132
D.4 Total reaction cross sections for deuterium projectiles on proton and carbon targets 134
D.5 Total cross sections for ^3H and ^3He projectiles on proton, carbon and aluminium targets 135

E.1 Climax Neutron Monitor Flux 136

List of Tables

3.1 Trigger configuration signals 30
3.2 Cuts used to select the protons for the calibration of TOF 36
3.3 Calibration constants for TOF 37
3.4 Efficiency and contamination for the charge cuts Z=1 52

4.1 Approximate vertical depth of the IMAX tracking detector 55
4.2 Set of investigated track quality cuts 61
4.3 The ratios deuteron-to-proton and triton-to-proton in IMAX instrument, determined with the fitting procedure using deterioration factors 77
4.4 Fractions of the data set representing the background for different energy bins 83
4.5 The deuteron-to-proton and triton-to-proton ratios in the IMAX instrument, determined with the simulation taking the background into account 86

5.1 The deuteron-to-proton and triton-to-proton ratios at the top of the IMAX instrument 98
5.2 The calculated fluxes of protons and deuterons, produced and attenuated during the propagation through 5 g/cm^2 of atmospheric depth 100
5.3 The flux of cosmic ray deuterons at the top of the instrument . . 101
5.4 The attenuation factors due to total inelastic interactions of deuterons with the atmospheric overburden 102
5.5 The flux of deuterons at the top of atmosphere 103
5.6 The deuteron-to-proton ratio at the top of atmosphere 103
5.7 The deuteron-to-helium ratio at the top of atmosphere 104
5.8 The flux of tritons at 5 $g \cdot cm^{-2}$ of atmospheric depth 105
5.9 The ratio of tritons at 5 $g \cdot cm^{-2}$ to ^4He at the top of the atmosphere 105

A.1 Partial derivatives for the elements of matrixes Z and V 114

C.1 IMAX Detector Grammages 122

D.1 Total reaction cross sections reference list for proton-proton collisions 124

D.2 Total reaction cross sections reference list for proton projectiles on carbon target 125
D.3 Total reaction cross sections reference list for proton projectiles on ^{14}N, ^{16}O and ^{19}F targets 126
D.4 Total reaction cross sections reference list for proton projectiles on ^{27}Al target 127
D.5 Total reaction cross sections reference list for proton projectiles on ^{28}Si and ^{56}Fe target 128
D.6 Total reaction cross sections reference list for proton projectiles on ^{40}Ar and ^{63}Cu target 129
D.7 Total reaction cross sections reference list for deuterium projectiles on proton and carbon targets 133
D.8 Total cross sections reference list for ^{3}H and ^{3}He projectiles on proton, carbon and aluminium targets 134

Chapter 1

Introduction

Energetic particles hitting the Earth's atmosphere were discovered nearly a hundred years ago. Since it was clear that their origin must be in the outer space their name was coined to *Cosmic Rays* (CR). Their main constituents are the ordinary nuclei of matter found in the solar system but with different abundances, especially for the light nuclei and sub-Iron elements.

If we are to understand the origin and composition of CR, it is necessary to relate the observed CR spectrum and composition near Earth to those at the sources. This is done by a physical model of CR propagation in the interstellar medium. The generally accepted picture has "primary" CR, produced in sources distributed throughout the galactic disk, which subsequently move in and out of the disk and the nearby more-rarefied galactic halo. Eventually the CR diffuse into distant regions of the halo and are lost from the galaxy.

Some of the nuclei in CR are produced in collisions of the primary CR with the ambient interstellar gas, and are termed "secondary" CR. By measuring the abundances of these secondaries relative to primary CR, which are synthesized abundantly in stars, it is possible to test the predictions of several competing propagation models. From such a kind of measurement, as for instance the B/C ratio, it has been inferred that cosmic-rays in the GeV/nuc energy range traverse $\sim 6\ g \cdot cm^{-2}$ of equivalent hydrogen between injection and observation [28].

Among other ratios suitable for such a measurement, as *sub-*Fe/Fe or $\bar{p}/p$, the light nuclei are another possibility to test the validity of the various propagation models. Protons (P) are by far the most abundant components among the primary CR, followed by the ^4He nuclei. Their isotopes, deuterium (D), tritium (T) and ^3He, are generally believed to be secondary particles and therefore the ratios $^3He/^4He$ and D/P are candidates for this type of measurement.

The present work concentrates on the D/P ratio, therefore the separation of deuterium from the other hydrogen isotopes will be thoroughly investigated. Also the $D/^4He$ ratio is of main interest here, since the spallation of ^4He plays the dominant role for the deuterium production above 1 GeV/nuc.

Beside deuterium, tritium can also provide useful information. Although a secondary component, tritium is an unstable isotope with a negligible mean lifetime if compared to the mean age of the CR ($12.3y \ll 10^7 y$) and therefore it is virtually absent in the CR. Therefore, the observed tritium is produced essentially in the interactions of CR with our atmosphere, from the spallation of helium and heavier nuclei. If the atmospheric depth for the production of tritons is known, the triton-to-helium ratio may provide a validity test for the production cross-sections used in propagation calculations through the atmosphere.

Numerous experiments have been performed in order to measure the CR composition. The IMAX balloon-borne experiment, whose data will be used in this work, was designed to measure the abundances and spectra of light isotopes and antiprotons in the cosmic radiation, over an energy range from about 200 MeV/nuc to 3 GeV/nuc. The instrument had a successful flight from Lynn Lake, Manitoba, Canada (56° latitude, geomagnetic cutoff 100 MV) on 16-17 July 1992, attaining a float altitude of about 36 km for a duration of about 16 hours. The analyzed data from this experiment have provided during the years important results already published: $\bar{p}/p$ ratio, $^3He/^4He$ ratio and the absolute fluxes of protons and helium at the top of the atmosphere [64, 74, 62]. However, the hydrogen isotopes were not completely analyzed [74, 68]. The goal of the present work is to perform an independent, more detailed and comprehensive analysis focused on these ratios, with a special care in minimizing any effects that might introduce a bias. As an additional result of this analysis, the triton-to-helium ratio will also be obtained.

The thesis is structured in six chapters. The first and current one, motivates the scientific goal of this work and offers a schematic view over the whole content. Chapter 2 contains a general presentation of the IMAX instrument.

Chapter 3 describes in more detail the methods of data analysis that leads to the determination of rigidity, velocity and charge. In this chapter, the following analyses related to the individual detectors are performed: maximum detectable rigidity, χ^2-distribution and especially the time-of-flight calibration and charge selection.

Chapter 4 is dedicated to the resolving of singly charged particles in the instrument by means of mass histograms simulation. Since multiple scattering influences the quality of mass histograms, a particular care has been payed to simulate this effect by two methods: one by using empirical deterioration factors and another by using empirical background shapes. This chapter provides the deuteron-to-proton and triton-to-proton isotopic ratios in the instrument.

Chapter 5 is dedicated to the instrumental and atmospheric corrections applied to the isotopic ratios in the instrument, in order to obtain the following quantities at the top of the atmosphere: deuteron-to-helium ratio, deuteron-to-proton ratio, differential deuterium flux and triton-to-helium ratio.

Chapter 6 provides a comparison of the results achieved by this work with

similar measurements and theoretical predictions from the literature together with the conclusions of this thesis.

Chapter 2

The Isotope Matter Antimatter Experiment (IMAX)

The Isotope Matter Antimatter Experiment (IMAX) was a balloon-borne superconductive magnet spectrometer designed to measure the galactic cosmic rays fluxes of antiprotons and light isotopes with a useful energy range for mass identification spanning from 0.2 *GeV/nuc to* 3.2 *GeV/nuc. This is accomplished by a simultaneous measurement of charge, velocity and rigidity of incoming particles. This chapter will cover descriptions of the IMAX payload and the individual detector systems while an emphasis is put on those components mainly responsible on the current analysis of deuterium.*

2.1 Introduction

The instruments attempting to study cosmic rays aim to identify the incoming particles and also to measure their energies. The technique used in IMAX for identifying particles relies on the fact that the curvature radius r of a charged particle in a uniform magnetic field is expressed by the relation:

$$r = \frac{{}^{A}_{Z}p}{Z \cdot e} \cdot \frac{sin\theta}{B}. \tag{2.1}$$

Here B is the magnetic field, θ the angle between the field and the initial velocity, $Z \cdot e$ the nucleus charge and ${}^{A}_{Z}p$ its momentum. The first term in the right hand side, proper to each type of particle, is commonly denoted as rigidity R since it is a measure of how much "rigid" will be the track in a given magnetic field:

$${}^{A}_{Z}R = \frac{{}^{A}_{Z}p}{Z \cdot e}. \tag{2.2}$$

If one replaces the momentum and present the result in terms of mass M we get:

$$M = \frac{R \cdot Z \cdot e}{\beta \cdot c}\sqrt{1 - \beta^2} \tag{2.3}$$

Therefore a simultaneous measurement of rigidity, charge and velocity assures the determination of mass. The energy of particles is thereafter easily inferred once that the mass and the velocity are known. In order to achieve this, a tracking system was used to provide rigidities, a set of two scintillator counters plus time-of-flight (TOF) paddles were responsible for the charge determination while for performing the velocity measurements, a combination of the TOF system and three Cherenkov counters was used. All the detectors are shown in figure 2.1 and they are described more in detail in the next subsection.

IMAX was built in a collaboration between New Mexico State University, NASA Goddard Space Flight Center (GSFC), California Institute of Technology (Caltech), the Danish Space Research Institute (DSRI) and the University of Siegen. The University of Siegen provided the drift chambers while NASA/GSFC was responsible for the TOF, S2 scintillator and the overall management. Caltech's added the aerogel Cherenkov counters (C2 and C3) and DSRI provided some aerogel development support. The IMAX payload framework, including the magnet, the MWPCs and S1 scintillator was provided by NMSU.

As can be noticed from figure 2.1, the central position of the instrument is occupied by the magnet and the tracking devices, consisting of drift chambers (DC) and multiwire proportional counters (MWPC). Above and below there are the Cherenkov counters and the scintillators: the time-of-flight system organized in two groups of scintillator paddles, top and bottom (top-TOF and bottom-TOF), the two aerogel Cherenkov counters, the teflon Cherenkov Counter (C1) and the two scintillator light integration boxes.

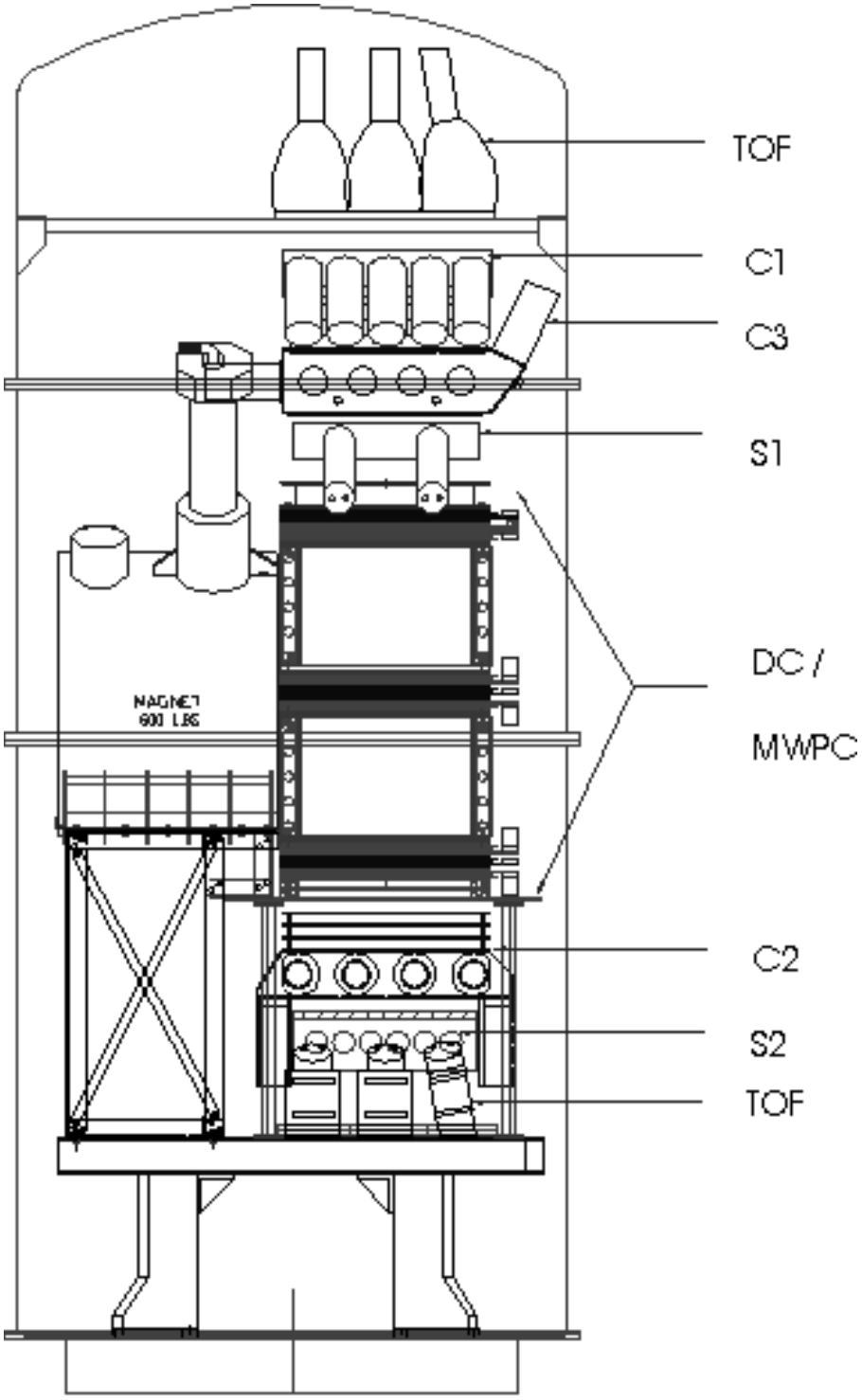

Figure 2.1: IMAX Payload schematics.

2.2 Spectrometer

2.2.1 Magnet

IMAX used the superconductive magnet from the NASA Balloon Borne Magnet Facility (BBMF) operated by the Particle Astrophysics Laboratory at New Mexico State University (PAL-NMSU) [30, 32]. The magnet operated at a normal flight current of 120 A, which resulted in an inhomogeneous magnetic field between 0.1 and 2.1 T in the drift chambers and up to 2.5 T in the region of the central multiwire proportional counters. The single coil, which consists of filamentary NbTi embedded in a Cu matrix, was placed in a liquid helium dewar and thus kept in a superconductive state. A second surrounding dewar filled with liquid nitrogen reduced the evaporation of liquid helium and permitted a life time of the superconductive state up to one hundred hours. The magnetic field lines inside the drift chambers are represented in figure 2.2.

2.2.2 Drift Chambers

For measuring particle tracks IMAX used a combination of drift chambers and multiwire proportional chambers. The drift chambers, whose model is shown in figure 2.3, were developed and constructed at the University of Siegen [43].

The passage of energetic charged particles, such as electrons, protons or nuclei, through a gas, which is electrically neutral, causes the ionization of the gas molecules. If the kinetic energy of the particles is larger than the ionization energy of the gas atoms, the electric fields of these charged particles pull electrons out from molecules near their path, producing what is called an ion pair. Along the ionizing particle track, a "mirror" track will be thus formed in a gas, consisting of ion pairs. The problem of a particle track detection is then equivalent to obtaining an "image" of such an electrically charged band in gas. After the gas was ionized the ion-electron pairs tend to recombine, returning to the neutral state, and consequently after a short time these types of tracks will vanish. To prevent this, the gas could be placed between an anode and a cathode, which can collect the charges before they will recombine. If the drift time of the electrons from the place of their creation until the arrival at the anode is known then one can draw conclusions about the distance they have travelled in the gas and points from the track can be calculated (see section 3.1.1).

IMAX contained two drift chambers placed above and below the central axis of the IMAX magnet coil. Combining both chambers, a total of 20 positions along a particle track can be measured. Twelve X-coordinates account for the bending direction and eight Y-coordinates for the non-bending one (see figure 2.3). The lateral walls of the chambers were made of 1 cm thick epoxy-composite

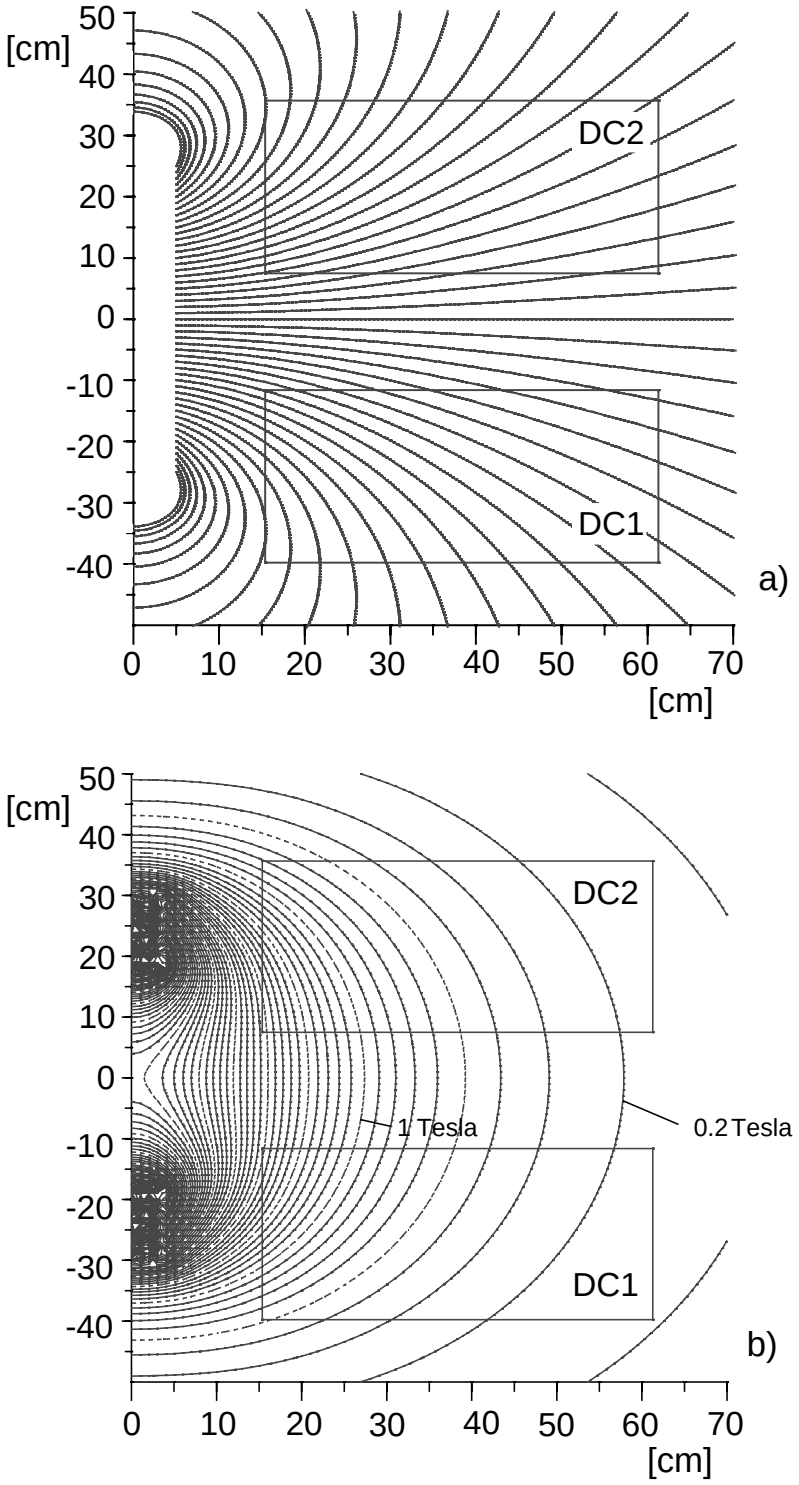

Figure 2.2: IMAX magnetic field lines a) and isomagnetic lines b).

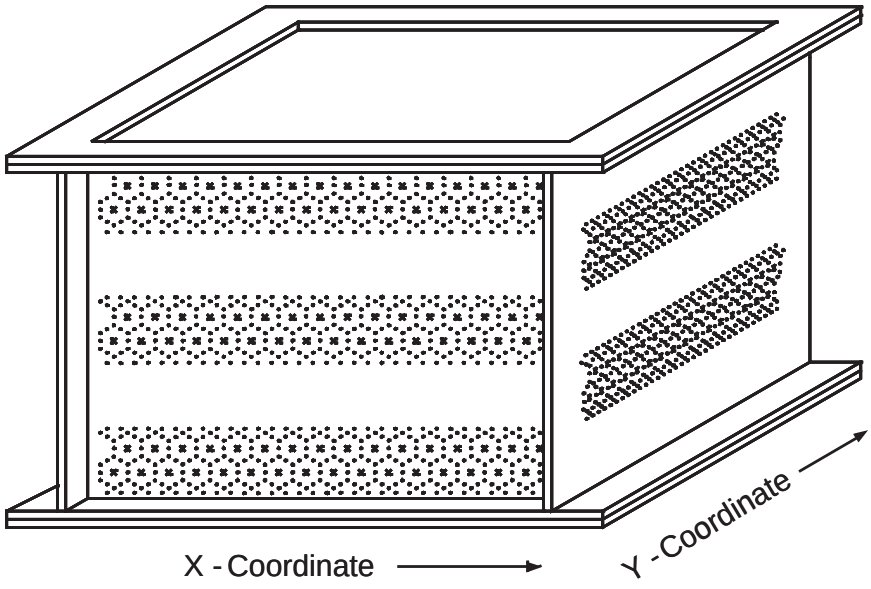

Figure 2.3: IMAX Drift Chamber.

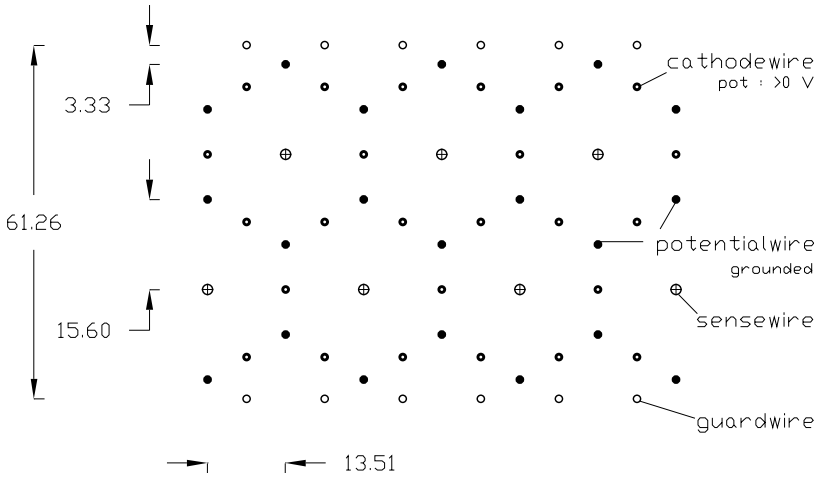

Figure 2.4: Drift chamber cell structure.

plates with the interior dimensions of 47 x 47 x 33.3 cm^3 while their upper and lower parts were covered with 125 μm mylar foils laminated on 35 μm copper foils. As gas, CO_2 of 99.995% purity was used. This particular gas was chosen because liberated electrons drift slowly compared to common drift chamber gases and thus their drift paths are less affected by the Lorentz force [77]. During the balloon flight, a constant gas flow of 3 to 4 l/h was maintained through the chambers with the goal of compensating the pressure changes due to temperature gradients within the gondola.

The inner space of the chambers is divided in small hexagonal drift cells, made up from an anode wire in the center and cathode wires in each corner of a hexagon. Such a drift cell structure is illustrated in figure 2.4. The wires consist of gold-plated tungsten of 30 μm diameter for the anodes and 100 μm for the cathodes. The reason for the choice of a hexagonal drift cell is the fact that one needs to obtain an electric field as symmetric as possible in order to have the curves of equal drift times as close as possible to circles. The introduction of additional potential wires has the role of increasing the symmetry of the field, as shown in figure 2.5 [17]. The guard wires are added between the adjacent X and Y layers and between the outer layers to prevent distortions of the electric field in the cells. The anodes operated at 4600 V, the cathodes at 500 V while the potential wires were grounded.

Signals from anodes were read by a system of LeCroy 4290 TDCs via LeCroy 2735 amplifiers and discriminators [61]. A time measurement in the TDCs was started as soon as the signal generated by the drifted electrons at the anode was significant enough to pass the discriminators. The stop signal, common for all 320 TDC channels was the system trigger delayed with 3.5 μs. The drift times, with a maximum value of about 2.2 μs, were able to be measured with a resolution of 3 ns. The drift chambers system achieved position resolutions up to 50 μm for Z=2 and about 70 μm for Z=1 particles.

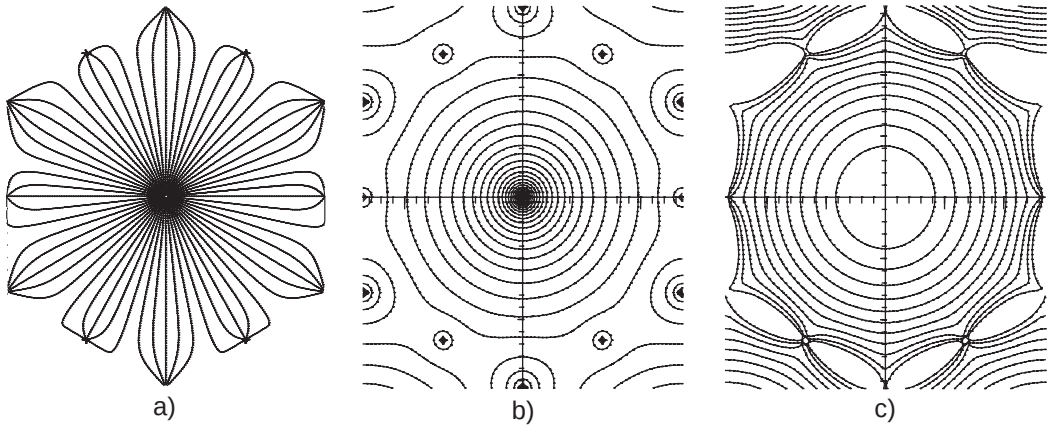

Figure 2.5: Drift cell electric field : a) electric field lines, b) equipotential lines and c) lines of equal drift time.

2.2.3 Multiwire Proportional Counters

The multiwire proportional counters (MWPC) were designed in the beginning of the 70's and were provided by the Particle Astrophysics Laboratory at New Mexico State University [52]. The functioning principle is similar to the one of DCs, based on the ionization of a gas traversed by charged particles. However, in this case, points along the incoming particles tracks are not inferred from measuring electron drift times. The charged particle passing through the MWPC's gas liberates electrons which travel towards the anodes. Due to the increasing electric field near the anodes they are accelerated and thus a cascade of ionization begins to form. The charges reaching the anodes are drawn off by a capacitor and the remaining distribution of positive ions induces a negative image charge on the cathodes (see figure 2.6).

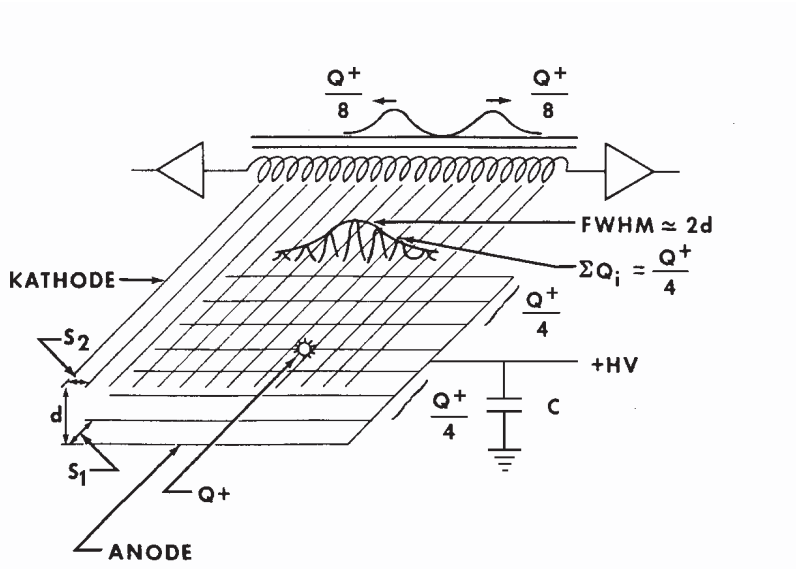

Figure 2.6: Functioning principle of MWPCs.

The 8 MWPCs used in IMAX consisted of parallel arrays of anode and cathode wires. One layer of anodes, each 2 mm thick, is positioned between two cathode layers at a spacing of 6 mm. The orientation of the cathode wires from the bending direction layer is perpendicular to the anodes whereas the non-bending layers are parallel to them. The anode plane was typically run at 4.7 kV with the respect to the grounded cathode plane. The MWPCs were filled with the so-called "Magic Gas", which is a mixture of 70% Ar, 29.5% C_4H_{10} (isobutane) and 0.5% CCl_3F (Freon). Its properties cause that the electrons which have to drift longer paths until anodes will recombine and therefore the magnetic field influence on the position information is diminished.

The signals on cathodes were transferred inductively to a delay line, discriminated and thereafter being read at each end by a TDC 4208. Those 24-bit-TDC have a time resolution of 1 ns and therefore can measure times up to 8.4 ms. The sum of the two propagation time signals is always constant at the value of about 7μs but the difference is position dependent. With this detector a position resolution from 330 μm up to 1500 μm was reached, with the better values for the bending direction because the cathode wires of the Y-view are parallel with the anodes.

2.3 Time-of-Flight System

The detector responsible both for velocity measurement and the instrument trigger signal was the Time-of-Flight system (TOF) and it was developed at NASA's Goddard Space Flight Center in Washington D.C. [63]. It consisted of two arrays of 3 scintillator paddles each, one at the top and the other at the bottom of the payload (see figure 2.1).

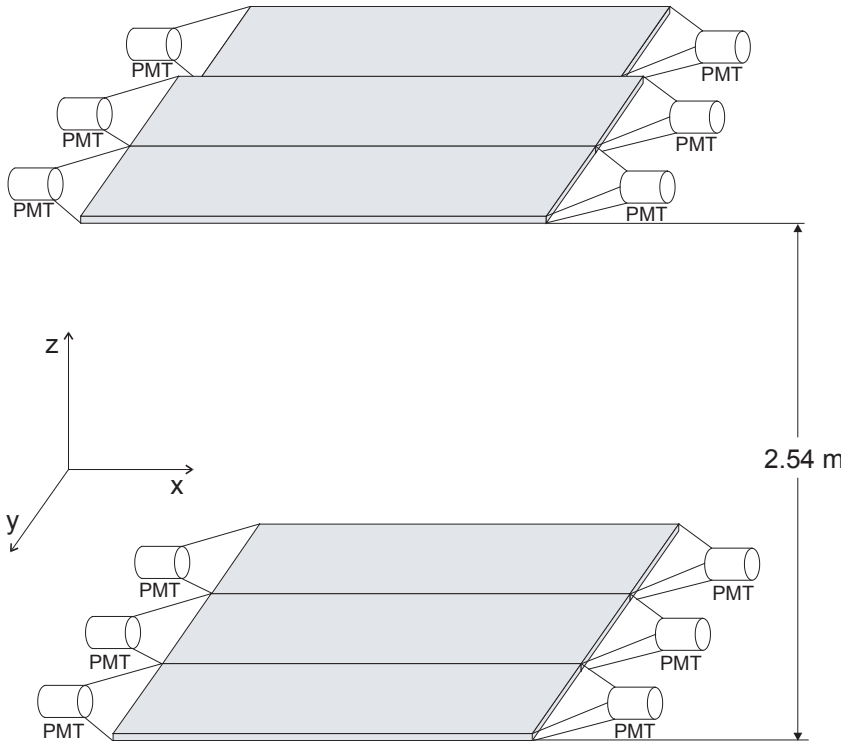

Figure 2.7: IMAX Time-of-Flight System (TOF)

Three paddles from the bottom array and one from the top were 60 cm x

20 cm x 1 cm Bicron BC-420 plastic while the remaining two were longer : 66 cm x 20 cm x 1 cm (see figure 2.7). At the end of each paddle a Hamamatsu R2083 photomultiplier, mounted within steel magnetic shielding tubes, collected the scintillation signal through light pipes (25 cm x 5 cm x 1 cm) made of acrylic plastic capable of transmitting ultraviolet light.

The high voltages applied to the tubes during the flight were between -2.7 kV to -3 kV. Further, every photomultiplier signal was split in two, a smaller part being used for time measurement and the other for the energy loss. Timing signals were sent firstly to LeCroy 4413 discriminators, then further to LeCroy 2290 TDCs (30 $ps/channel$) with the thresholds set at 15 mV (pulses induced by a minimum ionizing particle were generally above 100 mV) and finally to OR-Logic LeCroy 4564. For the dE/dX measurement LeCroy 2249A ADCs were used.

2.4 Scintillator Counters

In a scintillator the passage of a charged particle transfers some of its energy to electrons by exciting them to higher energetic states. The energy released after the de-excitation to the initial states is released via fluorescence light. Thus, the measured light yield will be proportional to the energy deposited in the scintillator and consequently to the square of the incident particle charge [40]. IMAX contained two such scintillator counters for the charge measurement.

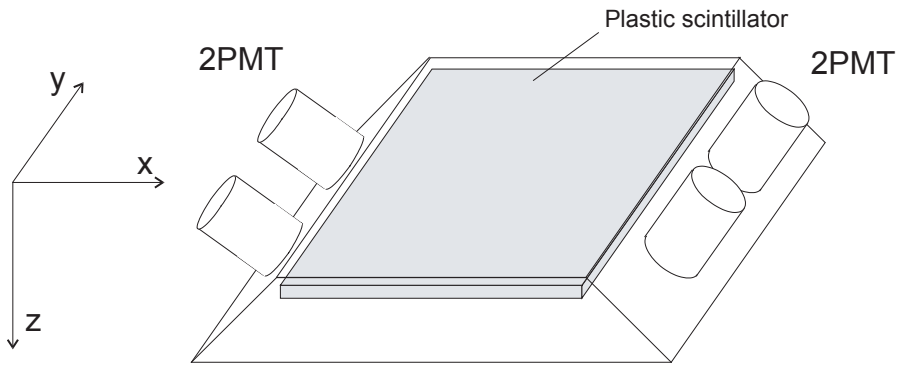

Figure 2.8: IMAX Scintillator Counter S1

The scintillator S1 was built and developed in New Mexico State University and contained a 51 cm x 51 cm x 1 cm Micron BC-400 plastic scintillator in a $BaSO_4$ coated aluminium box (see figure 2.8). The box is viewed by four magnetic shielded Hamamatsu photomultipliers R1307, gathered into two pairs which are

separately analyzed with LeCroy 2249A ADCs gated at 200 ns. The scintillator S2 was provided by NASA's Goddard Space Fligth Center. It contained a 55 cm x 49 cm x 1.8 cm Bicron BC-408 plastic scintillator. For the read out, twelve Hamamatsu R 2490-01 phototubes were used, all separately pulse-height analyzed with the LeCroy 2249A ADCs gated at 125 ns.

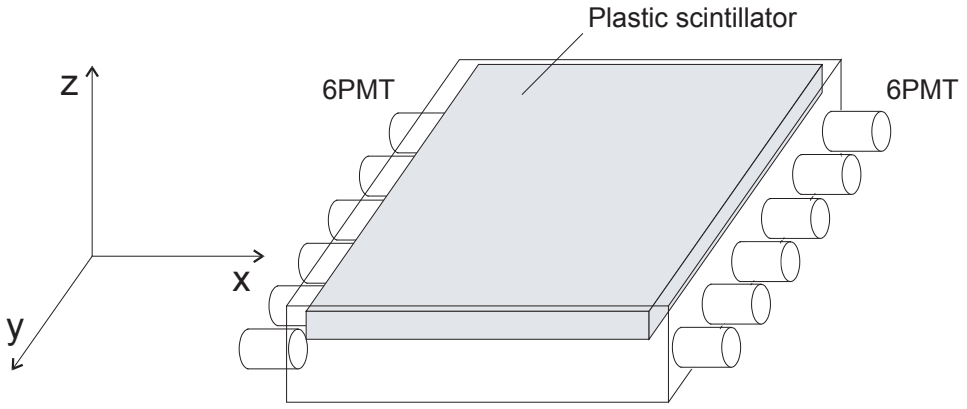

Figure 2.9: IMAX Scintillator Counter S2

Although the plastic scintillator efficiency (fraction of deposited energy which is converted into light) have not the highest efficiency among organic scintillators, they have the advantage of being inexpensive and easy to be manufactured and handled. With the rule of thumb that one photon is yielded per 100 eV of energy loss in the plastic scintillators and with 1-10 MeV energy loss per IMAX scintillator the detection efficiency approach 100%.

2.5 Cherenkov Counters

If a charged particle passes through a material with the refractive index n and a velocity v greater than the velocity of light in that material c/n then a specific electromagnetic radiation is emitted, shortly called Cherenkov radiation. The explanation for this phenomenon is that the atoms along the track are polarized and the dipole fields formed this way emit photons once they vary in time. From the above condition it is easy to infer that a particle will emit Cherenkov light as long as it moves at a speed β bigger than $1/n$.

There were in total three Cherenkov detectors which aimed to measure velocities in the IMAX experiment (see figure 2.1): the detector C1, developed by New Mexico State University and which used Teflon radiators with a refractive index $n = 1.33$ and the detectors C2 and C3 developed by California Institute of Technology to measure energies from 2 GeV/nuc up to 3.5 GeV/nuc. For this

goal, aerogel with a refractive index $n = 1.043$ was chosen. These detectors are described in full detail in [53] and they are not used in the present analysis.

Chapter 3

Mass Separation

This chapter presents in detail how the separation of mass is achieved with the IMAX spectrometer. The first section presents how the rigidity can be inferred by using the measurement of track points. The second section will explain how the velocity measurement is achieved by analyzing the data of the time-of-flight (TOF) system. The main task in this section is to perform the TOF calibration. The last section describes how the charge can be determined by measuring the energy deposited in scintillators. The charge separation of the hydrogen isotopes from the helium nuclei will be performed by choosing an appropriate selection ctriterium and the efficiency of this selection will be determined.

3.1 Rigidity Determination

In this section it is first presented how the position measurement is performed both with drift chambers and with MWPC in IMAX tracking systems. Next step shows how from the track points obtained in this way the rigidity can be determined by using an iterative fitting procedure. The relevant characteristics of the detector for this work are analyzed and presented in the final part: the maximum detectable rigidity (MDR) and the χ^2-distribution of tracks.

3.1.1 Position Measurement

In the IMAX instrument there were two different tracking systems grouped in a hybrid system. A very detailed description of both analysis from drift chambers and multiwire proportional chambers are given in [61] here being depicted only the principle of functioning.

Multiwire proportional chambers and drift chambers are quite different from each other in the way of determining the position of a particle's passage in the

detector. In the case of MWPC the measurement is based on calculating the difference of propagation times at both ends of a delay line, in this way the coordinates being already roughly measured. After corrections for the variation with the distance of the signal propagation velocity and for the length dependency of the delay wire with temperature, the MWPC provided points with position resolutions varying from 330 to 1500 μm.

For performing the data analysis of IMAX drift chambers one had to overcome more complicated problems. As described in the second chapter, the drift chambers measured propagation times of electric signals formed inside a drift cell, from track points until the anode wires. The first major task is to allocate to every measured drift time a drift path and this can be achieved by calculating the so-called "Drift-time to Path Relation" (DPR).

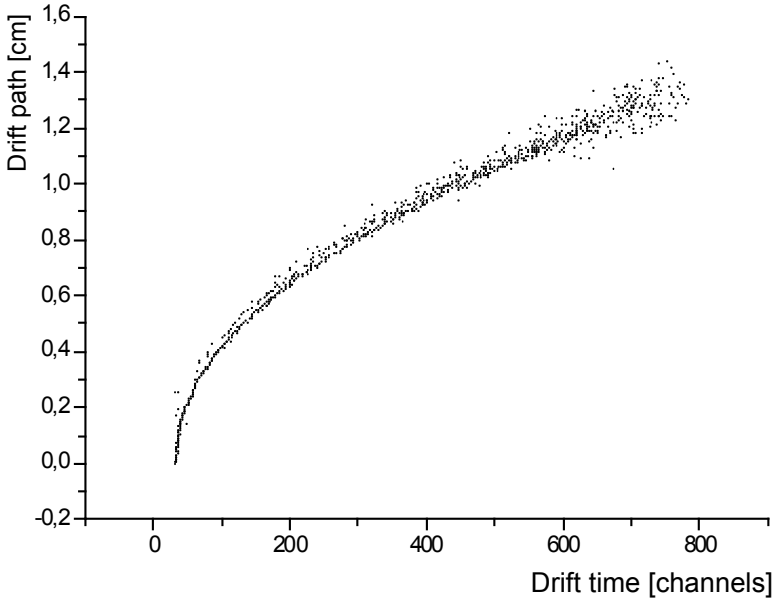

Figure 3.1: Drift-time to Path scatter plot.

The drift times are obtained from the measured TDC times after an offset is subtracted. The offset times are proper to each drift cell. They are slightly different from each other due to different length of signal paths and can be inferred from the distribution of the measured times for every cell [61]. The DPR is then obtained by means of an iterative procedure. In order to be able to fit a track, a square-root DPR relation is assumed in the first iteration. This assumption is based on the cylindrical symmetry of the electric field inside a cell and the fact that the drift velocity is almost linear in the case of a CO_2 drift gas [77].

By fitting a track to the drift circles obtained with the approximate DPR a new estimate of the drift paths is obtained from the distance between the estimated track and the anode wire. A cubic spline fit performed through all the new estimated drift paths as a function of the drift times, presented in figure

3.1, provides a new improved DPR. The iterative procedure continues until the differences between two consecutive DPRs become few micrometers.

Due to asymmetries in the electric field of a cell there is a small dependence of the DPR on the angle of incidence, therefore only tracks penetrating the instrument at angles lower than 2.5° are firstly analyzed. In the case of tracks with larger angles, an angle correction was additionally performed. Moreover, the temperature variations inside the instrument cause variations of the drift gas CO_2 density and thus, DPR being modified, a calculation of DPR every thirty minutes was necessary.

Besides the position measurement, the other important quantity in the rigidity determination is the drift chamber position resolution, which can be calculated on the basis of a residual scatter plot [22, 60]. The residuals are defined as the difference between the fitted track and the measured track point as given by the DPR: $x_{res} = x_{fit} - x_{meas}$ as illustrated in figure 3.2. Figure 3.3 shows the distribution of residuals as a function of the drift path for a sample of measured particle tracks.

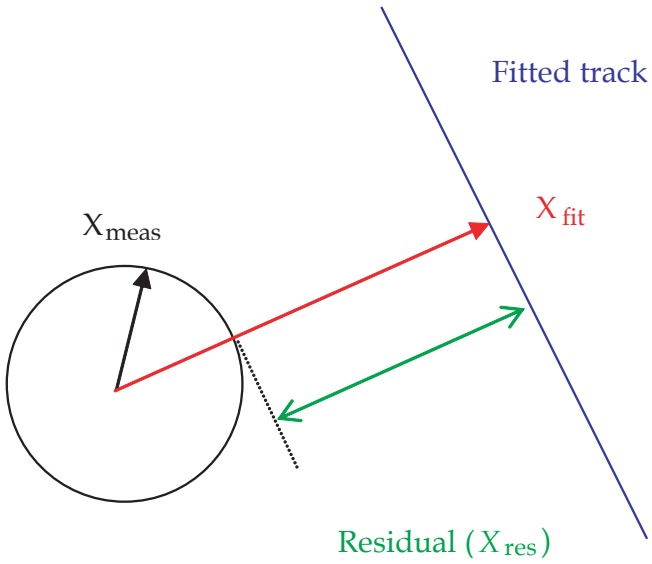

Figure 3.2: Definition of the residual

This kind of representation shows easily if a certain DPR describes correctly the data by looking if the points are centered around the X axis and one can already guess how good is the resolution by observing the width of the distribution around the same axis. The position resolution is the standard deviation of the gaussian that fits the residual histogram built for each specific drift interval. It is clear from the plot that the position resolution is drift-path dependent, the best values being obtained for medium drift paths. Thus, the position resolution was derived from the residual histograms built for each specific drift interval. In previous works it has been noticed that the calculated residuals depend on the

number of points used for the fitting procedure [67, 51, 44]. According to that, the adopted method was to correct each residual with an approximated multiplying factor:

$$x_{reskor} = x_{res} \cdot \sqrt{N/(N-f)} \tag{3.1}$$

In relation 3.1, N is the number of measurement layers and f is the number of fit parameters. In case of straight tracks and X and Y projections fitted independently, we have $f = 2$ and therefore there are $N - 2$ two degrees of freedom, whereas for the magnet on, all the points are fitted simultaneously and $f = 5$.

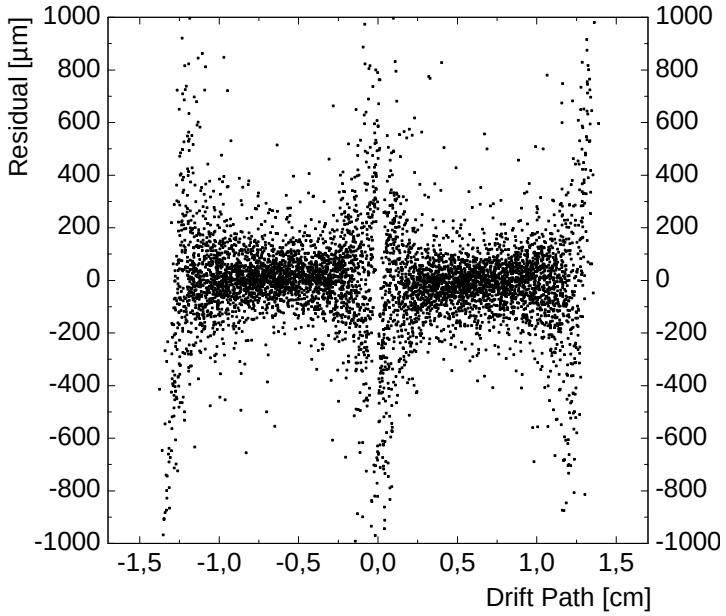

Figure 3.3: Residual Distribution as a function of the drift path.

An important difference between the DPRs in the case of magnet on and off is the effect on the drift path due to the magnetic field. For cells situated in stronger magnetic regions, the drift path is extended by curving because of the Lorentz force and therefore measured drift times are systematically larger than in the case with magnet off. The adopted procedure is similar to the angle correction, in the sense that one does not compute different DPRs for zones with stronger magnetic field, but rather a correction matrix, built from the residuals itself. The space resolution obtained in this way is essentially magnetic-field independent and reaches minimum values at about 50 μm for $Z = 2$ and about 70 μm for $Z = 1$, both for medium drift distances as it is shown in figure 3.4.

The poorer resolution at long drift paths can be explained due to both a reduced symmetry of the electric field and electron diffusion. In the case of shorter

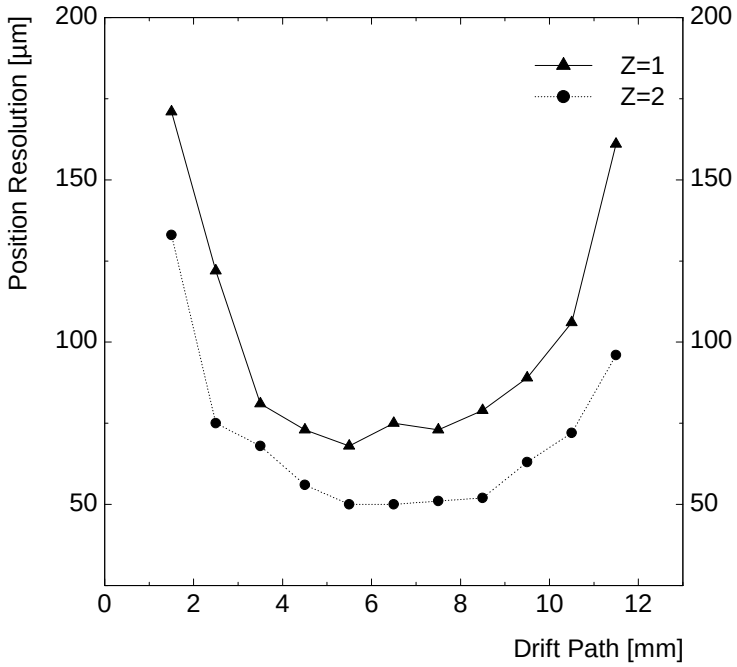

Figure 3.4: Position resolution of IMAX drift chambers

distances the drift velocity increases sharply in the proximity of the anode wires and an error in timing translates into a larger position error. In addition, when a particle passes closer to the sense wire, the clustering of ionization along the path translates into an error in position since electrons may not be liberated at the point of closest approach.

3.1.2 Rigidity Determination using an Iterative Fitting Procedure

The rigidity determination based on position measurements of track points, relies on the integration of the equation of motion for a charged particle in a magnetic field, motion which is described by the Lorentz force:

$$m\gamma\frac{d^2\vec{r}}{dt^2} = \frac{q}{c}\left(\frac{d\vec{r}}{dt}\times\vec{B}\left(\vec{r}\right)\right) . \tag{3.2}$$

Due to the fact that the detectors provide track points at fixed positions in space, it turns out to be more appropriate to express the equation as a function of position rather than of time. By introducing the parametrization $dl = \beta c dt$, the acceleration of the particle can be expressed as:

$$\frac{d^2\vec{r}}{dt^2}\left(t\right) = \beta^2 c^2 \frac{d^2\vec{r}}{dl^2}\left(l\right) . \tag{3.3}$$

By substituting the expression 3.3 in 3.2 one gets for the motion law :

$$\frac{d^2\vec{r}}{dl^2} = \frac{\eta}{c}\left(\frac{d\vec{r}}{dl}\times\vec{B}\left(\vec{r}\right)\right) \tag{3.4}$$

where the quantity η is called deflection and it is equal to:

$$\eta = \frac{q}{m\gamma\beta c} . \tag{3.5}$$

As one can easily notice, the deflection is the inverse of the rigidity defined in Chapter 2 (relation 2.2). Given the magnetic field $\vec{B}$, known at every point inside the tracker, the rest of the quantities needed to reconstruct the trajectory is contained in the so-called *status vector* : $\vec{\alpha} = (\vec{r}_0, d\vec{r}/dl|_{\vec{r}_0}, \eta)$ where $\vec{r}_0$ is the space vector of the particle in the initial point and $d\vec{r}/dl|_{\vec{r}_0}$ indicate the direction of the velocity in $\vec{r}_0$. One should note that because of the chosen parametrization, $d\vec{r}/dl$ is a unit vector with the information about velocity being transferred to the deflection, which makes the components of this vector to be its direction cosines.

The equation of motion 3.4 can be numerically integrated and the details are presented in appendix A. The particle track reconstructed this way, being nothing else than the theoretical path through the detector, provides actually a fit to the measured points. The agreement between this fit and the measured points of the track depends on the correctness of the choice of status vector. Therefore, the correct status vector and implicitly the correct rigidity, is given by the status vector that minimizes the χ^2 of the fit:

$$\chi^2\left(\vec{\alpha}\right) = \sum_{i=1}^{N_x}\left(\frac{x_i\left(\vec{\alpha}\right) - x_{mi}}{\sigma(x_{mi})}\right)^2 + \sum_{i=1}^{N_y}\left(\frac{y_i\left(\vec{\alpha}\right) - y_{mi}}{\sigma(y_{mi})}\right)^2 \tag{3.6}$$

where x_{mi} and y_{mi} represent the measured points in the i-th layer and $N_{x,y}$ the number of hits in the X and Y view, respectively. It is important also to notice that the position resolution σ varies with respect to the measured points since it varies with the drift path according to figure 3.4. The iterative minimizing procedure which leads to the rigidity is also described in the appendix A.

3.1.3 χ^2-Distribution

An important quantity for the goodness of the position measurements and therefore of the measured tracks quality, often mentioned throughout the thesis, is given by the value of the χ^2 obtained at the end of the minimization procedure mentioned above.

If one considers n random variables $u_1, u_2..., u_n$, normal distributed with $N(\mu_i, \sigma_i)$, then the new variable

$$\chi^2 = \sum_{i=1}^{n} \left(\frac{u_i - \mu_i}{\sigma_i} \right)^2 \tag{3.7}$$

will be distributed as following [16]:

$$f_n(\chi^2) = \frac{(\chi^2)^{\frac{n}{2}-1} \cdot e^{\frac{-\chi^2}{2}}}{2^{\frac{n}{2}} \cdot \Gamma\left(\frac{n}{2}\right)} \tag{3.8}$$

also called the χ^2-distribution with n degrees of freedom. In figure 3.5 $f_n(\chi^2)$ is plotted for n varying from 1 to 16.

Such a computation of chi-square has the disadvantage that it depends on the degrees of freedom, namely in the case of track measurements on the number of hit layers, making the analysis more cumbersome. In order to simplify it when cuts on χ^2 are to be performed, it is useful to introduce the normalized χ^2, $\chi^2_n = \chi^2/n$, which is distributed as:

$$\tilde{f}_n(\chi^2_n) = n \cdot \frac{(n \cdot \chi^2_n)^{\frac{n}{2}-1} \cdot e^{\frac{-n \cdot \chi^2_n}{2}}}{2^{\frac{n}{2}} \cdot \Gamma\left(\frac{n}{2}\right)} \quad . \tag{3.9}$$

As one can notice in figure 3.6, in comparison with the un-normalized case, for n large enough all distributions reach a maximum at $\chi^2_n \cong 1$ and are approximately the same at higher values of χ^2_n, making possible to use unique cuts even if the number of hit layers is variable.

In the case of a tracking system, the χ^2 variable has the expression:

$$\chi^2 = \sum_{i=1}^{N_x} \left(\frac{x_{mi} - x_i}{\sigma(x_{mi})} \right)^2 + \sum_{i=1}^{N_y} \left(\frac{y_{mi} - y_i}{\sigma(y_{mi})} \right)^2 \tag{3.10}$$

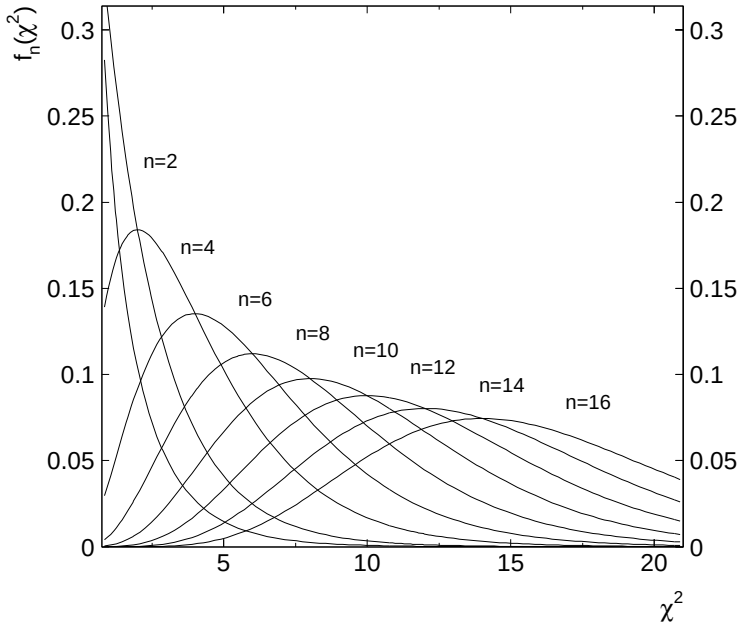

Figure 3.5: The χ^2-distribution with degrees of freedom varying up to 16.

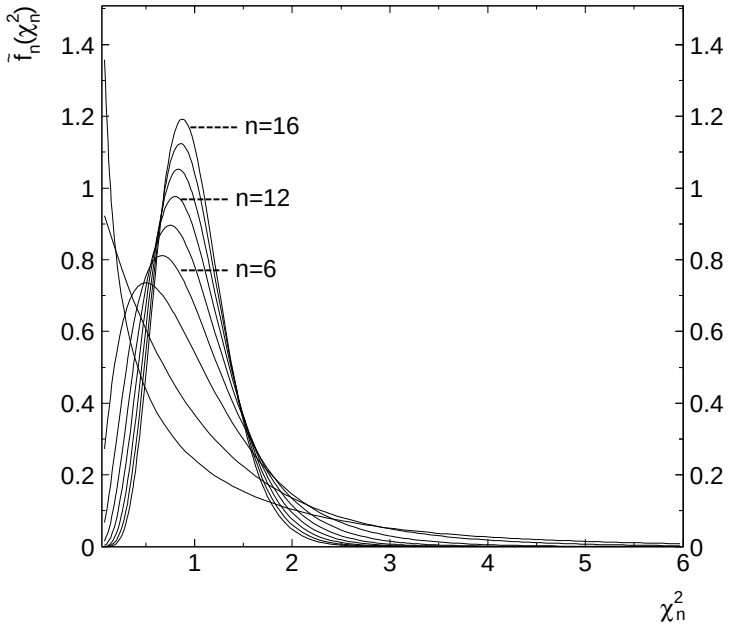

Figure 3.6: The normalized χ^2-distribution with degrees of freedom varying up to 16.

where x_i and y_i are the fitted points, x_{mi} and y_{mi} are the measured points and σ_i is the position resolution. In equation 3.10 N_x and N_y are the numbers of measurement layers which participate at the fit and which can vary up to 20 for the X-view and up to 12 for the Y-view. It can be demonstrated [7] that the values of χ^2 in this case are distributed according to a χ^2-distribution with $N_x + N_y - N$ degrees of freedom, where N is the number of fit parameters.

In order to select events of a good tracking quality, cuts in the χ^2 can be performed. Since the meaning of the collocation "good tracking quality" is that of a precisely measured deflection and the position measurements in the bending X-view are essential for it, two different χ^2 derived from the total one are commonly used, χ^2_x and χ^2_y as in the following:

$$\chi^2_x = \sum_{i=1}^{N_x} \left(\frac{x_{mi} - x_i}{\sigma(x_{mi})} \right)^2 \text{ and } \chi^2_y = \sum_{i=1}^{N_y} \left(\frac{y_{mi} - y_i}{\sigma(y_{mi})} \right)^2 . \tag{3.11}$$

The number of the hit layers N_x and N_y which are used in the fit vary on an event-by-event basis and consequently it is appropriate here to use the normalized χ^2. As it was previously presented, the five parameters that form the status vector are responsible for determination of the fitted points of a track. Because of the magnetic field configuration (figure 2.2), the bending in the Y-view could be considered negligible and the track is essentially a straight line. Therefore for the χ^2_y there are only two parameters left, the initial y position and the angle between the velocity vector and the YOZ plane. Since for the determination of the track the status vector has 5 parameters, for the X-view there are only three left. A better picture to understand why only three parameters are enough to determine the track is to consider the magnetic field largely homogenous, which makes the trajectories becoming closer to circles and thus determined by three parameters. The number of degrees of freedom becomes for the two views:

$$n_x = N_x - 3 \text{ and } n_y = N_y - 2 . \tag{3.12}$$

Figure 3.7 presents how two different χ^2-distributions, namely for $N_x = 16$ and $N_y = 8$, are brought to a similar shape by normalizing them. Thus, common cuts in χ^2 can be used, without the inconvenience of rejecting preferentially events with a higher number of measurement layers. The functions in the bottom figures represent the theoretical normalized χ^2-distribution calculated from the relation 3.9.

The discrepancy between the theoretical χ^2-distributions and the measurements is basically due to the fact that the position measurements as performed by IMAX are not exactly normally distributed, one of the reasons being the δ-ray emission. Moreover, apart from the interaction of incident particles with the magnetic field, which can be traced with the fitting algorithm, there are other

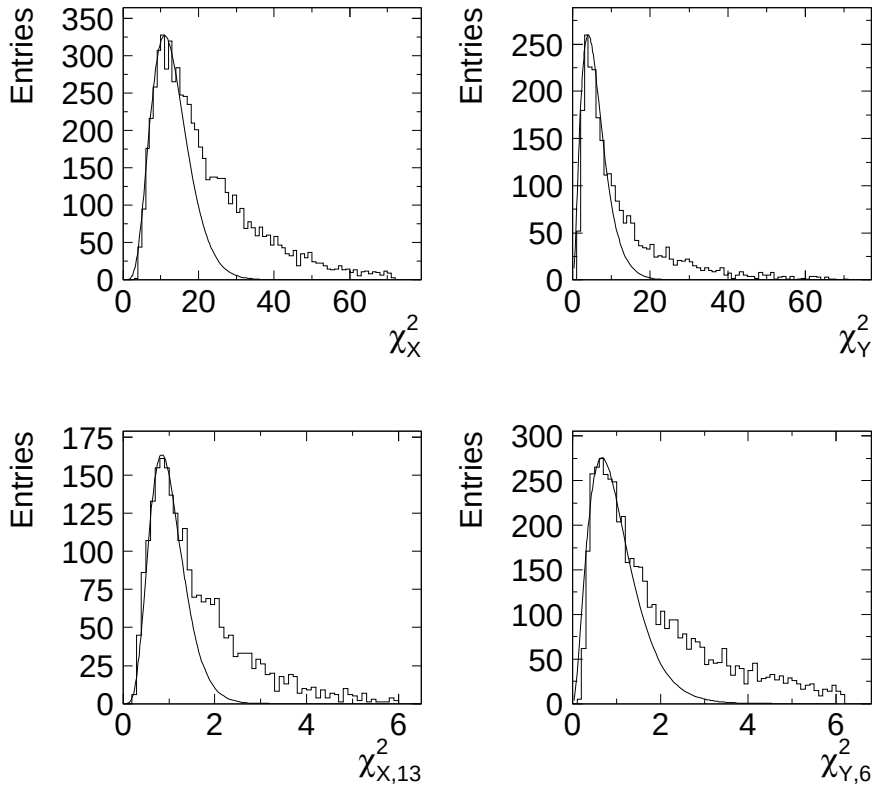

Figure 3.7: The usual and normalized χ^2 histograms for a) $N_x = 16$ and b) $N_y = 8$. The curves show the theoretical normalized χ^2-distributions.

kind of processes which are to be taken in consideration: Coulomb and inelastic (nuclear) scattering. An improvement of the fitting procedure against δ-electrons and multiple scattering was made by applying the so called " 5σ - method" [61]. This method is based on the fact that in case of gaussian variables there is a 99,999% probability for a measurement to lie inside the $\pm 5\sigma$ interval around the mean value and therefore points which do not fulfill this condition are put aside for the final fit, up to a maximum of two points.

3.1.4 The Maximum Detectable Rigidity (MDR)

The most important characteristic of a spectrometer is the so-called "Maximum Detectable Rigidity" (MDR). As the name already mentions, MDR is a quantity which characterizes the quality of the spectrometer and indicates up to which value the rigidity of an incident particle can be reliable measured.

By definition, the MDR corresponds to the rigidity value for which the measurement error is equal to the rigidity itself. In order to obtain a quantitative relation one has to take into account that the relative error on the momentum, introduced by to the spatial resolution alone has the following expression [37]:

$$\left.\frac{\sigma(p)}{p}\right|^{track\,resolution} = \frac{\sigma(x)}{0.3BL^2}\sqrt{720/(N+4)}\cdot p/Z\bar{e} \tag{3.13}$$

where $\sigma(x)$ is the spatial resolution, N is the number of position measurements and Z is the charge.

Equation 3.13 is written in the case of an uniform magnetic field and measurement layers equally spaced. This relation obviously represents only an approximation for IMAX case, where the magnetic field is not homogenous and the position resolution and the number of measurement layers are not constant. Taking in consideration the relations 3.5 and 2.2, one can also express the deflection error (also called $sigma - deflection$):

$$\sigma(\eta)|^{track\,resolution} = \frac{\sigma(x)}{0.3BL^2}\sqrt{720/(N+4)}\,. \tag{3.14}$$

As one can notice from the relation 3.14, the outstanding feature of the sigma-deflection is that it does not depend on the deflection itself, and therefore it could be used as a performance factor for a given spectrometer.

Sigma-deflection and MDR can be now easily related to each other. Considering the relation between rigidity and deflection error,

$$\sigma(R) = R^2\cdot\sigma(\eta) \tag{3.15}$$

it is easy to notice that if one measures the rigidity R equal to the quantity $1/\sigma(\eta)$ the relative error in rigidity becomes equal to the unit and therefore the sigma-deflection is related to the MDR as:

$$MDR = \frac{1}{\sigma(\eta)}\,. \tag{3.16}$$

This feature of the sigma-deflection also implies a linear relation between the relative error in rigidity and the rigidity itself:

$$\frac{\sigma(R)}{R} = \frac{R}{MDR}\,. \tag{3.17}$$

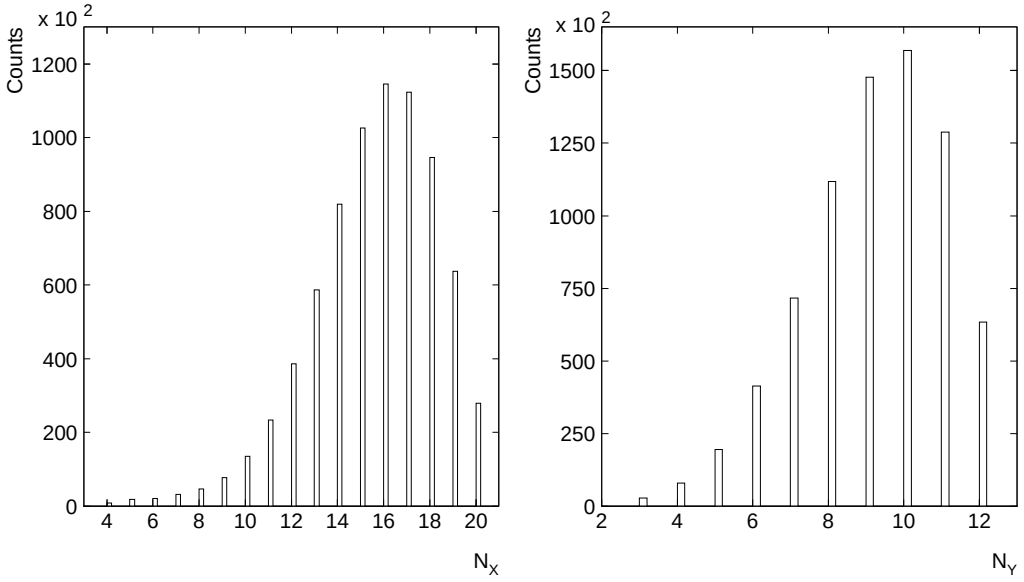

Figure 3.8: Distribution of the hit measurement layers for the X-view (left) and Y-view (right).

In the case of a spectrometer like the one of the IMAX instrument, I have mentioned before that the applicability of this formula is difficult. The sigma-deflection will vary on an event-by-event basis because the quantities on which it depends are not constant anymore.

Figure 3.4 already illustrates how the position resolution can vary in the measurement of a track. The number of measurement layers that participate at a fit is also variable, as presented in figure 3.8. The other dependency is related to the magnetic field and in IMAX case, where the magnetic field is not homogeneous, the term BL transforms to the field integral $\int |\vec{B} \times \vec{l}|_y dl$. This field integral, which is a measure for the transversal momentum gain during the propagation in the magnetic field, is presented in figure 3.9, as calculated from the fitted track lengths and the known magnetic field configuration.

Given the variation in the magnetic field integral, in the number of measurement layers and in the space resolution, the sigma-deflection is expected to be rather a distribution. In fact, it can be calculated as an outcome of the fitting process, as in the following:

$$\sigma(\eta) = \frac{1}{Z(5,5)} = \left(\frac{\partial^2 \chi^2}{\partial \eta^2} \right)^{-1} \tag{3.18}$$

where $Z(5,5)$ is an element of the matrix Z defined in appendix A.

In figure 3.10 it is presented the sigma-deflection distribution provided by the fitting algorithm, for events with rigidities greater than 20 GV. In order to

refer again to an MDR for this instrument, it has been accustomed to define the MDR_{track} as the reciprocal value of the sigma-deflection distribution maximum, obtaining a value of 185 GV.

The multiple scattering process contributes also to a further increasing of the deflection error. This process is important at low energies and as the energy increases the sigma-deflection remains only influenced by the tracking. Therefore, in order to show the performance in rigidity measurement only due to tracking, events at high energies ($R > 20\ GV$) were selected. Also, the notation MDR_{track} indicates that this value is connected with the relation 3.14, so it depends on the track resolution. The multiple scattering effect on the spectrometer will be discussed in detail in chapter 4.1.

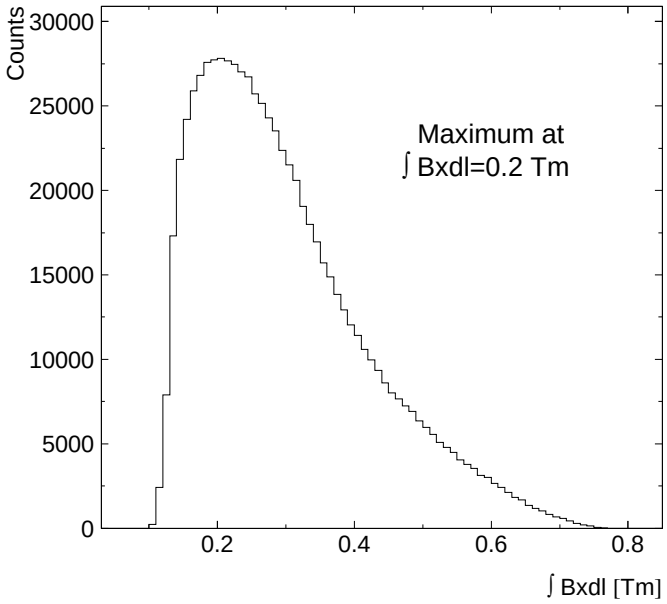

Figure 3.9: IMAX magnetic field integral.

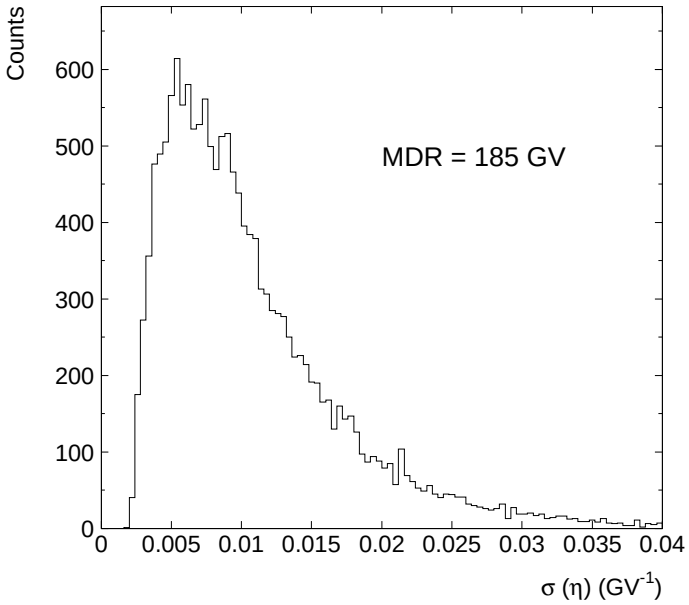

Figure 3.10: The sigma-deflection distribution for a sample of events with $R > 20\ GV$. The value of MDR indicated in the figure has been obtained from the maximum of the distribution.

3.2 Velocity Measurement

The velocity measurement with the TOF system is achieved by measuring the flight time between two scintillator paddles and the length of the particle track. In principle, a start signal for the time-to-digital converter (TDC) is generated when one of the top-TOF paddles is hit. When the particle passes through a bottom TOF paddle, a stop signal is sent to TDC, determining in this way a total flight time. For calculating the flight path, the tracking system is used; the particle velocity is calculated by dividing it by the time of flight. However, in order to obtain the time-of-flight more complicated procedures are necessary.

3.2.1 The Time-of-Flight Measurement Principle

A detailed picture of the TOF system of IMAX is presented in figure 3.11. Scintillation photons are generated at a given position within the TOF paddle. By successive reflections they travel to the paddle's end where they are detected by photomultipliers, two for each paddle. The position at which the photons are generated and the effective velocities at which they travel will affect the relative timing of the signals between the two photomultipliers.

The output anode signal of a PMT is directly connected to a discriminator where, in case that it is bigger than the threshold, it will be shaped in an ECL-Signal and further redirected to the Logic Module for obtaining the trigger. The discriminator threshold was set up at 15 mV, the typical amplitude for a minimum ionizing particle being above 100 mV. This setting of the threshold assures that a TOF measurement can not be started by noise signals but in the same time is low enough so that the "Time-walk" effect is being kept at negligible level [74].

Adopting the convention that north is the direction from the magnet to the tracker, with the scintillator paddles being perpendicular, the PMTs are arranged in East (E1-E3) and West (W1-W3) groups, this tagging being done north-wise. A minimal condition for a TOF measurement is the presence of at least one signal in any of the PMT groups indicated in table 3.1, that is the condition A∧B∧C∧D.

A:	T1E1 ∨ T1E2 ∨ T1E3	B:	T1W1 ∨ T1W2 ∨ T1W3
C:	T2E1 ∨ T2E2 ∨ T2E3	D:	T2W1 ∨ T2W2 ∨ T2W3

Table 3.1: Trigger configuration signals

The achievement of the trigger signal, apart from the fact that it must fulfill each of the above mentioned four conditions, it also has to happen in a time window of about 50 ns, this value being set on the basis of the propagation times

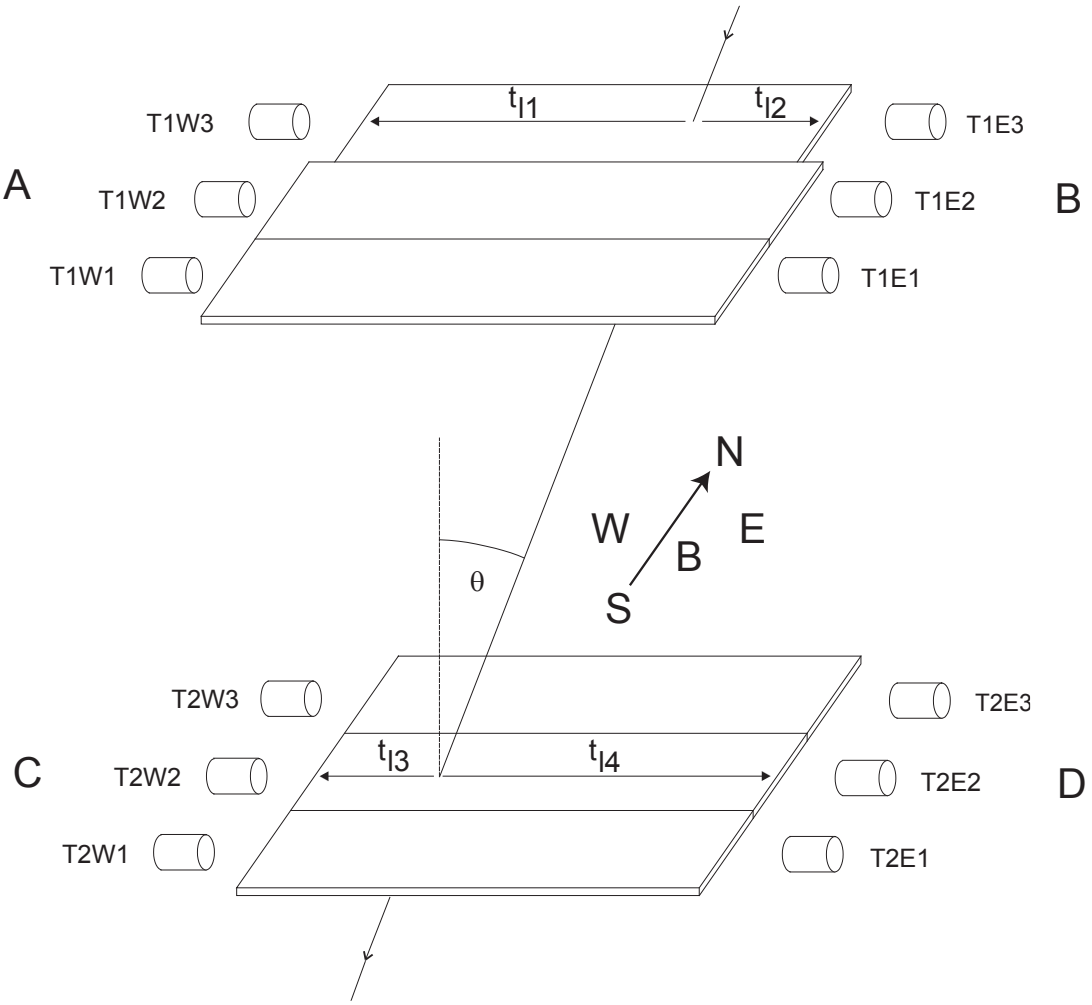

Figure 3.11: Schematical picture of IMAX TOF.

of signals inside the detector.

Figure 3.12 shows schematically the timing for one single event. The time labelled 1 in the picture refers to the particle hit in the upper scintillators. After a time t_{fl} the particle reaches the lower scintillators (time labelled 2) and signals in the PMTs are detected after times t_{l1}, t_{l2}, t_{l3} and t_{l4}. As a strobe signal (time labelled 3) for starting the coincidence window (K_{coi}) the signal C$\vee$D is used, meaning that at least a signal in the bottom TOF must be present, because the signals from A and B have a larger delay (K_{A1}, K_{B1}). This assures that casual perturbations in one of the bottom TOF photomultipliers still allows a trigger to be obtained.

In order to solve the ambiguity of the reference point of time measurement, which can vary with the strobe, the signal D is delayed (K_{del}) in such a way that the strobe will be always triggered by signal C. Once the coincidence is formed (time labelled 4) in the time window, the trigger for the TDCs is generated at the end of the coincidence window.

The advantage of using TDCs in a COMMON START mode with respect to the COMMON STOP mode is that the dead time is minimized. The STOP signals for TDCs are given by a second output of the discriminator and is delayed (K_{A2}, K_{B2}, K_{C2} and K_{D2}) in order to assure that it will not be released before the COMMON START signal. In this way the time t_3 measured from the east bottom TOF will always be constant, whereas the other times will vary with the incidence position in the paddle and the angle of the track.

According to figure 3.12 the four measured times by the TDCs can be expressed in the following manner:

$$\begin{aligned} t_1 &= t_{l1} + K_{A1} + K_{A2} - t_{fl} - t_{l3} - K_{C1} - K_{coi} \\ t_2 &= t_{l2} + K_{B1} + K_{B2} - t_{fl} - t_{l3} - K_{C1} - K_{coi} \\ t_3 &= t_{fl} + t_{l3} + K_{C1} + K_{C2} - t_{fl} - t_{l3} - K_{C1} - K_{coi} = c_3(ct.) \\ t_4 &= t_{fl} + t_{l4} + K_{del} + K_{D1} + K_{D2} - t_{fl} - t_{l3} - K_{C1} - K_{coi}\ . \end{aligned} \tag{3.19}$$

Considering that

$$t_{fl} = \frac{d_{FP}}{\beta c} \text{ and } t_{li} = \frac{s_i}{v_{eff}} \text{ for } i = \overline{1,4} \tag{3.20}$$

where d_{FP} is the flight path as calculated from the fitting procedure, s_i is the propagation distance from the impact point in the scintillator to the detection point of the photomultipliers, v_{eff} the effective propagation velocity of light in the scintillator, and adopting the following notation:

$$\begin{aligned} c_1 &= K_{A1} + K_{A2} - K_{C1} - K_{coi} \\ c_2 &= K_{B1} + K_{B2} - K_{C1} - K_{coi} \\ c_3 &= K_{C2} - K_{coi} \\ c_4 &= K_{del} + K_{D1} + K_{D2} - K_{C1} - K_{coi} \end{aligned} \tag{3.21}$$

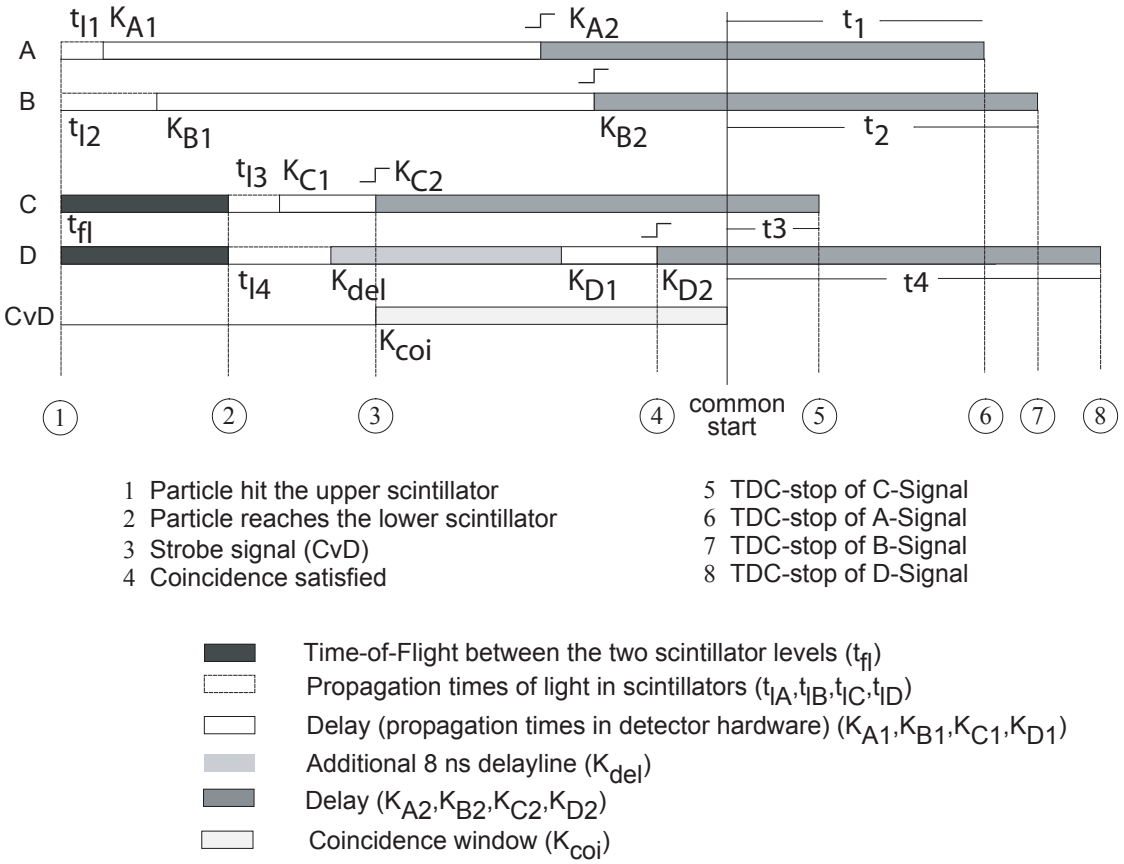

Figure 3.12: The measurement principle of TOF.

one obtains:

$$\begin{array}{rcl} t_1 &=& \frac{s_1}{v_{eff}} - \frac{d_{FP}}{\beta c} - \frac{s_3}{v_{eff}} + c_1 \\ t_2 &=& \frac{s_2}{v_{eff}} - \frac{d_{FP}}{\beta c} - \frac{s_3}{v_{eff}} + c_2 \\ t_3 &=& c_3 \\ t_4 &=& \frac{s_4}{v_{eff}} - \frac{s_3}{v_{eff}} + c_4 \, . \end{array} \tag{3.22}$$

The method to extract the time of flight from the above equations is to note that the paddle lengths $l_1 = s_1 + s_2$ and $l_2 = s_3 + s_4$ are constants and therefore the expression $t_3 + t_4 - (t_1 + t_2)$ can be evaluated. This is called the Difference-of-Sums (ΔS) and it is calculated from the four measured TDC times:

$$\Delta s = c_3 + c_4 - c_1 - c_2 + \frac{s_3 + s_4}{v_{eff}} - \frac{s_1 + s_2}{v_{eff}} + \frac{2 * d_{FP}}{\beta c} \, . \tag{3.23}$$

By grouping all the constants in a single term k one obtains that:

$$\Delta s = k + 2 * \frac{d_{FP}}{\beta c} \, . \tag{3.24}$$

This last equation must be slightly modified in order to express every terms in TDC channels. Each TDC has his own channels-to-time conversion number Δ_{TDC_i}, slightly different from each other but approximately equal to 30 ps/channel as stated in the technical specifications. Dividing the equation 3.24 by Δ_{TDC_i} with $i = \overline{1,9}$, one gets:

$$\Delta S_i = \frac{k}{\Delta_{TDC_i}} + \frac{2}{c \, \Delta_{TDC_i}} \cdot \frac{d_{FP}}{\beta} \, . \tag{3.25}$$

After noting the constant terms with K_{1_i} and K_{2_i} the equation 3.25 becomes:

$$\Delta S_i = K_{1_i} + K_{2_i} \cdot \frac{d_{FP}}{\beta} \, . \tag{3.26}$$

In this final form, ΔS_i is a known quantity constructed from the four measured times and d_{FP} is given by the tracker as a result of the fitting procedure. If both constants K_{1i} and K_{2i} are known then one can derive the velocity β.

3.2.2 Time-of-Flight Calibration

A method to determine the constants K_{1i} and K_{2i} consists in using particles of the same type, protons for convenience, propagating through the detector. By measuring their rigidity R, the velocity can be calculated according to the following equation:

$$\beta_{rig} = \frac{R}{\sqrt{Z^2c^2m_{pr}^2 + R^2}} \tag{3.27}$$

where m_{pr} indicates the mass of protons.

In this case, the Difference-of-Sums becomes:

$$\Delta S_i = K_{1_i} + K_{2_i} \cdot \frac{d_{FP}}{\beta_{rig}} \tag{3.28}$$

in which all quantities are known but the constants K_{1_i} and K_{2_i}. Thus, in case of a pure sample of protons, a scatter plot of ΔS_i vs. $\frac{d_{FP}}{\beta_{rig}}$ must have the points distributed along a straight line having as parameters the two constants.

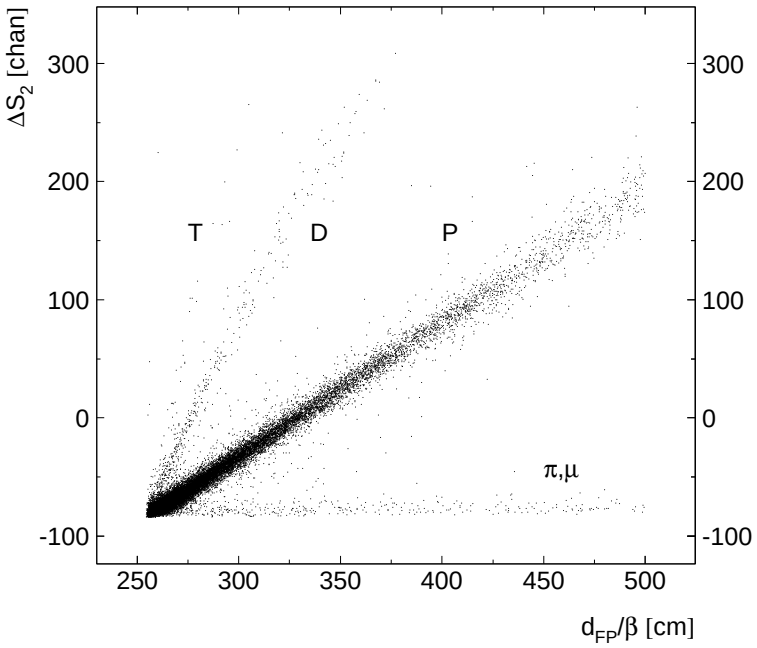

Figure 3.13: Difference-of-Sums scatter plot for paddle combination 2.

However, in practice it is not straight forward to obtain this sample of protons as shown in figure 3.13, because there are also other overlapping bands belonging

to deuterium, tritium and pions, since all these particles were also recorded during the flight. The helium particles were removed from this plot because a rough estimation of the charge can be done at this point using only the upper TOF scintillator with the method ADC vs. η^2 (see section 3.3). Clearly the most abundant particles are protons.

A method to extract only protons from the data is to perform an iterative procedure. Firstly, a rough graphical cut selects protons on the scatter plot ΔS vs. $\frac{d_{FP}}{\beta_{rig}}$, with the β_{rig} obtained assuming the proton mass for all events. After fitting the data with a straight line, a new improved cut is made by selecting only events within a 5σ time-resolution band (5*122 ps equivalent to 20 TDC channels [74]) around the calibration line. The fitting is repeated until the line parameters converge to constant values.

This procedure was used also in this work but the constants determined in this way turned out to be not accurate enough, resulting in a worse mass resolution and a shift in the mass histograms peaks off their correct value, especially at energies above 1 GeV/nuc. Since this effect appeared especially at high energies, where the influence on the mass measurement precision is dictated by the velocity resolution (see chapter 4.2), the shift was attributed to the determination of TOF constants K_{1_i} and K_{2_i}. This led to a re-evaluation of the calibration constants by means of an improved procedure.

A proton sample of better quality was obtained by performing a mass selection, as described further in chapter 4 by using the calibration constants calculated with the first method. Tracks with better quality criteria were also chosen by imposing stronger cuts on the track fitting. Moreover, a fit on the points only in the middle energy domain relevant for this work, from 400 to 1000 MeV/nuc, assures that the high-energy protons does not affect the result, since in this energy domain the measured difference-of-sums are less and less accurate and the sample is also contaminated by other singly charged particles. The low energy domain for this work, from 100 to 400 MeV/nuc, was also excluded since the rigidity is worsening due to multiple scattering (see chapter 4.1) and in addition there is insufficient statistics in order to provide reliable support points for fit-

$$
\begin{gathered}
0.6\ amu < Mass < 1.5\ amu \\
N_x > 15 \\
N_y > 8 \\
\chi^2_{x,y} < 2 \\
0.4\ \tfrac{GeV}{nuc} < E_{kin} < 1\ \tfrac{GeV}{nuc} \\
\Delta\eta < 0.07\ GV
\end{gathered}
$$

Table 3.2: Cuts used to select the protons for the calibration of TOF

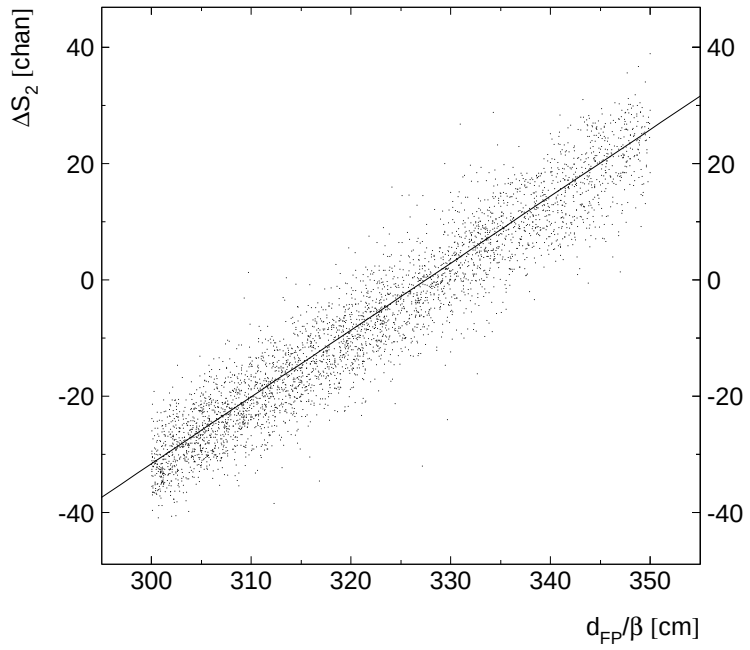

Figure 3.14: Proton band from paddle combination 2, selected for the calibration line of TOF.

ting the calibration lines. The set of cuts used to select the proton sample is summarized in table 3.2.

By performing the fit for the nine paddle combinations a new set of constants was obtained (table 3.3). A fit example for the paddle combination no. 2 is presented in figure 3.14.

Paddle combination	$K_1[chan/cm]$	$K_2[chan]$
1	- 382.25	1.1673
2	- 376.52	1.1497
3	- 390.01	1.1426
4	- 396.92	1.1584
5	- 395.52	1.1498
6	- 409.37	1.1463
7	- 391.61	1.1497
8	- 394.19	1.1555
9	- 403.78	1.1339

Table 3.3: Calibration constants for TOF.

With the velocity calculated in this fashion it is extremely important to in-

fer the timing resolution, since this affects in a decisive way the overall mass separation performance of the instrument (chapter 4.2).

One method to obtain it is to select one type of particles whose times of flight should be constant and to check the standard deviation of the measured times of flight around this value. This can be achieved by selecting only singly charged events (section 3.3) and also with high rigidities R > 15 GV. The kinetic energies of those events should be higher than 14 GeV/nuc for protons and therefore the beta would be essentially 1. At those rigidities, the tracks are practically straight lines and the influences on the flight path due to different penetrating angles in the instrument are not greater than 3% of the 2.54 m, namely the length top TOF - bottom TOF. Consequently, one would expect for such events a time of flight of 8.47 ns ($2.54 \cdot c^{-1}[m/s]$). The measured times of flight histogram for the events selected in this fashion is presented in figure 3.15 and it is described very good by a gaussian distribution with a mean value of 8.47 ns. The time resolution for singly charged particles with the IMAX experiment was found to be 159 ps.

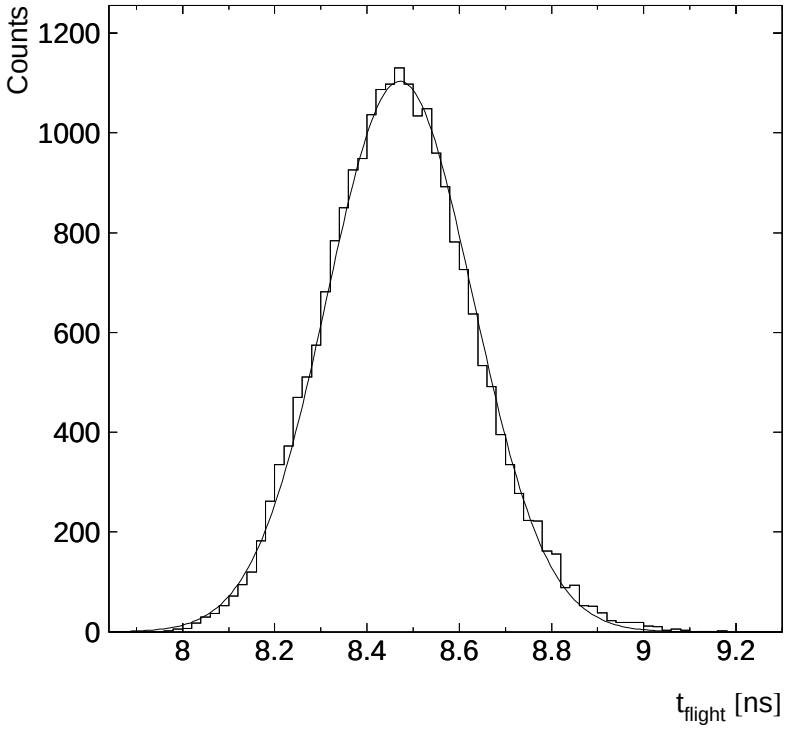

Figure 3.15: Time resolution with the IMAX instrument for singly charged particles: $\sigma_t = 159ps$.

A very useful information which can be inferred from the time-of-flight measurement is the impact position X_{TOF} in the scintillator paddles. Since the

lengths of the paddles are known, one can calculate from the differences $t_1 - t_2$ and $t_3 - t_4$ the effective velocity of light v_{eff} in scintillators [61], which was found to be around $1.5 \cdot 10^8 \ m/s^2$. By comparing the above mentioned time differences with the extrapolated points of the track X_{Track} from the drift chambers to the TOF scintillator paddles, one can thereafter calculate the impact position with a precision of 1.4 cm.

By choosing events with kinetic energies higher than 10 GeV/nuc, where the multiple scattering does not play a significant role (see chapter 4.1), the precision of the extrapolated track points from the drift chambers to the top-TOF paddles becomes approximately 1 mm and therefore the positions obtained this way can be considered as a reference.

In figure 3.16 it is presented the position resolution for the top-TOF measurement as calculated from the difference $X_{TOF} - X_{Track}$. The comparison between the two measured impact points, X_{TOF} and X_{Track} is very useful in removing events with irrelevant velocity measurements by requiring them to have a position agreement inside a 3-σ interval around the extrapolated impact position, for both top and bottom TOF (see chapter 4.2).

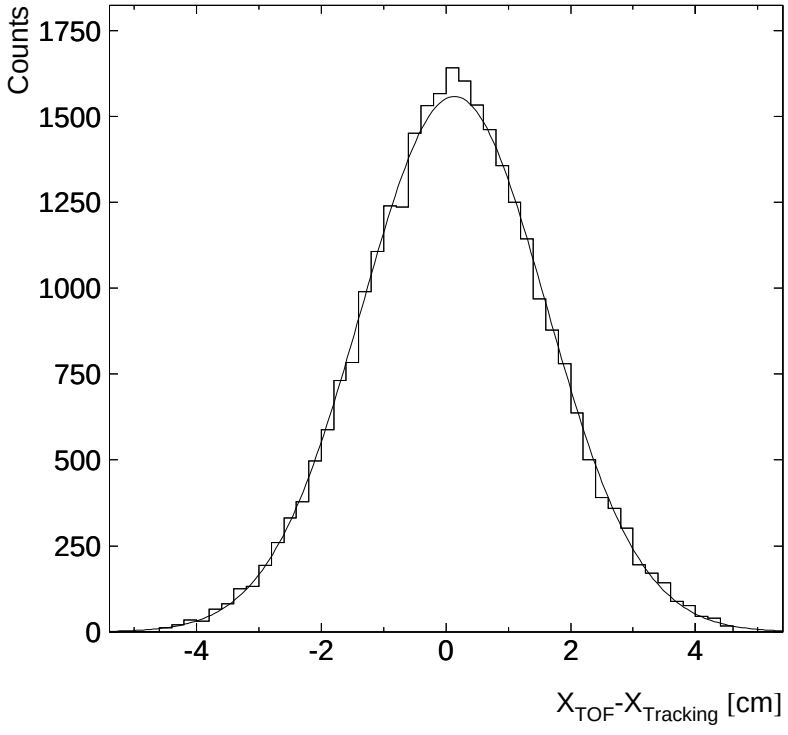

Figure 3.16: Resolution of the top-TOF position measurement: $\sigma_{X,TOF} = 1.4\,cm$.

3.3 Charge Separation

The charge measurement is achieved by measuring the deposited energy in each of the IMAX four scintillators, expressed in *ADC* channels. Performing scatter plots of the type *ADC* vs. *ADC*, samples of the same charge can be separated and finally "real" charges can be ascribed to events, for each of the four scintillators. The overall charge for each event is determined by performing a four fold coincidence within specific charge cuts and therefore the efficiency and contamination have also to be determined.

3.3.1 Charge Determination

A charged particle traversing matter within the energy domain relevant for this experiment, 200 to 1800 $MeVnuc^{-1}$, loses energy mainly by ionization and excitation. According to Bethe and Bloch the average energy loss dE per unit length dx (g/cm^2) due to those processes is given by:

$$-\frac{dE}{dx} = 4\pi N_A r_e^2 m_e c^2 \frac{z}{a}\frac{Z^2}{\beta^2}\left[ln\left(\frac{2m_e c^2\gamma^2\beta^2}{I} - \beta^2 - \frac{\delta}{2}\right)\right] \tag{3.29}$$

where

Z	charge of the penetrating particle in units of the elementary charge
z, a	atomic number and atomic weight of the absorber
$m_e = 0.511\ MeV/c^2$	electron mass
$r_e = 2.818\ fm$	classical electron radius $\left(r_e = \frac{1}{4\pi\epsilon_0}\cdot\frac{e^2}{m_e c^2}\right)$ with ϵ_0 - permittivity of free space
$N_A = 6.022\cdot 10^{23}\ mol^{-1}$	Avogadro number
I	ionization constant characteristic to the absorber material
δ	parameter responsible for the density effect

For the Bicron scintillator which are used in IMAX the minimal energy loss by excitation and ionization is around 2 $MeVg^{-1}cm^2$ and the average excitation energy is approximately 100 eV [65]. The collected photons, which can be over $2\cdot 10^4$ according to the above considerations, are detected by photomultipliers and finally the outgoing signals are integrated in *ADC* Lecroy units. A series of corrections have to be performed on the raw signal, as the subtraction of the temperature dependent dark currents and correction for dependency on the

incidence position in scintillator [61]. After the corrections, the measured ADC signal is directly related to the deposited energy in the scintillator.

The key feature of relation 3.29 with respect to a charge measurement is the dependency of the deposited energy on the squared charge of the incident particle. However, a histogram of the energy loss is not enough to separate the charges since there is also a squared beta dependency. A way to identify particles of the same charge is to perform scatter plots ADC vs. β^2 or ADC vs. η^2, shown in figure 3.17.

By observing the features of the two scatter plots, one can notice the separation in charge bands in the case of the first plot and a further separation in mass bands in the case of the second one. In principle both quantities could be used for determining the charge but it is clear that the separation of bands at high energies has better quality in the beta representation. Therefore in the analysis for the charge determination the beta representation was used.

A method to perform the charge selection consists in building charge bands with parabolic functions and then ascribing to each event an integer charge if the energy loss lies between their limits. This procedure is less complicate but it has the disadvantage that the charge bands can not be satisfactorily adjusted in order to optimize the selection efficiency and contamination.

For this analysis a more refined method was used. The first step was to select event samples of a specific charge in all four scintillators, independently from the energy. This can be achieved by performing graphical cuts on scatter plots ADC vs. ADC from different scintillators. Since there are four ADC measurements for each event (S1, S2, TOFT and TOFB), in principle six scatter plots can be built; the three scatter plots used for the selection were ADC from top-TOF versus ADC from scintillators S1, S2 and bottom-TOF (figure 3.19). It can be noticed in figure 3.19 that domains of particles with the same charge are separated, with the helium particles being the events grouped in the upper zone.

From figure 3.17 it is clear that the main problem in selecting a sample of particles with the same charge is that at high energies singly charged particles start to contaminate the helium band due to the Landau fluctuations. Moreover, events with wrong beta measurement may be ascribed to the wrong sample. By performing ADC versus ADC scatter plots, events showing large fluctuations of the energy released in one of the scintillators are clearly separated from the bulk of events and can be easily removed from the sample. At low energies the average energy loss increases (see relation 3.29) and singly charged events in this representation may in principle contaminate the helium sample.

Nevertheless it can be noticed in figure 3.19 that the $Z = 1$ band is bent and the bending increases going from the upper to the lower plot. The reason is that with increasing amount of material between two scintillators, as in the case of top-TOF to S2 or bottom-TOF, the energy loss becomes more and more important and the velocity difference in the two scintillators becomes significant, resulting in a larger energy loss in the lower scintillator.

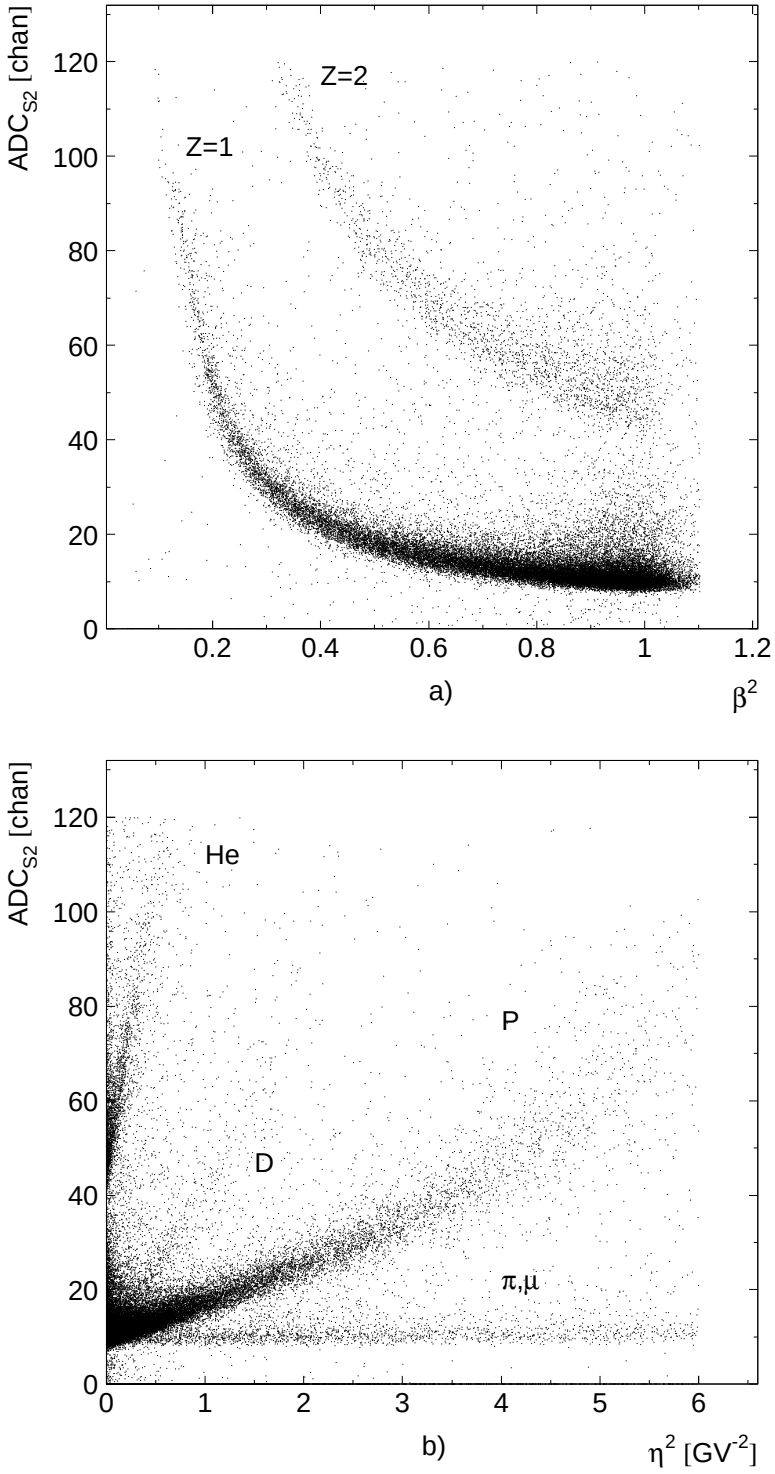

Figure 3.17: The energy loss in the scintillator S2 versus a) squared beta and b) squared deflection.

In order to diminish the afore mentioned contamination of helium samples at low energies, ADC scatter plots scaled with the squared beta can be used in addition to the ADC scatter plots already mentioned. As it is noted in equation 3.29, the product between the energy loss and squared beta is not dependent anymore on the energy but one has to remember that the measured velocity represents an average from top-TOF to bottom-TOF and therefore it does not correspond exactly to the velocity in each scintillator.

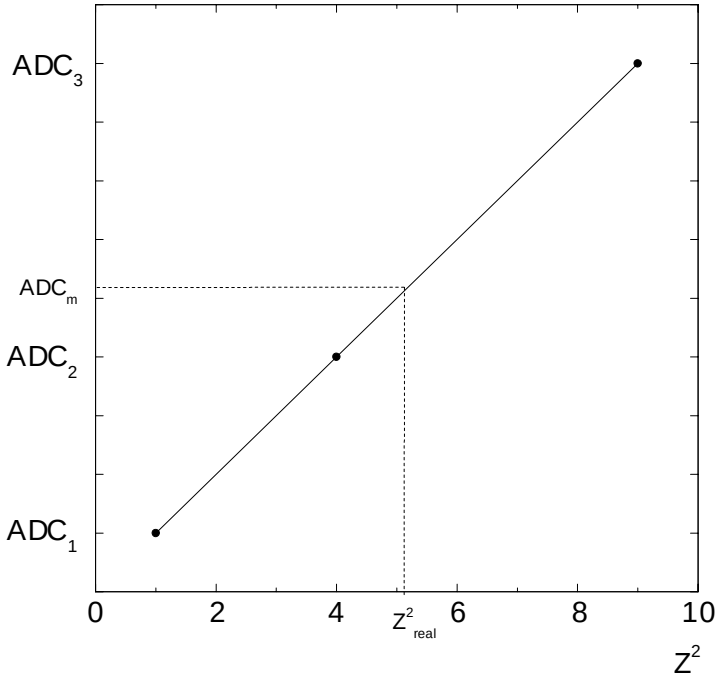

Figure 3.18: Schematic representation of the interpolation for ascribing a "real" charge to an ADC measurement.

Thus, for this kind of representation were chosen scintillator groups with the least amount of material between them, such that the velocity differences are kept at a minimal level (figure 3.20). The charge separation for events belonging to the low energy domain is evident. In this way, a solid coincidence between six scatter plots was used for the choice of each sample by means of graphical cuts (figures 3.19 and 3.20).

By using the method described above clean samples of $Z = 1$ and $Z = 2$ particles were selected and ADC vs. β^2 plots were built for all the four scintillators (figure 3.21).

With the charge curves obtained from fitting polynomial functions to the scatter plots, "real" charges could be ascribed to events according to the measured ADC_m in each scintillator, by means of a linear interpolation as shown in figure

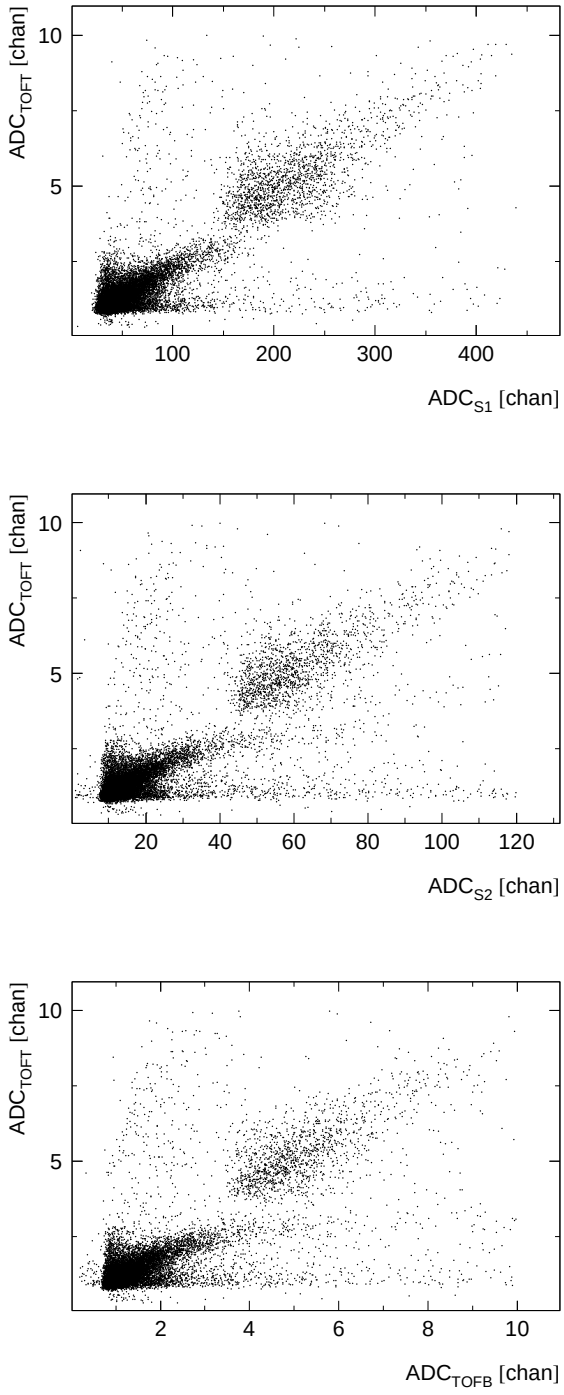

Figure 3.19: Energy loss scatter plots used for charge sample determination.

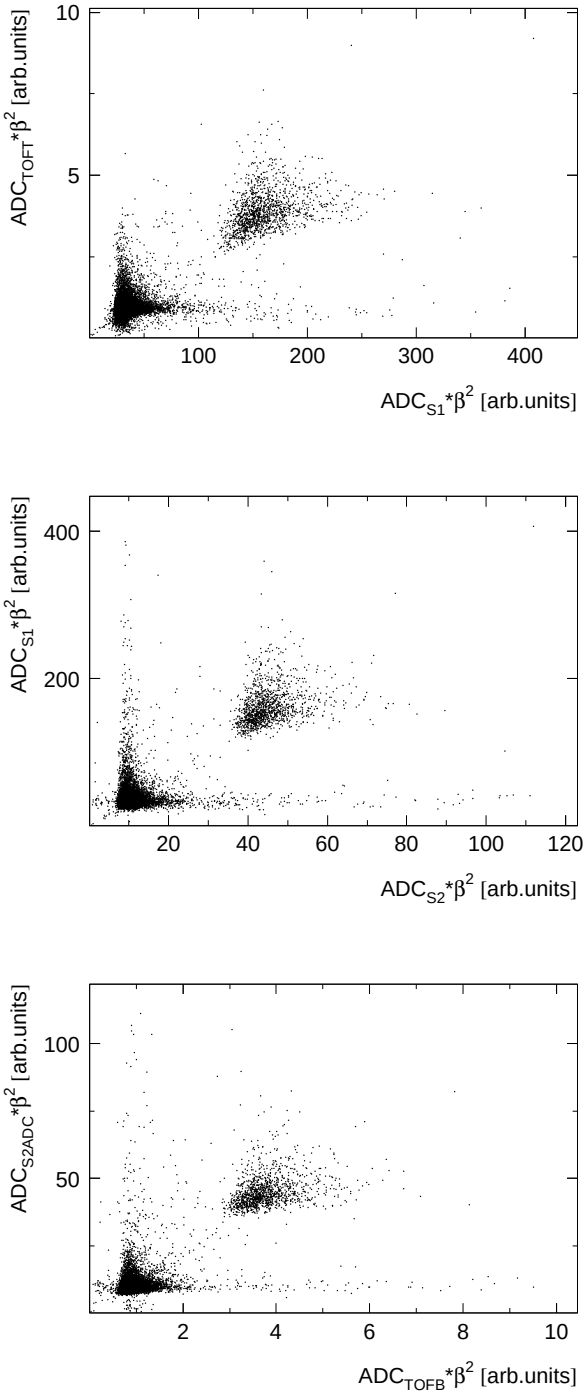

Figure 3.20: Scatter plots of energy loss scaled with squared beta used for determining charge samples.

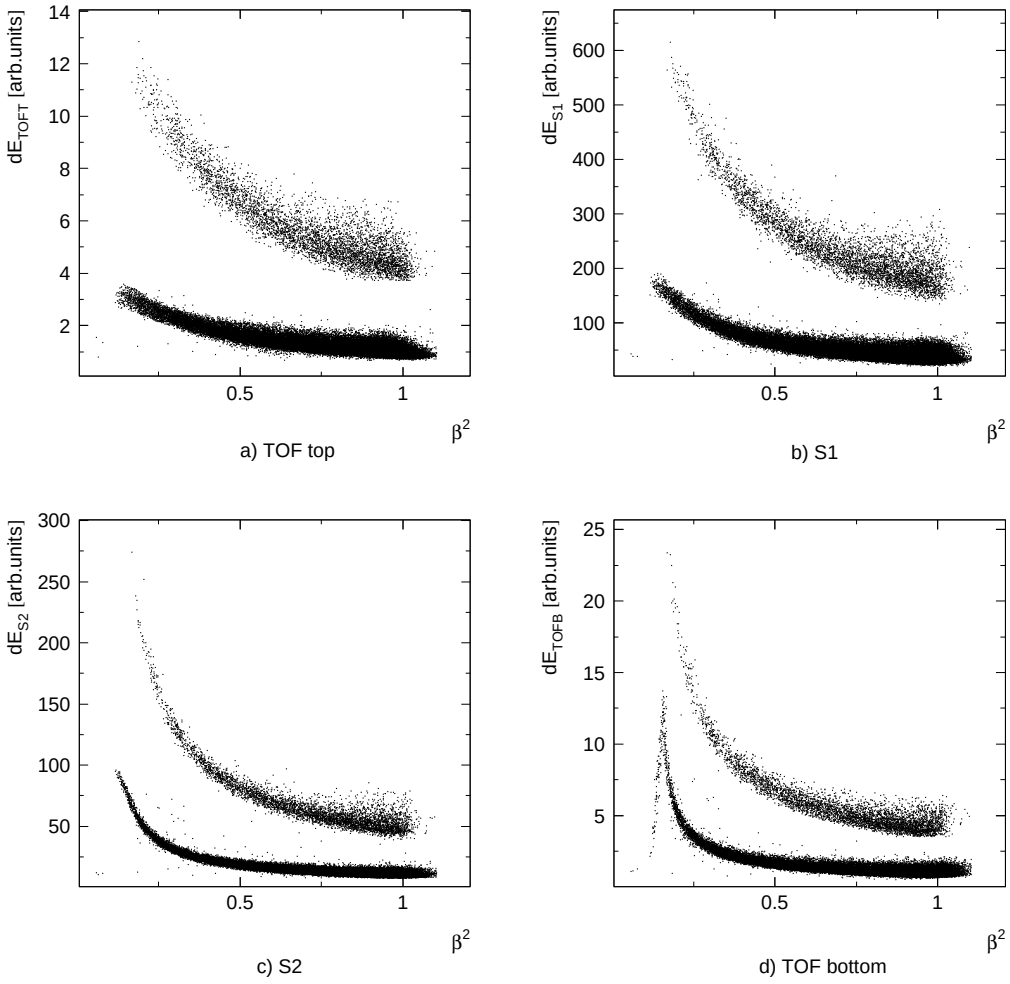

Figure 3.21: Samples chosen for charge bands fitting in all four scintillators.

3.18. The following parametrization has been used:

$$Z_{real} = \begin{cases} \sqrt{1 + 3 \cdot \dfrac{ADC_m - ADC_1}{ADC_2 - ADC_1}} & \text{if} \quad ADC_m \leq ADC_2 \\ \sqrt{4 + 5 \cdot \dfrac{ADC_m - ADC_2}{ADC_3 - ADC_2}} & \text{if} \quad ADC_m > ADC_2 \end{cases} \tag{3.30}$$

where ADC_Z, $Z = 1, 2, 3$, are the ADC values corresponding to the fitted charge curves of protons, helium and lithium and to the measured velocity β. In the case of $Z = 3$, the charge curve has been obtained from the $Z = 2$ one, scaled with the factor $3^2/2^2 = 2.25$.

The charge histograms are presented in figure 3.22 for all four scintillators. As it was expected from the distribution of the energy loss around the Bethe-Bloch average values, the charge histograms are not gaussian-like but rather show Laundau tails, which is to be expected considering the scintillator small thickness.

The charge curves are thought to follow the average energy loss and one can notice from the histogram shapes that this could be the case for all scintillators except the top-TOF one. The explanation could be based on the fact that the velocity of the less massive muons and pions is especially affected while traversing the instrument. Accordingly, their ascribed velocity in top-TOF scintillator, which is in fact an averaged one, is systematically lower than the true one. This might lead to a widening of the charge bands for this kind of particles on an ADC vs. β^2 scatter plot, which translates itself into a lower measured charge.

Although more and more negligible as the incident particles are more massive, this effect is still present, therefore in principle a bias in the isotopic ratio is possible. Nevertheless, as it will be presented in the next section, the charge cut will be considered large enough in order to exclude a bias into the isotopic ratio due to this effect.

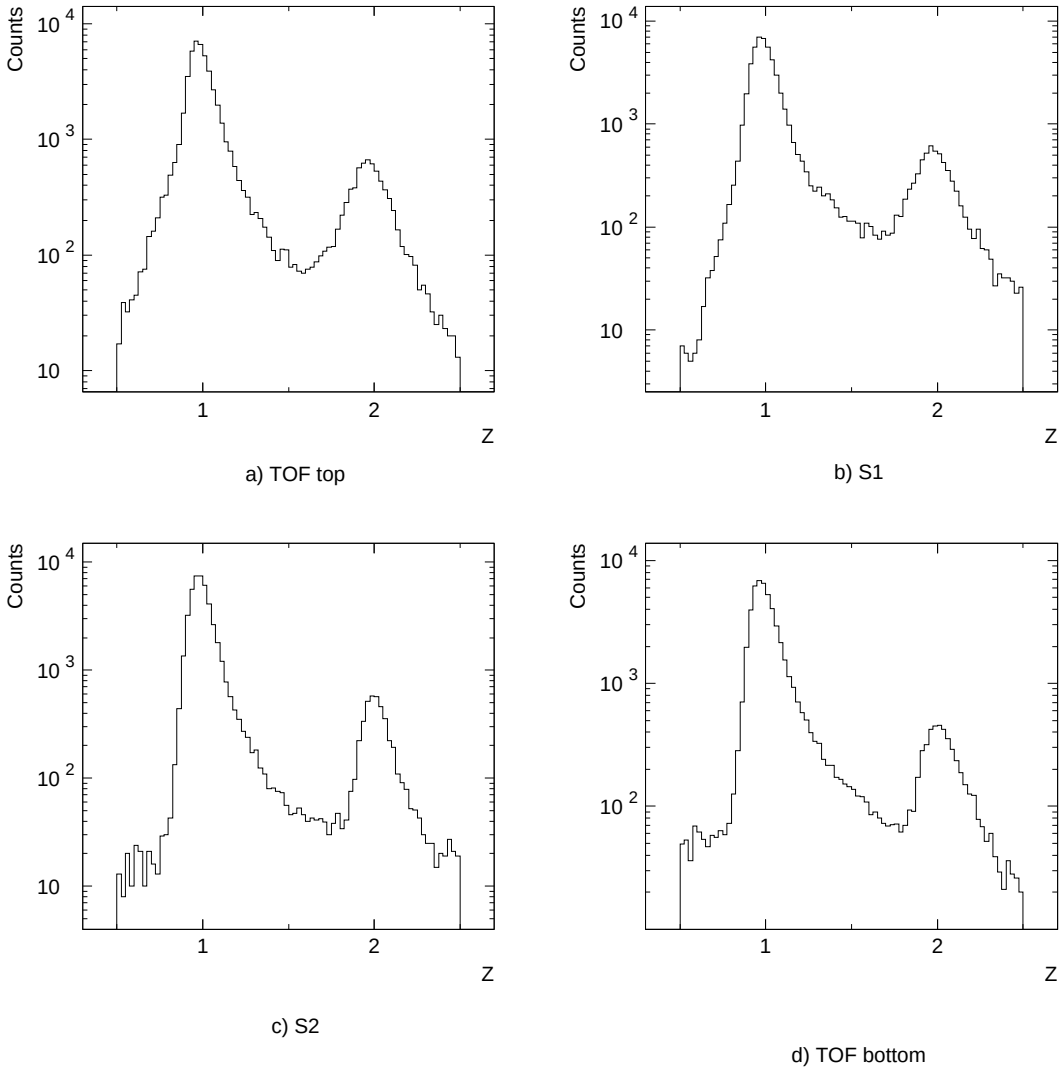

Figure 3.22: Charge histograms in all four scintillators.

3.3.2 Efficiency and Contamination of the Charge Selection

An important point in determining the charge of an event is that, according to the Bethe-Bloch relation, the deposited energy in scintillators does not dependent on the mass of the incident particle. This fact points out that the measured deposited energy is distributed independently of the mass around the average values of Bethe-Bloch. Therefore, an important assumption for the present analysis is that a charge cut do not introduce a bias in the deuteron-to-proton ratio.

The choice of the charge cuts must fulfill the following requirements: good efficiency and negligible helium contamination. The efficiency of a charge cut in selecting a specific charge is defined as the probability that the measured charge lies inside that cut:

$$EFF = \frac{n_{inside\ cut}}{N_{ref}} \tag{3.31}$$

where $n_{inside\ cut}$ is the number of events inside the cut and N_{ref} is the number of events in a reference sample of events, which are known to have that specific charge.

The notion related to the efficiency is the contamination in a charge cut with any unwanted charges. The contamination in a specific charge cut is actually the efficiency of the same cut with respect to different charges. Therefore, considering a reference sample with charges different than in the case of efficiency, the contamination can be defined as the probability that the measured charge lies inside the cut.

$$CON = \frac{m_{inside\ cut}}{M_{ref}}. \tag{3.32}$$

Here $m_{inside\ cut}$ is the number of events inside the cut and M_{ref} is the number of events in a reference data set, which are known to have a different charge than in the case for efficiency.

For our particular case, if one wishes to calculate efficiency and contamination for proton charge cuts, the reference data set will be made of protons for the first task and of helium in the second. IMAX can offer four possible independent charge measurements and therefore when a charge cut for a scintillator is studied, the other three can be used to obtain the reference sample. For a proton reference sample a three-fold coincidence was used because the helium contamination is brought to a minimal level. The same is valid for the choice of a helium sample. The charge cuts used for choosing the reference samples were $1 \pm 0.3\bar{e}$ for protons and $2 \pm 0.3\bar{e}$ in the case of helium.

Considering that $n_{inside\ cut}$ and $m_{inside\ cut}$ are binomial distributed with the probabilities EFF and CON it follows that the errors for the efficiency and con-

tamination are:

$$\begin{aligned} \Delta EFF &= \sqrt{\frac{EFF(1-EFF)}{N_{p,ref}}} \\ \Delta CON &= \sqrt{\frac{CON(1-CON)}{M_{He,ref}}}. \end{aligned} \tag{3.33}$$

By studying different charge cuts, it was finally adopted the following charge cuts: $1 \pm 0.6\bar{e}$ for protons and $2 \pm 0.2\bar{e}$ for helium. In figures 3.23 and 3.24 are plotted the efficiencies and contaminations for the above mentioned charge cuts.

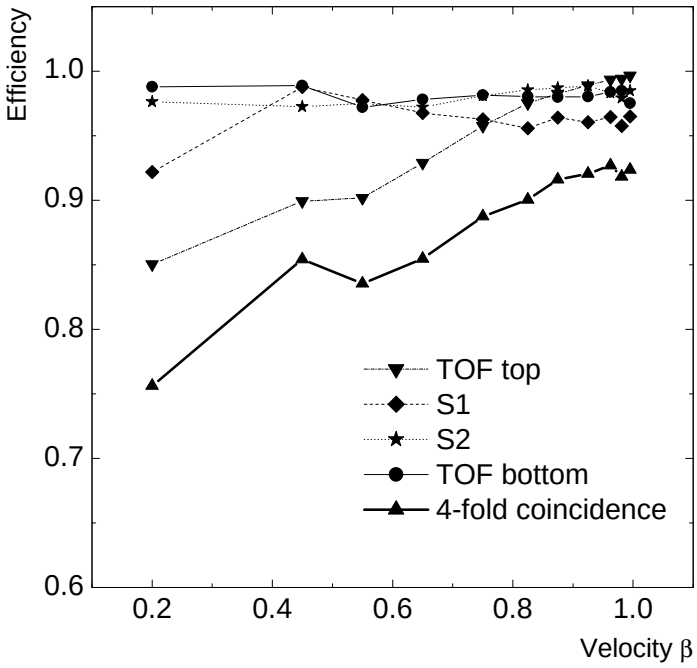

Figure 3.23: Charge efficiency in all four scintillators for protons with a charge cut $1 \pm 0.6\bar{e}$.

The charge cuts for protons are rather loose if one considers the charge histograms from figure 3.22. This choice is meant to prevent a possible influence on the isotopic ratios for singly charged particles. Especially at low energies, where the energy loss is more important with respect to the total kinetic energy, an average measured velocity can be systematically different for two incident particles, a deuterium and a proton, if they penetrate the instrument with the same

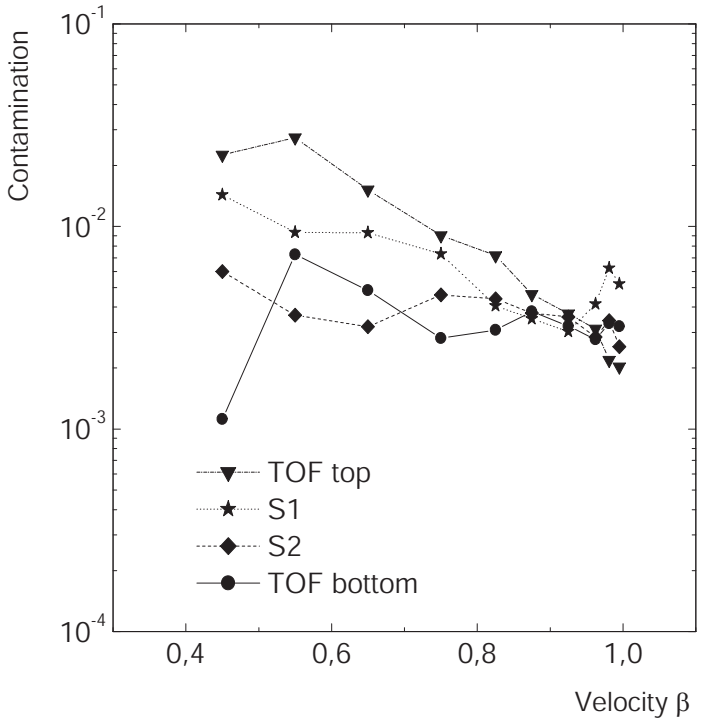

Figure 3.24: Contamination of the proton band with helium in case of a charge cut $1 \pm 0.6\bar{e}$ in all four scintillators.

incident beta. A loose cut around the charge band, which is determined in fact by protons because they are more numerous, will eliminate such possible "fine structures" of the Bethe-Bloch plots.

The efficiency reached by a four fold coincidence is mainly situated around 90% for the velocity domains important in this analysis ($\beta > 0.5$) while the contamination is kept at the level of 10^{-9}. For the statistics involved in the present analysis, around 10^6 events, such a contamination level is practically negligible. The difference in efficiency for the top-TOF with respect to the other three, visible in the low energy domain, could be explained with the same considerations as in the previous section, when the charge histogram for top-TOF was discussed (figure 3.22). Since for the present analysis the choice of charge cuts in the case of helium is of less importance, only the efficiency and contamination for the proton charge cuts are presented in table 3.4.

Velocity	Scintillator	EFF	CON($*10^{-2}$)
$\beta = 0.45$	TOF top	0.89 ± 1.1%	3.25 ± 12.6%
	S1	0,97 ± 0.5%	1.43 ± 19.2%
	S2	0,98 ± 0.4%	0.62 ± 29.8%
	TOF bot	0.98 ± 0.3%	0.11 ± 69.3%
	4-fold coincidence	0.85 ± 1.3%	$2.16*10^{-7}$ ± 78.9%
$\beta = 0.55$	TOF top	0.90 ± 0.7%	3.75 ± 6.0%
	S1	0,97 ± 0.3%	0.93 ± 12.2%
	S2	0,97 ± 0.3%	0.36 ± 19.6%
	TOF bot	0.97 ± 0.4%	0.72 ± 13.9%
	4-fold coincidence	0.83 ± 1.0%	$6.8*10^{-7}$ ± 27.7%
$\beta = 0.65$	TOF top	0.93 ± 0.5%	2.51 ± 4.5%
	S1	0,97 ± 0.3%	0.93 ± 7.5%
	S2	0,96 ± 0.3%	0.32 ± 12.9%
	TOF bot	0.97 ± 0.2%	0.48 ± 10.5%
	4-fold coincidence	0.85 ± 0.7%	$2.1*10^{-8}$ ± 18.8%
$\beta = 0.75$	TOF top	0.96 ± 0.3%	1.90 ± 4.0%
	S1	0,98 ± 0.2%	0.73 ± 6.5%
	S2	0,96 ± 0.3%	0.46 ± 8.3%
	TOF bot	0.98 ± 0.2%	0.28 ± 10.6%
	4-fold coincidence	0.88 ± 0.5%	$8.5*10^{-8}$ ± 15.5%
$\beta = 0.825$	TOF top	0.97 ± 0.2%	0.92 ± 7.4%
	S1	0.98 ± 0.2%	0.40 ± 11.2%
	S2	0.95 ± 0.3%	0.44 ± 10.8%
	TOF bot	0.98 ± 0.2%	0.30 ± 12.9%
	4-fold coincidence	0.90 ± 0.5%	$3.9*10^{-8}$ ± 21.6%
$\beta = 0.875$	TOF top	0.98 ± 0.2%	0.63 ± 8.0%
	S1	0.98 ± 0.1%	0.35 ± 10.8%
	S2	0.96 ± 0.2%	0.37 ± 10.4%
	TOF bot	0.97 ± 0.2%	0.38 ± 10.4%
	4-fold coincidence	0.91 ± 0.4%	$2.3*10^{-8}$ ± 20.0%
$\beta = 0.925$	TOF top	0.98 ± 0.1%	0.27 ± 12.5%
	S1	0.98 ± 0.1%	0.30 ± 11.8%
	S2	0.96 ± 0.2%	0.35 ± 10.9%
	TOF bot	0.98 ± 0.1%	0.32 ± 11.4%
	4-fold coincidence	0.92 ± 0.3%	$1.2*10^{-8}$ ± 23.4%
$\beta = 0.962$	TOF top	0.99 ± 0.1%	0.11 ± 27.8%
	S1	0.98 ± 0.1%	0.41 ± 14.4%
	S2	0.96 ± 0.2%	0.28 ± 17.4%
	TOF bot	0.98 ± 0.1%	0.27 ± 17.6%
	4-fold coincidence	0.92 ± 0.3%	$1.0*10^{-8}$ ± 40.0%
$\beta = 0.981$	TOF top	0.99 ± 0.1%	0.11 ± 40.3%
	S1	0.97 ± 0.2%	0.62 ± 17.5%
	S2	0.95 ± 0.3%	0.34 ± 23.6%
	TOF bot	0.98 ± 0.2%	0.33 ± 24.0%
	4-fold coincidence	0.91 ± 0.4%	$1.5*10^{-8}$ ± 55.4%
$\beta = 0.995$	TOF top	0.98 ± 0.1%	0.03 ± 73.9%
	S1	0.98 ± 0.2%	0.52 ± 26.0%
	S2	0.96 ± 0.3%	0.25 ± 37.2%
	TOF bot	0.97 ± 0.3%	0.32 ± 33.1%
	4-fold coincidence	0.92 ± 0.5%	$8.6*10^{-8}$ ± 92.9%

Table 3.4: Efficiency and contamination for the charge cuts Z=1.

Chapter 4

Hydrogen Isotopic Ratios in the Instrument

This chapter provides the isotopic ratios measured in the IMAX instrument for singly charged nuclei: protons, deuterons and tritons, prior to any instrumental corrections. A thorough analysis concerning the choice of different quality and geometry cuts will be performed with the aim of leaving those ratios unaffected. By using the incident velocity and deflection spectra together with the time-of-flight resolution and sigma-deflection distribution it was possible to develop a Monte Carlo simulation to reproduce the measured mass histograms.

4.1 Mass Resolution for Singly Charged Isotopes with IMAX

In the previous chapter I have presented how the measurements of rigidity, velocity and charge are performed with the IMAX detectors. These measurements allow us to calculate the mass, according to the formula 2.3. The separation of particles in mass bands can already be observed on a beta vs. rigidity scatter plot, as shown in figure 4.1, where the plotted data are selected using minimal requirements for the track selection (see section 4.2). The mass bands become distinguishable because charged particles penetrating the magnetic field with the same velocity will manifest different rigidities, according to their mass. For instance, the mass band of tritium is located in the right extreme of the plot, whereas the pions and muons are to be seen in the upper left zone.

The separation in bands can be improved, depending on the severity of the imposed selection cuts over the tracks quality. However, from the scatter plot shown in figure 4.1, it is clear that a mass separation could be achieved at least for rigidities up to 3 GV. Above this energy, one can see that the bands begin to overlap and therefore in order to improve the mass resolution further cuts are

usually applied. As I will show in section 4.2 the use of track quality cuts has to be done with extreme care since the isotopic ratio could be affected.

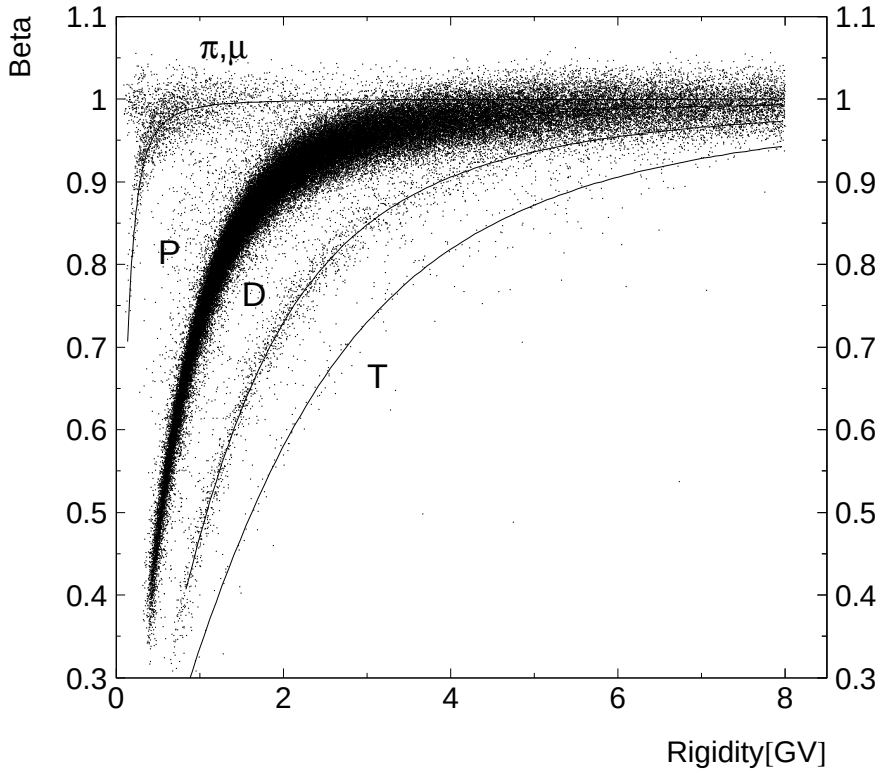

Figure 4.1: Beta vs. rigidity representation for singly charged particles. The pions and muons, protons, deuterons and tritons can be separated in distinct bands.

A quantitative estimation of the mass error can be obtained analytically by performing error propagation in equation 2.3, assuming that the charge is measured exactly:

$$\sigma(M) = M\sqrt{\gamma^4 \left(\frac{\sigma(\beta)}{\beta}\right)^2 + \left(\frac{\sigma(\eta)}{\eta}\right)^2}. \tag{4.1}$$

The velocity β of an incident particle is the ratio of the flight path d and the time of flight t:

$$\beta = \frac{d}{t \cdot c}. \tag{4.2}$$

Considering that the error in the flight path d can be neglected, it follows that the relative error of the velocity will be:

$$\frac{\sigma(\beta)}{\beta} = \frac{\beta c}{d}\sigma(t) \tag{4.3}$$

where the time of flight resolution is $\sigma(t) = 159\,ps$, as presented in chapter 3.2, and the flight path is $d = 254\,cm$.

To write the deflection error one has to take into account two contributions: one due to the track measurement error $\sigma_{track}(\eta)$ (relation 3.14) and the other due to multiple scattering $\sigma_{ms}(\eta)$. The multiple scattering denotes the interaction of charged particles traversing the matter with the Coulomb potentials of nuclei and electrons. This leads to a certain number of scattering processes depending on the amount of material traversed by the charged particle, with low deviations from the original trajectory. The multiple scattering contribution and the track measurement error are independent from each other and therefore the overall deflection error is:

$$\sigma^2(\eta) = \sigma^2_{track}(\eta) + \sigma^2_{ms}(\eta). \tag{4.4}$$

According to [36], in the limit of small scattering angles, the relative error of the deflection measurement due to multiple scattering is:

$$\frac{\sigma_{ms}(\eta)}{\eta} = \frac{\sqrt{x/X_0}\cdot(1+0.0038\cdot ln(x/X_0))}{\beta\cdot\int \vec{B}\times\vec{dl}}\cdot 5.23\times 10^{-2}\frac{Vs}{m}. \tag{4.5}$$

Here, the field integral $\vec{B}\times\vec{dl}$ which was already presented in figure 3.9, has the average value of $0.29\ T\cdot m$. The ratio x/X_0 represents the thickness of the scattering medium, measured in units of the radiation length. The tracking detector, consisting of drift chambers and MWPCs, can be considered as a succession of five layers of different mass, thickness and radiation length, as presented in table 4.1.

	Material	Vertical Path $[g/cm^2]$	Radiation length $[g/cm^2]$
DC CO_2	CO_2	0.13	36.2
DC Mylar	Mylar	0.0695	40.0
DC Copper	Scintillator	0.1254	12.9
MWPC Argon	Ar	0.0512	19.55
MWPC Mylar	Mylar	0.0353	40.0

Table 4.1: Approximate vertical depth of the IMAX tracking detector.

Therefore, the numerator of the relation 4.5 can be replaced with:

$$\sqrt{\sum_{i=1}^{5}\left(\sqrt{\frac{x_i}{X_{0i}}}\cdot\left(1+0.038\cdot ln(\frac{x_i}{X_{0i}})\right)\right)^2}=0.109. \tag{4.6}$$

These observations allow us to express the multiple scattering error in a similar way as for the tracking error, namely by using the concept of a MDR:

$$\frac{1}{\sigma_{ms}(\eta)}=MDR_{ms}=\frac{\beta\cdot R}{0.0197}. \tag{4.7}$$

The characteristic feature of MDR_{ms} is that, on contrary as in the MDR_{track} case, it increases with energy. This dependence indicates that the multiple scattering contributes to the relative error of deflection especially in the low energy domain, where the value of MDR_{ms} decreases.

Taking into account all the relations 4.7, 4.4 and 4.3, the expression 4.1 of the mass resolution can be rewritten as:

$$\sigma(M)=M\sqrt{\gamma^4\frac{\beta^2c^2}{d^2}\sigma^2(t)+R^2\sigma^2_{track}(\eta)+R^2\sigma^2_{ms}(\eta)} \tag{4.8}$$

or, in terms of MDR:

$$\sigma(M)=M\sqrt{\left(\gamma^2\frac{\beta c}{d}\sigma(t)\right)^2+\left(\frac{R}{MDR_{track}}\right)^2+\left(\frac{R}{MDR_{ms}}\right)^2}. \tag{4.9}$$

In order to present the mass error in terms of kinetic energy per nucleon, the velocity β, and the rigidity R have to be replaced according to the following expressions:

$$\begin{aligned}\gamma &= \frac{E_{kin}\,[GeV/nuc]}{0.931\,[GeV]}+1\\ \beta &= \sqrt{1-\frac{1}{\left(1+\frac{E_{kin}\,[GeV/nuc]}{0.931\,[GeV]}\right)^2}}\\ R &= M\cdot\beta\cdot\gamma\ [GV/c]\end{aligned} \tag{4.10}$$

where 0.931 GeV/c^2 represents the atomic mass unit and M is the particle's mass in GeV/c^2 units.

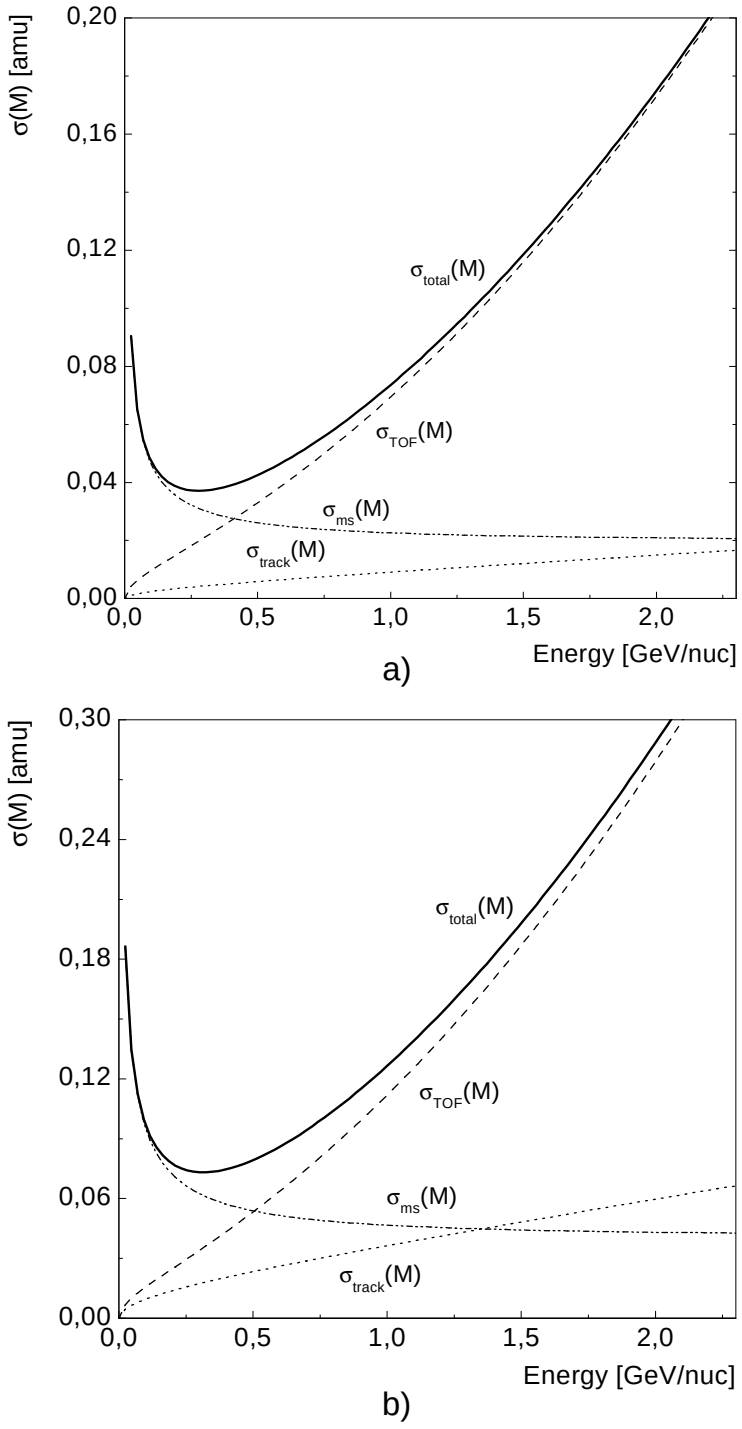

Figure 4.2: Expected a) proton and b) deuterium mass resolutions vs. kinetic energy with the IMAX instrument. Separate contributions from the tracking position resolution, multiple scattering and time-of-flight measurement are shown.

In figure 4.2 is plotted the absolute mass error, as calculated from the relation 4.9, for protons and deuterons. In both cases, the mass error in the kinetic energy interval 200÷400 MeV/nuc is expected to reach the lowest value, with the remark that for the more massive and rigid deuterium this minimum is higher than for protons. At low energies, up to 500 MeV/nuc, the mass resolution is mainly affected by the multiple scattering. With increasing energy, the determinant role in the mass measurement quality is taken by the timing error $\sigma_{TOF}(M)$. This term determines the upper energy limit for mass separation of singly charged isotopes with the IMAX instrument. Already over 2 GeV/nuc the mass error for deuterium reaches 0.3 amu, thus making very difficult a separation from protons.

One can already notice in figure 4.2 that in the low energy domain $\sigma_{ms}(\eta)$ is larger than $\sigma_{track}(\eta)$. In section 3.1.4 only the latter has been discussed, as an outcome of the fitting algorithm at high energies (relation 3.18), where multiple scattering is not anymore significant. In section 4.3 will be investigated to what extent the sigma-deflection distribution provided by the fitting procedure describes the influence of multiple scattering on the rigidity measurement at low energies.

4.2 Influence of Track Quality and Geometry Cuts on the Isotopic Ratios

As mentioned before, the basic role of cuts is to remove events where the mass measurement is less accurate, thus smearing the mass separation. Cuts improve the quality of the mass histograms mainly by removing events placed in a zone of ambiguous separation, like the region around 1.5 *amu* between protons and deuterons. If the separation becomes clear enough, usual procedures for obtaining the ratios are histogram fitting or event counting.

Cuts that could carry out these tasks are of two different sorts: requirements for a better rigidity and for a better velocity measurement. By imposing cuts on the χ^2 and $\sigma(\eta)$ or by selecting events with more hit layers employed in the fit, more accurate rigidities are selected. In addition, the agreement between the measured impact point in TOF scintillators, both from the timing information and from the tracking extrapolation (see chapter 3.2), inside a 3-σ interval of 4 *cm*, eliminates events which most probably provide an unreliable velocity measurement. Geometrical cuts are also applied by constraining tracks to pass through the active areas of each detector involved in the measurement: tracking system, time-of-flight, scintillators S1 and S2.

For the geometrical and position agreement cuts it appears no reason to question an influence on the isotopic ratio. In figure 4.3 are shown the mass histograms of events selected in this way and through a four-fold charge coincidence $Z = 1$, according to the charge cuts presented in section 3.3. In addition, further minimal conditions to select these data required only one paddle hit in the top and bottom TOF scintillators and a minimum of four position measurements in the X-coordinate and three in the Y-coordinate.

Since the number of deuterons differs with more than an order of magnitude from the protons, a logarithmic scale was used. In order to study the ratio dependence on the energy, the energy range $0.2 \div 1.8$ GeV/nuc has been split in bins of 200 MeV/nuc, calculated from the measured velocity.

As one can notice in figure 4.3, the geometry and position agreement cuts are not tight enough to achieve the needed degree of separation that would allow a gaussian fit or even an event counting. The shapes are strongly non-gaussian and moreover, due to the extreme abundance of protons there is a significant ambiguity for the masses around 1.5 *amu*. The resolution is indeed worsening with increasing energy, such that for the last bin it seems very difficult to distinguish between isotopes.

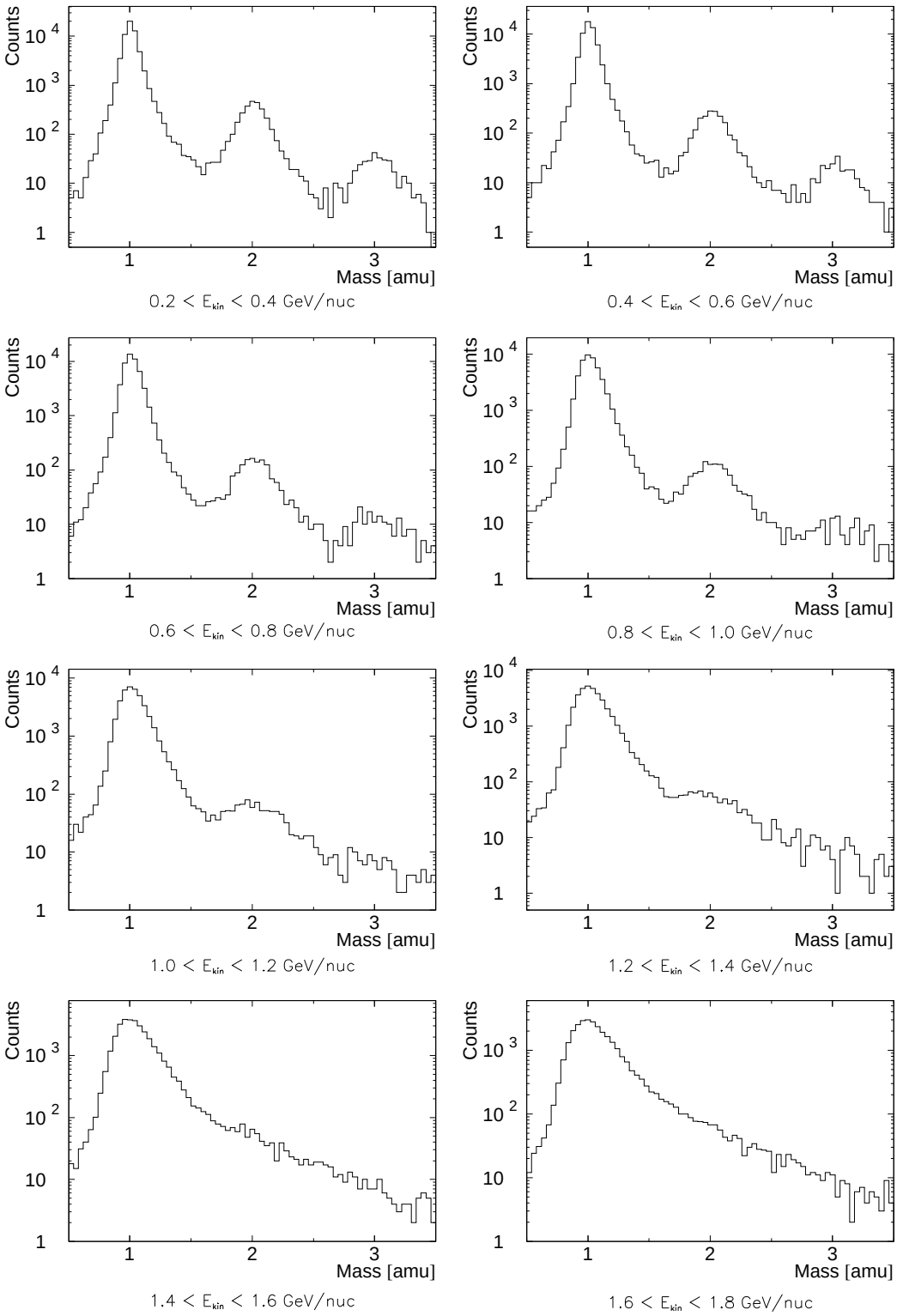

Figure 4.3: Singly charged mass histograms obtained with geometrical and position agreement cuts.

The role of the quality cuts would be to improve the mass histograms. The quantities that are suitable to be used for the selection are the following:

N_x, N_y	Number of hit layers in the tracking system (x and y readout)
χ^2_x, χ^2_y	The χ^2 of a track, calculated according to the relation 3.11 and normalized
$\sigma(\eta)$	The deflection error provided by the fitting procedure (relation 3.18)

The drawback in applying cuts is that the isotopic ratio could be affected. Since in this work only the singly charge isotopes are discussed, one has to investigate to what extent the applied cuts remove systematically more protons than deuterons, for example, or viceversa.

A way to investigate this effect is to build for each mass histogram bin in a given energy domain the following ratio: number of events after applying a specific cut divided by the number of events prior to the cut. The quantities obtained in this way can be called surviving fraction or surviving ratio histograms. If a cut has no influence on the data then the bins of the surviving ratio histograms have the value 1 or if the cut has no influence over the ratio they remain constant over all measured masses. The following cuts were investigated with this method:

$\chi^2_x < 25$	$\chi^2_y < 25$	$N_x > 6$	$N_y > 4$	$\sigma(\eta) < 0.05$
$\chi^2_x < 8$	$\chi^2_y < 8$	$N_x > 12$	$N_y > 6$	$\sigma(\eta) < 0.04$
$\chi^2_x < 4$	$\chi^2_y < 4$	$N_x > 15$	$N_y > 8$	$\sigma(\eta) < 0.02$
$\chi^2_x < 1$	$\chi^2_y < 1$	$N_x > 17$	$N_y > 10$	$\sigma(\eta) < 0.01$

Table 4.2: Set of investigated track quality cuts

By observing the shapes of the surviving fraction histograms presented in figures 4.4 to 4.8, two general features can be noticed. The first feature is that at low energies the effect of the track quality cuts is mainly noticeable for the less accurate and less numerous events with masses between the peaks. The reason is that a cut in this energy domain, where the mass resolution is determined mainly by the rigidity error, will affect especially the events with a poorer measured rigidity. These events clearly exhibit a poorer measured mass, therefore the cut removes mainly the events situated far from the correct masses, as the regions around 0.5, 1.5 or 2.5 *amu*. It can be also observed that a better separation can be achieved for harder cuts.

It was proven that a quantitative criterium to evaluate this effect was difficult to be found but nevertheless on the basis of the experience gained in the previous works [75, 33, 41] one can conclude that equal heights, widths and areas of the histogram peaks indicate an unchanged abundance ratio. Based on those qualitatively criteria, it can be easily observed that the track quality cuts at low

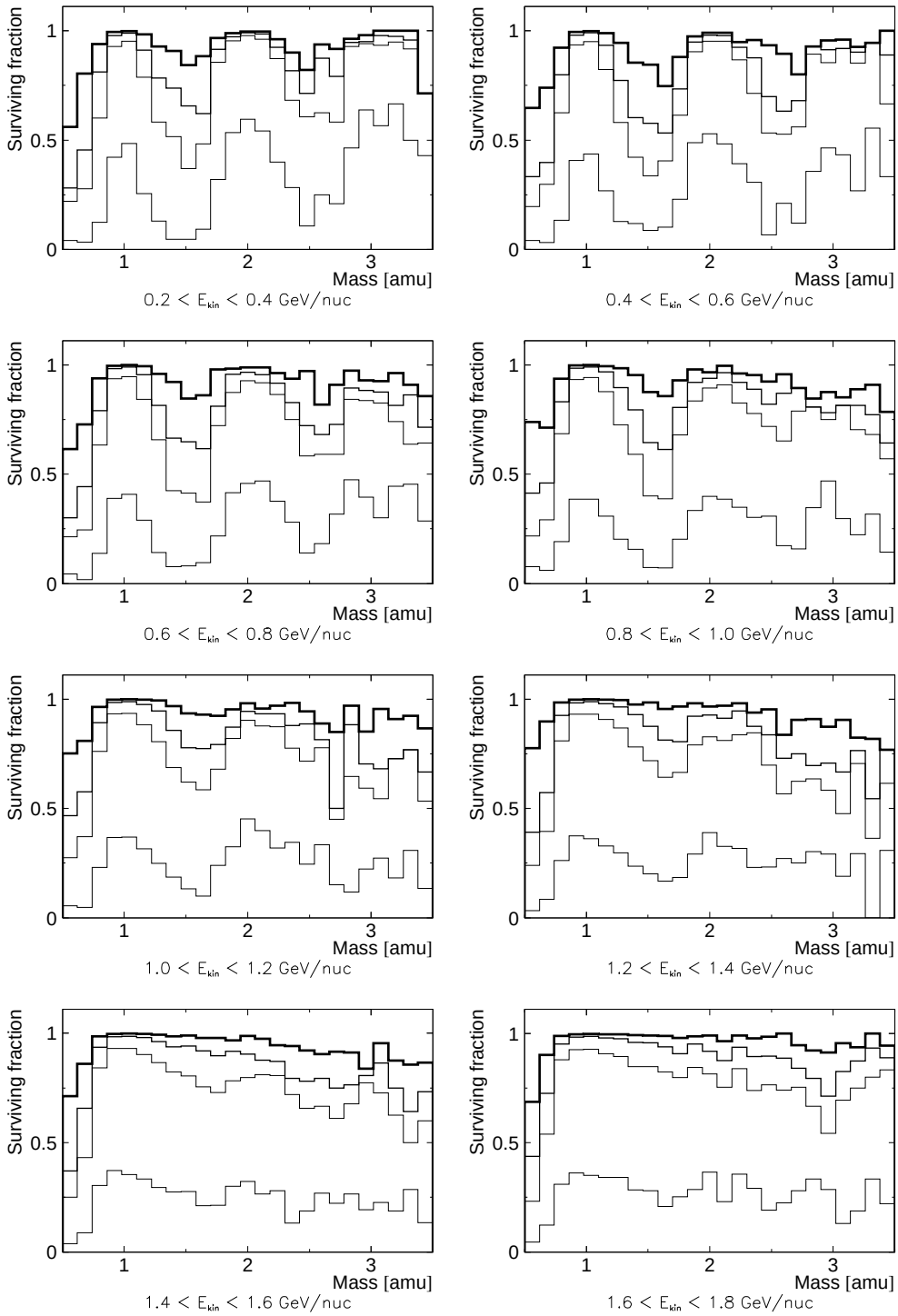

Figure 4.4: Surviving fraction histograms obtained with χ^2_x cuts (thickest line corresponds to the biggest value in table 4.2).

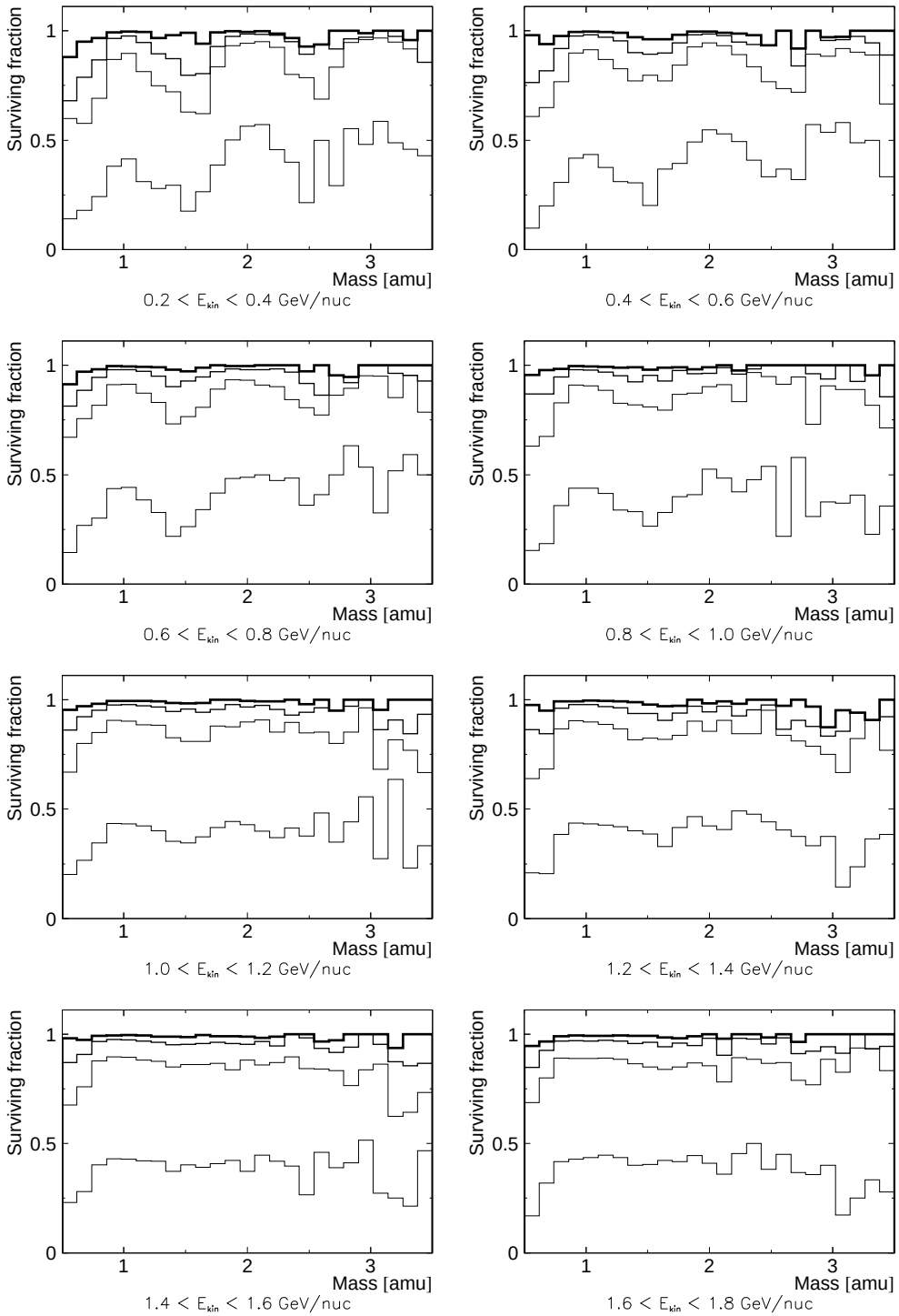

Figure 4.5: Surviving fraction histograms obtained with χ^2_y cuts (thickest line corresponds to the biggest value in table 4.2).

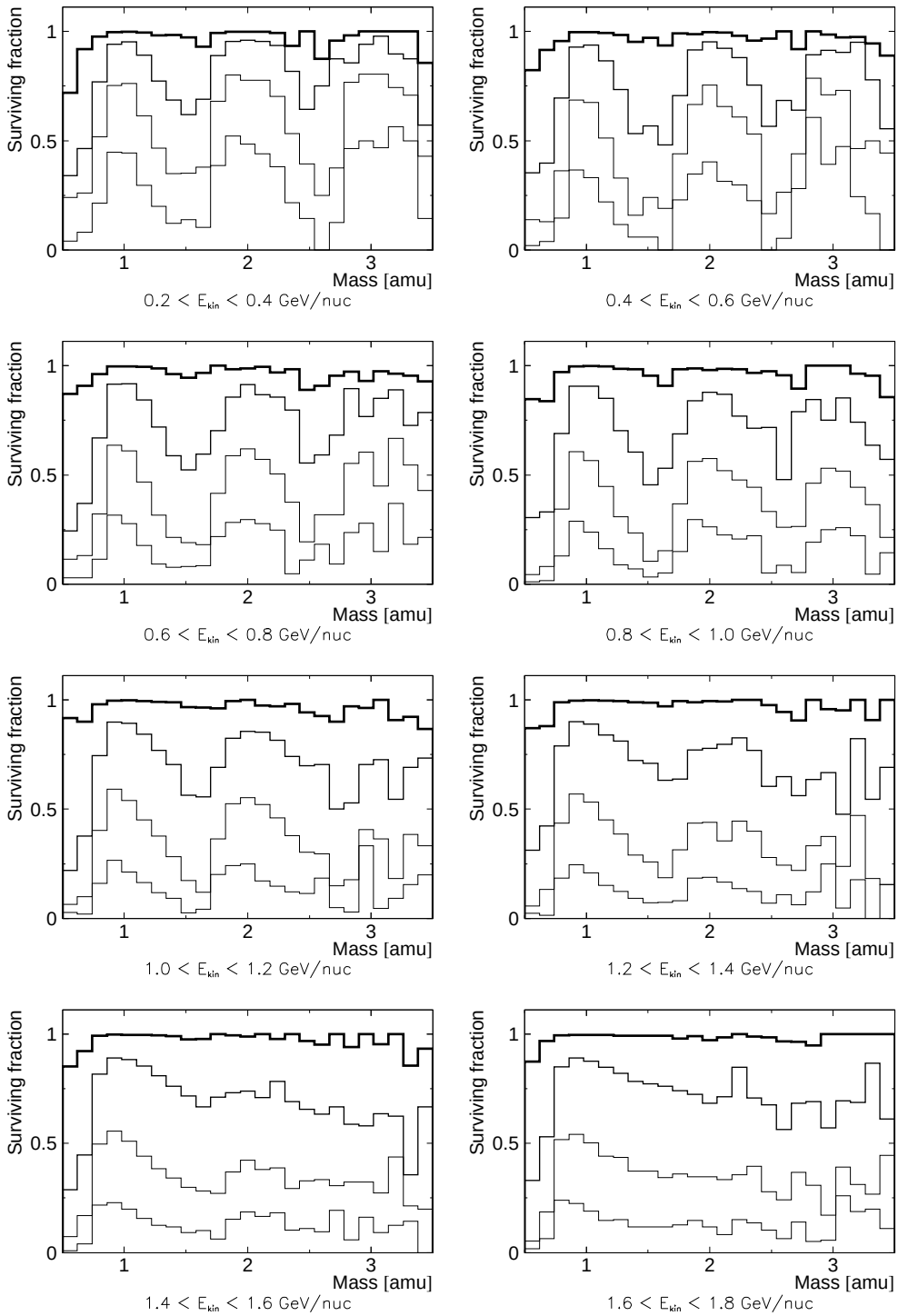

Figure 4.6: Surviving fraction histograms obtained with N_x cuts (thickest line corresponds to the smallest value in table 4.2).

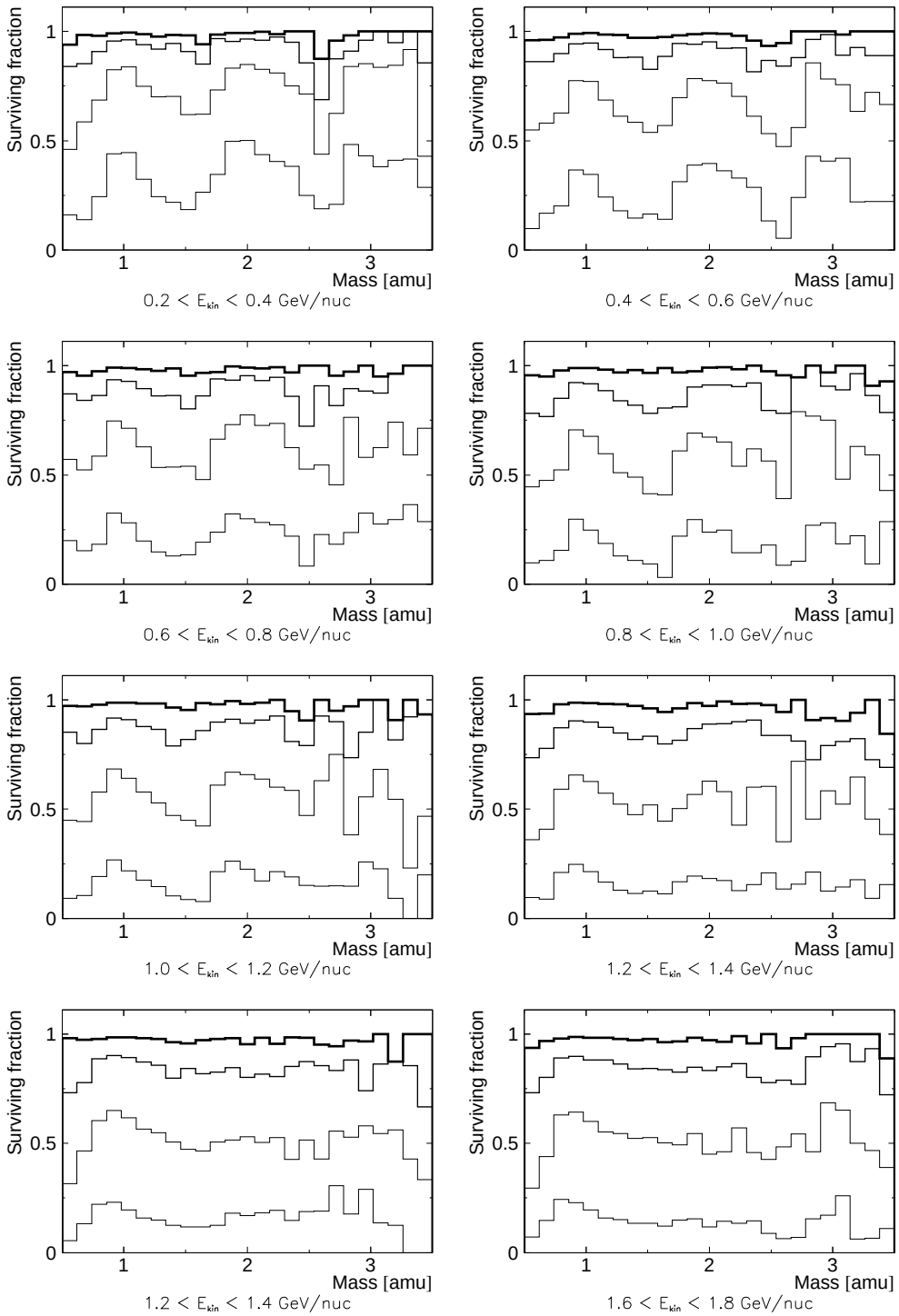

Figure 4.7: Surviving fraction histograms obtained with N_y cuts (thickest line corresponds to the smallest value in table 4.2).

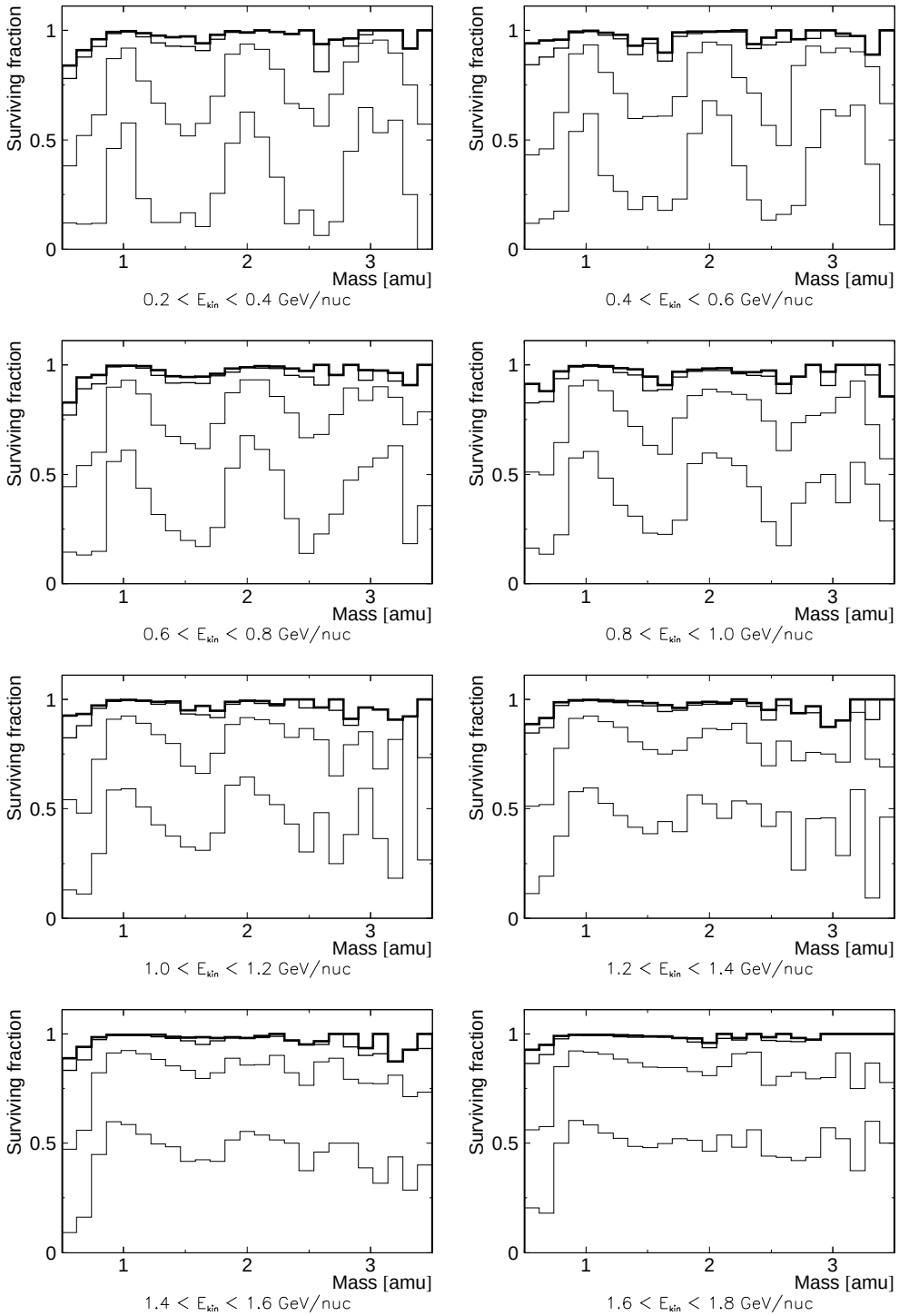

Figure 4.8: Surviving fraction histograms obtained with $\sigma(\eta)$ cuts (thickest line corresponds to the biggest value in table 4.2).

energies have the tendency to affect mainly the protons. The proton peaks tend to be lower and narrower than the deuteron or the triton ones as the hardness of the cut is increased. This effect is attributed to multiple scattering, since it can be seen from the relation 4.7 that at the same kinetic energy per nucleon the protons are more affected by this process. In principle, any track quality cut performed at low energy will bias towards higher values the deuteron-to-proton and triton-to-proton ratios, by removing especially the lighter isotopes and this effect increases with the hardness of the cut.

In the high energy domain, according to relation 4.9, the mass resolution starts to be dominated by the velocity error and therefore a track quality cut does not have an important impact on the shape of the mass histograms. Indeed, one can observe in figures 4.4 to 4.8 a flattening of the surviving fraction histograms and additionally a decreasing tendency for deuterium and tritium fractions with respect to protons. This might lead to the conclusion that the heavier isotopes are preferentially removed with respect to protons. However, it is possible that this effect is caused by the significant difference in abundance between protons and deuterons.

Previous measurements indicate that deuterons are less than 5% of the proton flux [87]. Based on this significant difference in abundance, there will be an increasing number of protons contaminating the deuterium peak with increasing energy, since the mass resolution is worsening, until the the deuterium peak is completely incorporated in the proton tail. The deuterium and tritium peaks of the surviving fraction histograms 4.4 to 4.8 are therefore lower than the proton one because the cut rejects besides deuterons and tritons also this non-negligible fraction of contaminating protons. This is consistent with the assumption that at high energy a track quality cut does not affect the isotopic ratio. Since in this energy domain a track quality cut will not bring a significant improvement of the mass histograms, it turns out to be safer to avoid using hard cuts.

From these consideration, it was decided to do not apply any further track quality cuts, except for the minimal ones, which were mentioned at the beginning of this section. The isotopic relative abundance will be estimated by means of a simulation aiming to reproduce the observed mass histograms.

4.3 Simulation Inputs Based on the Detector Performances

Since neither gaussian fitting nor a simple counting of events can solve the ambiguity of isotope identification, a simulation represents another possible way. The idea behind such a procedure is based on an inverse Monte Carlo approach: given a desired output distribution, namely the measured mass histograms, one should find the prerequisite input parameter values. The isotopic ratios are among the inputs parameters that determine the mass histograms. By varying the ratios, different levels of agreement between data and simulation can be reached, with the best agreement being related to the correct ratio.

Apart of the isotopic ratios there are other inputs necessary to obtain simulated mass histograms, namely inputs related to the detector performances, empirically determined from the data. The performances of the IMAX instrument which are needed as inputs in such a simulation are connected to each of the three separate measurements: charge, deflection and velocity.

Let us firstly refer to the charge selection performance. In chapter 3.3 it was shown that by a four-fold coincidence the selection of singly charged particles is done up to a negligible level of contamination of particles with charge $Z = 2$. As a consequence, one can assume that in the measured mass histograms (figure 4.3), particles with charge Z different from 1 are practically non-existent. Therefore, the impact of the charge resolution on the mass measurement is negligible. By simulating events with charge $Z = 1$ it is safe to assume that at least from this point of view the real mass histograms should be reproduced.

In order to simulate measured velocities one has to know both the measurement error and the incident velocity distribution. The absolute error of the velocity has been already estimated from relation 4.3 and it depends on the timing error, which was found in chapter 3.2 to be 159 ps. The spectral shape of the incoming velocities can be chosen empirically as being the measured β-distribution of singly charged particles, presented in figure 4.9.

The simulation of the spectrometer performance is a more complicated task and the problem that arises at this point is to find out the correct sigma-deflection distribution that reproduces the mass histograms. The deflection error is not a constant with respect to the energy. As it was already shown in relation 4.4, it has two components, a contribution from the position error (tracking resolution) and another one from the multiple scattering:

$$\sigma(\eta) = \sqrt{\sigma_{track}(\eta)^2 + \sigma_{ms}(\eta)^2}. \tag{4.11}$$

Although the first term does not depend on the energy, according to 3.14 it is not a constant, and it builds the distribution presented in figure 3.10. The

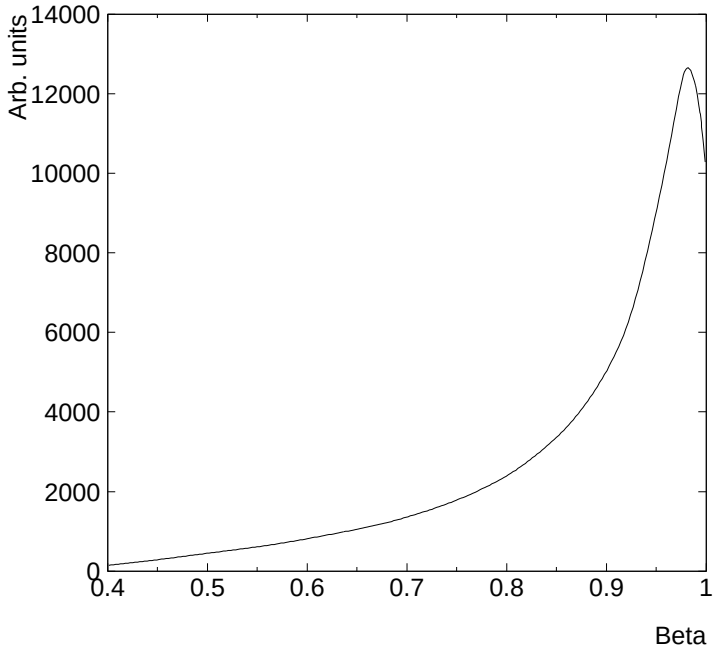

Figure 4.9: Velocity distribution of singly charged particles in the IMAX instrument, used as input of the simulation.

second term decreases with increasing energies according to relation 4.7.

Even if the fitting algorithm provides an overall deflection error, according to relation 3.18, this value cannot be used satisfactorily for a simulation unless several modifications are performed. Since the multiple scattering is not considered in the tracking algorithm, the deflection error provided by the fitting routine is underestimated for the low energies and cannot explain the observed rigidity distribution, and therefore the measured mass histograms, as it is explained further on.

The deflection error for events measured at rigidities higher than 15 GV (14 GeV/nuc for protons) is essentially caused by tracking resolution only, because the multiple scattering is not anymore significant. Thus, at these energies, the deflection error distribution provided by the fitting algorithm can be used reliably to simulate the spectrometer performance.

Let us refer now to the sigma-deflection provided by the fitting algorithm in the case of low energies. The fitting algorithm tries to interpolate the measured points as if they belong to a smooth track, namely a track of a charged particle propagating in vacuum and in the presence of a magnetic field. Since particles suffer Coulomb scattering inside the spectrometer one can not speak anymore about a smooth track, but rather about a discontinuous track. The track should

be considered smooth only between two subsequent collisions. A correct reconstruction of each segment of the track, should be associated with a new status vector that takes into account the sudden change in direction of the velocity at the point of collision. Therefore, a rigorous approach would be to integrate the equation of motion with as many status vectors as the number of multiple scattering processes. In practice this is a very difficult task, so that a common approach [32], the same adopted in this work, is to fit a single smooth track through the measured points, which actually belong to a series of discontinuous, "broken" tracks.

The outcome is that the residuals, defined in chapter 3.1.1, at low energies will build systematically wider distributions. This can be accounted for by defining an effective position resolution that gets worse at low energies [61]. One should mention at this point that the effective position resolution is worsened by the multiple scattering, while the real tracking position resolution remains energy independent. The dependency on the energy of the effective position resolution for protons, as calculated from the residual distribution obtained from the fitting procedure and averaged for medium drift paths, is illustrated in figure 4.10.

Based on the worsening position resolution with the decreasing energy, it is therefore expected for the deflection error distribution provided by the algorithm to follow this tendency. In figure 4.11 the sigma-deflection histograms provided by the fitting algorithm in the low and high energy case are presented. In order to compare the two distributions, they have been normalized to the total number of events. The sigma-deflection distribution in the case of low energies becomes indeed worse, shifting to higher values. These differences between the two histogram are nevertheless just a hint about how much would be affected the deflection error distribution provided by the algorithm, in an analogue case of highly energetic particles (negligible multiple scattering) tracked with two different position resolutions. A low energy sigma-deflection distribution like the one shown in figure 4.11 failed to reproduce the mass histograms, the simulated mass histograms achieving a mass separation of much better quality than in the measured histogram case.

A more correct sigma-deflection distribution at low energies, can be estimated according to the relation 4.4 by means of a simulation. It is actually sufficient to obtain it for a low energy bin, $200 \div 400\ MeV/nuc$ for instance, in order to see how different it is from the sigma-deflection distribution provided by the fitting algorithm.

In order to reproduce the second term of relation 4.4, protons with the kinetic energy between 200 and 400 MeV/nuc were simulated according to the velocity spectrum measured by IMAX. Combining this term with the sigma-deflection distribution at high energy, from figure 4.11, an effective sigma-deflection for low energies can be obtained (figure 4.12). The two distributions are normalized again in order to observe the differences. The differences are significant. The peak position of the simulated distribution is about 5 times higher than the one obtained

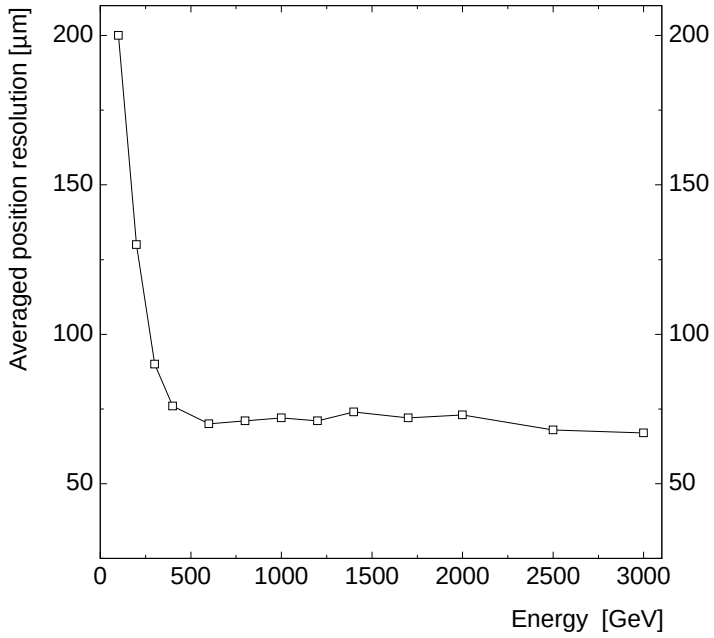

Figure 4.10: Averaged position resolution for protons as a function of energy.

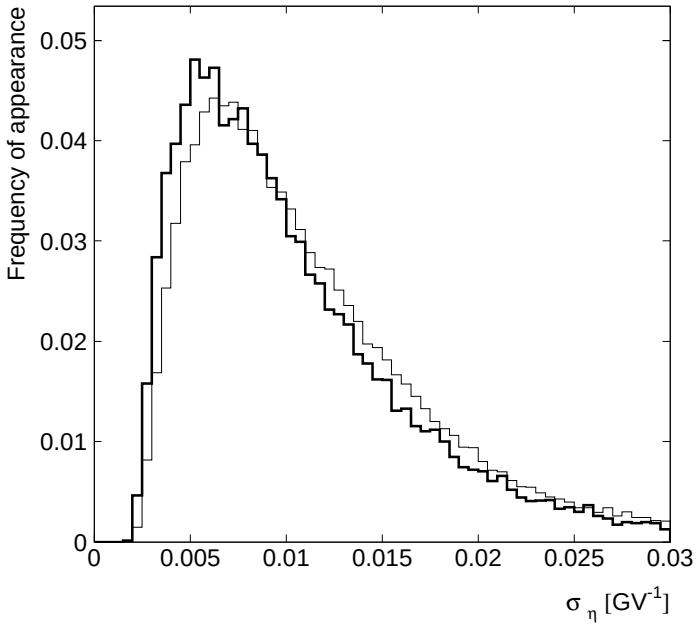

Figure 4.11: Deflection sigma-deflection distributions for energies above 14 GeV/nuc (thick line) and $0.2 \div 0.4$ GeV/nuc.

from the fitting algorithm and also the widths of the two distributions differ considerably. This figure provides a hint that the sigma-deflection calculated by the fitting routine is a significant underestimation of the real distribution and therefore, if used as input for the simulation, it would provide mass histograms of much better quality than the measured ones.

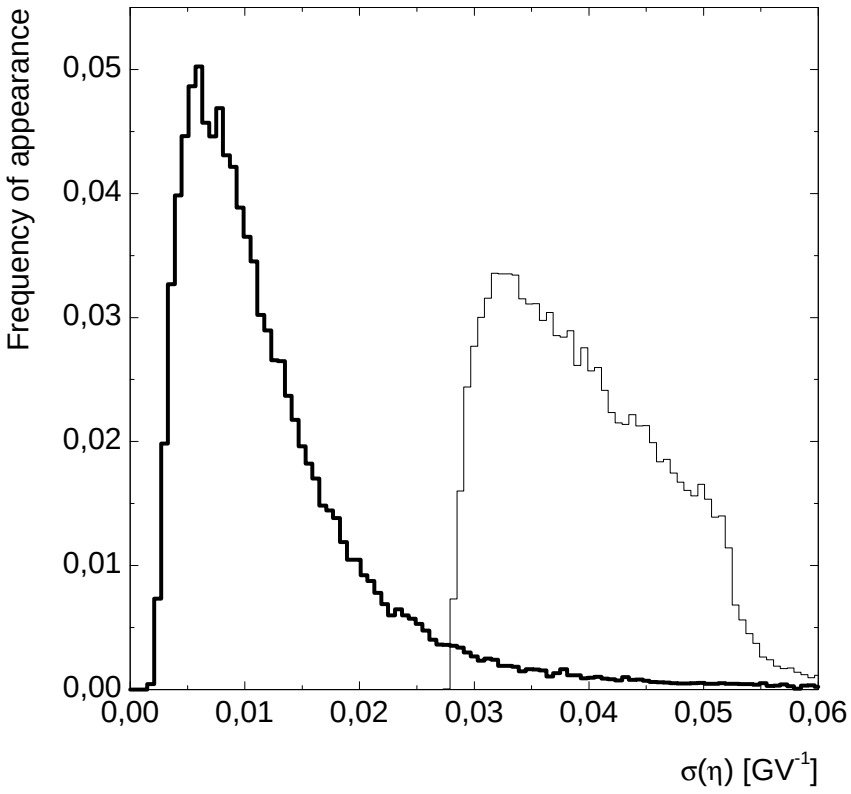

Figure 4.12: Measured (thick line) and simulated sigma-deflection distribution for energies between $200 \div 400\ MeV/nuc$.

However, it was found that even a simulation based on the simulated distribution presented in figure 4.12 was still overestimating the quality of the measured mass histograms in the low energy domains. There are at least two ways to overcome this difficulty. The first is to assume that there is a certain degree of resemblance between the correct sigma-deflection distribution and the one provided by the fitting algorithm and therefore to try to find some adjustable factors between them.

The second method, developed for this work, is to treat the events which most likely are affected by multiple scattering at large angles as belonging to a background. The mass histograms can then be reproduced by adding it to the

mass histograms obtained with a sigma-deflection distribution simulated, as in figure 4.12.

4.4 Simulations of Mass Histograms

4.4.1 Simulation Using Deterioration Factors

One way of performing the simulation is to correct the high-energy sigma-deflection histogram $\sigma_{track}(\eta)$ with an energy dependent factor, found in such a way that the mass histograms can be reproduced. In order to find a relation between the corrected (effective) sigma-deflection spectrum $\sigma_{eff}(\eta)$ and the $\sigma_{track}(\eta)$ provided by the fitting routine, one has to point again to relation 4.9, in which the contribution to the mass error due to the rigidity can be expressed by a single term:

$$\frac{1}{MDR_{eff}^2} = \frac{1}{MDR_{track}^2} + \frac{1}{MDR_{ms}^2}. \tag{4.12}$$

By multiplying this relation by MDR_{track}^2 and using the following notation:

$$\alpha = \frac{MDR_{track}}{MDR_{eff}} \tag{4.13}$$

one obtains:

$$\alpha = \sqrt{1 + \left(\frac{MDR_{track}}{MDR_{ms}}\right)^2}. \tag{4.14}$$

The quantity α, which is plotted in figure 4.13 with MDR_{track}=185 GV for singly charged isotopes, is energy dependent since it depends on MDR_{ms} and therefore decreases to the unit as the energy increases. Intuitively, for the energies between 200 and 400 MeV/nuc it is equal to the ratio between the peak positions of the two histograms presented in figure 4.12. However, as it was mentioned before, the theoretical value of α does not describe adequately the observed behavior, but this way of writing the relation between MDR_{eff} and MDR_{track} suggests that one could obtain numerically, from the data, a value for the α-factor. This factor, that could also be called deterioration factor, is energy dependent and therefore it has to be determined for each energy bin. Once it is known, the $\sigma_{eff}(\eta)$ distribution can be obtained from the relation:

$$\sigma_{eff}(\eta) = \frac{1}{MDR_{track}} \cdot \frac{MDR_{track}}{MDR_{eff}} = \sigma_{track}(\eta) \cdot \alpha. \tag{4.15}$$

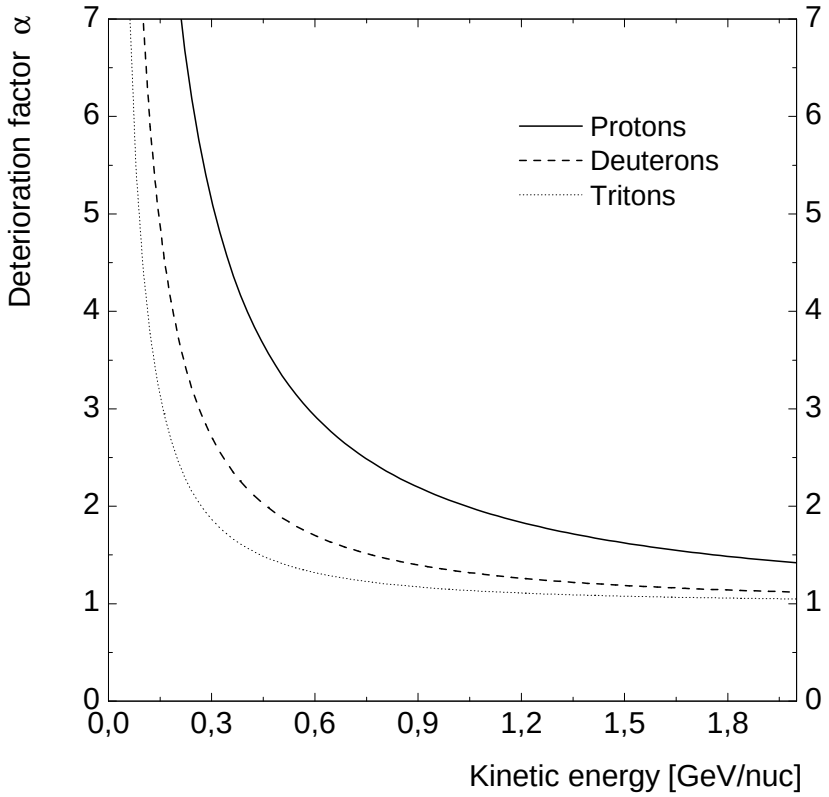

Figure 4.13: The analytical behavior of the α-factors for protons, deuterons and tritons, according to the relation 4.14.

The α-factors that describe most accurately the data can be found out by introducing them as additional variables of the simulation. Using the measured velocity spectral shape with a velocity error obtained from the time resolution $\sigma(t)$ equal to 159 ps, together with the $\sigma_{track}(\eta)$-distribution at high energies, the only parameters left are the α-factors for the three isotopes and the deuteron-to-proton and triton-to-proton ratios. This model is then able to simulate on an event-by-event basis the rigidity and the velocity values of the incoming particles that IMAX would provide in a real measurement. Using a sufficiently large number of events, smooth mass distributions can be obtained, which are then normalized to the number of events observed in the specific bin. As a criterium for the level of agreement between the measured and the simulated mass histograms the following χ^2-method was used [69]:

$$\chi^2 = \sum_{i=1}^{N_{bin}} \frac{(N_i - n_i)^2}{\sigma_i^2} \text{ with } \sigma_i = \sqrt{n_i} \tag{4.16}$$

where N_i and n_i represent the numbers of simulated and measured events in the

i-th mass bin. N_{bin} represents the number of bins of the mass histograms on which the minimization is performed.

4.4.2 D/P and T/P Ratios Determined with Deterioration Factors

In principle, the minimization can be performed simultaneously for all the five variables: α-factors for the three isotopes and the deuteron-to-proton and triton-to-proton ratio. However, because of the significant volume of calculations it has been chosen to perform an iterative process.

In the first step, the α-factors for protons are determined in each energy bin, by evaluating the minimization function only on the interval $0.6 \div 1.4$ amu and by neglecting the contamination of deuterium and tritium. With these factors estimated and by initializing the deuteron-to-proton ratio with reasonable values, the deterioration factor for deuterons can be determined. The interval on which the χ^2 is calculated will also include this time the deuterium: $0.6 \div 2.4$ amu.

This procedure is repeated alternatively for protons and deuterons and after few steps the so-determined α-factors converge to some steady values. Hence, with the α-factors being fixed, the simulation is performed again by varying the ratio. Using the deuteron-to-proton ratio determined this way, the whole procedure is repeated so that new values for the factors and the ratio are obtained. The procedure was repeated until the parameters varied only because of their statistical errors.

In order to determine the triton-to-proton ratio the same procedure was applied, but with minor differences. The ratio D/P and the α-factors determined previously, have to be used now in order to describe the contamination with deuterons in the tritium mass bins. The simulation variables in this case will be the ratio T/P and the deterioration factors for tritons. The interval of fitting has also to be changed; in this case it has to be set to $0.6 \div 1.4$ $amu \wedge 2.6 \div 3.4$ amu.

The deterioration factors determined for protons,deuterons and tritons are presented in figure 4.14. The factors follows in general the analytical behavior, but there is a systematical displacement above the curves, especially at low energies. This has been already expected, since it was mentioned in section 4.3 that a simulation based on the analytical curves only, overestimates the quality of the mass histograms at low energies.

Tritium is much less affected by multiple scattering than protons, as it is shown in figure 4.14. For energies higher than 1 GeV/nuc the deterioration curve differs from 1 with less than 10%. Therefore it should be expected that their α-factors would be almost constant and smaller than the ones for protons. However, their value as a result of the fitting procedure was bigger than expected. The reasons could be the influence of the statistical error, since the statistics in the

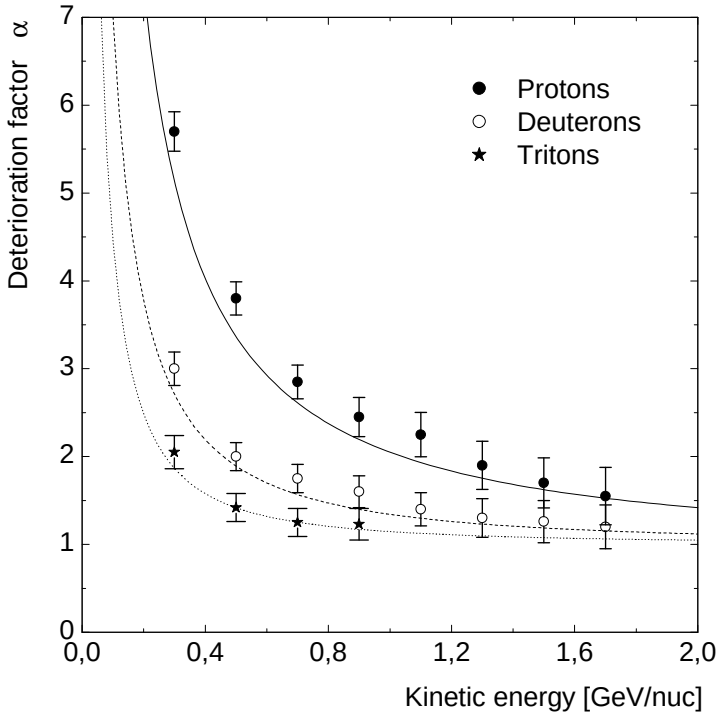

Figure 4.14: The α-factors of protons, deuterons and tritons. The curves represent the analytical behavior of the α-factors.

case of tritium is significantly smaller than the one of protons. Because of this reason, in the case of tritium, the analytical curve of the deterioration factors was used for the last four energy bins.

The level of agreement between the simulated and measured histograms can be seen in figure 4.16 while in figure 4.17 it is shown the χ^2 as a function of the D/P ratio. The other mass histograms and χ^2-minimization curves relative to the four energy bins, from 1 up to 1.8 GeV/nuc, are grouped in appendix B. The values for the D/P and T/P ratios are gathered in the table 4.3.

The error of the ratio can be determined directly from the chosen χ^2-method for minimization. In figure 4.15 the χ^2 dependency on the ratio is shown, for the energy bin $200 \div 400$ MeV/nuc. The points presented there, corresponding to a specific ratio and χ^2, are fitted with a fourth-order polynomial. The minimum of the fitted curve corresponds to the best estimate of the ratio while the interval error of $\pm 1 \cdot \sigma$, according to this method, is the ratio interval between the points of $\chi^2_{min} + 1$.

The measured mass histograms are in general reproduced by the simulation. At low energies, the agreements are particularly good for tritons and deuterons, since they are less affected by multiple scattering. The discrepancies between

Energy domain (MeV/nuc)	Ratio $\frac{D}{P} \pm \sigma$	Ratio $\frac{T}{P} \pm \sigma$
200 ÷ 400	0.0510 ± 0.0010	0.00601 ± 0.00037
400 ÷ 600	0.0353 ± 0.0012	0.00452 ± 0.00040
600 ÷ 800	0.0285 ± 0.0013	0.00399 ± 0.00035
800 ÷ 1000	0.0274 ± 0.0012	0.00346 ± 0.00036
1000 ÷ 1200	0.0231 ± 0.0014	0.00340 ± 0.00038
1200 ÷ 1400	0.0252 ± 0.0017	0.00314 ± 0.00041
1400 ÷ 1600	0.0245 ± 0.0018	0.00401 ± 0.00055
1600 ÷ 1800	0.0240 ± 0.0022	0.00553 ± 0.00080

Table 4.3: The ratios deuteron-to-proton and triton-to-proton in IMAX instrument, determined with the fitting procedure using deterioration factors.

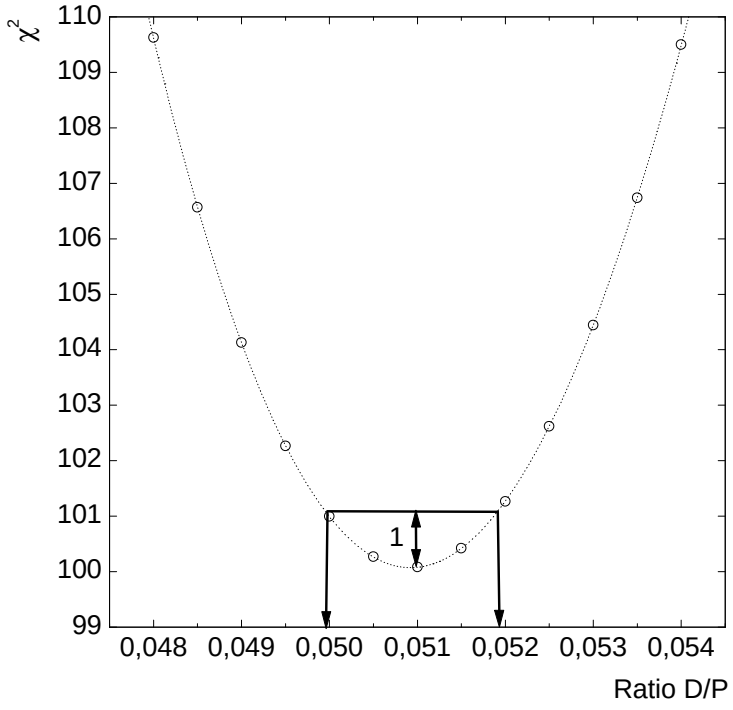

Figure 4.15: Determination of the ratio D/P and its error according the χ^2-minimization method. The obtained D/P ratio is 0.0510 ± 0.0010.

data and simulation are noticeable especially in the tails of the proton mass peaks, where the simulated histograms have systematically a slightly better resolution. One should nevertheless mention that they amount only to few percents from the proton peak. This can be explained taking into account that according to the theory of Molière about multiple scattering [9], the small scattering angles are normally distributed around the average scattering angle $\Theta = 0$ while the distribution for larger angles behaves more like Rutherford scattering, namely with more prominent tails than expected from a gaussian distribution. Therefore, the gaussian deflection error used in the simulation underestimates the frequency of appearance of larger angles, and thus underestimates the dimensions of the mass histogram tails.

If we note that the events in the tails, especially where the discrepancies are visible, make up to some percents from the whole statistics, this implies that the adopted approach allows to reproduce the observed mass histograms at the first order. The impact of the non-gaussian tails on the isotopic ratios is only a second order effect. A possible way to take into account this effect is to consider the events in the tails as background and to add it to the output of the simulation without the aid of deterioration factors, as it will be shown in section 4.4.3.

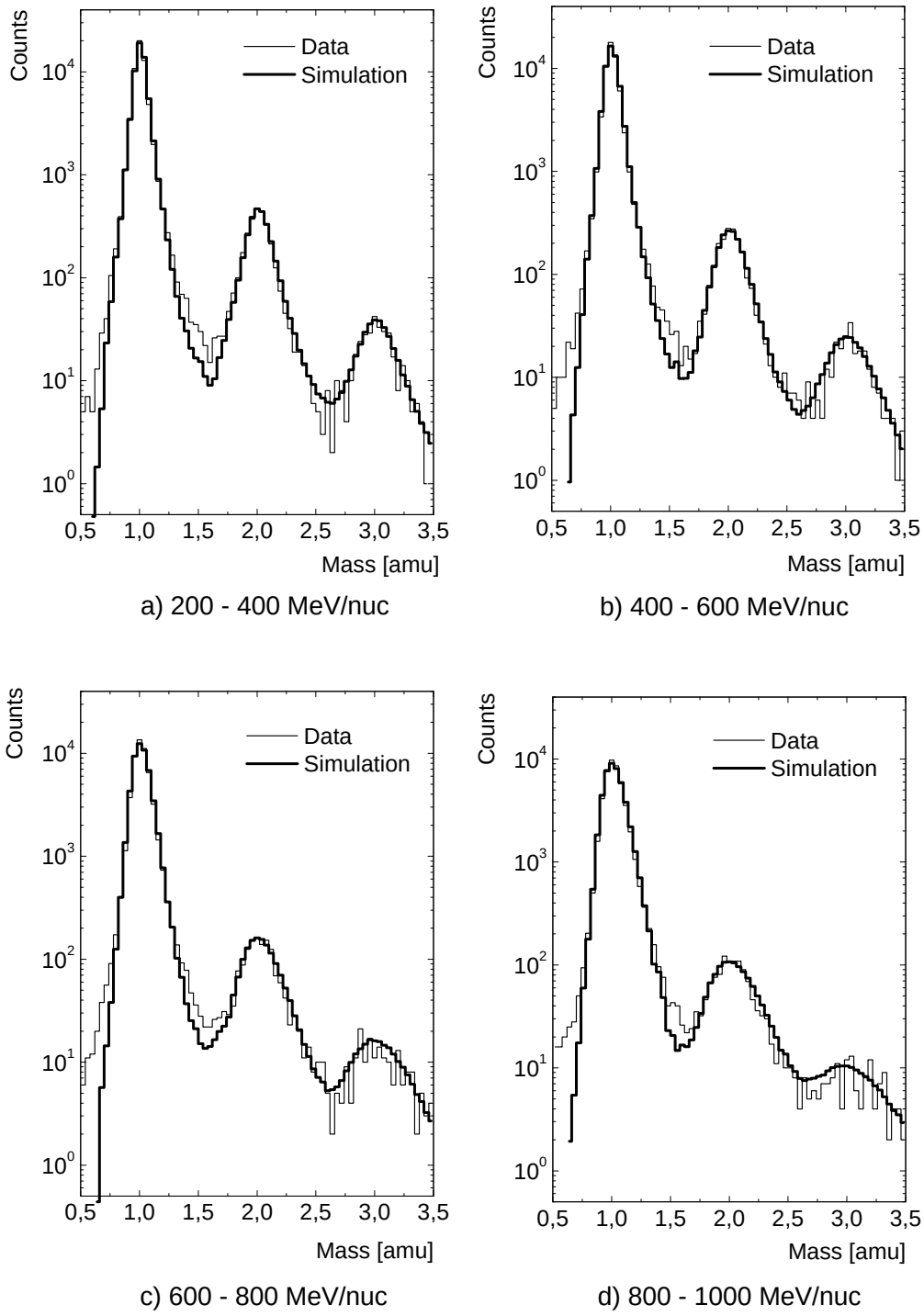

Figure 4.16: The measured and simulated mass histograms using deterioration factors for the energy range $0.2 \div 1$ GeV/nuc.

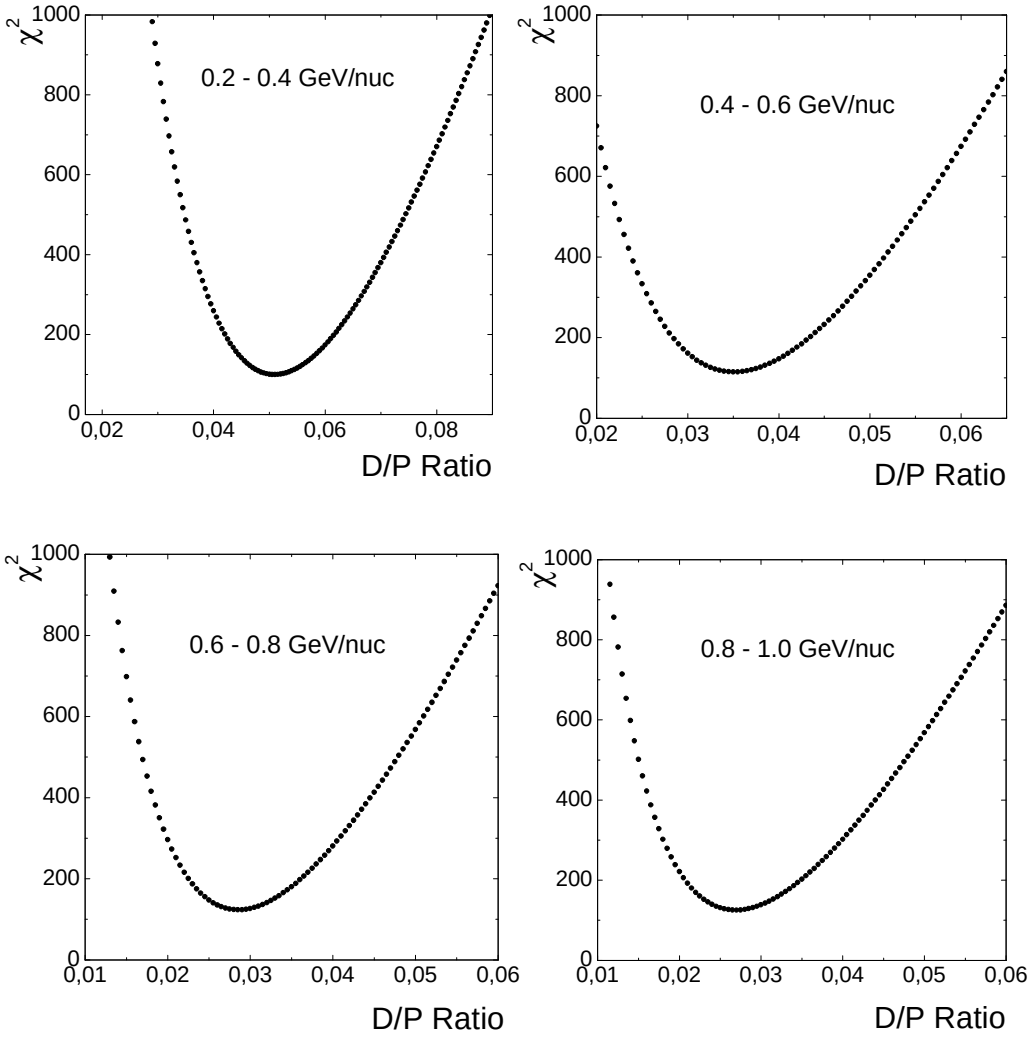

Figure 4.17: The χ^2 dependency on the ratio D/P of the simulated mass histograms for the energy range $200 \div 1000$ MeV/nuc.

4.4.3 Empirical Determination of Background Shapes

Although the simulation model based on energy dependent deterioration factors is capable to determine isotopic ratios in the instrument, there still exists a certain level of disagreement between the measured and simulated histograms, especially in the tails of the mass peaks. Apart of the low energy, where the multiple scattering with large angles are probably responsible for the disagreements, in the high energy bins of this analysis, the disagreements are also present for the left tails of the proton peak.

By looking again at figures 4.4 - 4.8 and by noticing that at high energies track quality cuts are still very effective on this particular edge of the histograms, it can be concluded that also the events with unreliably measured rigidities are again candidates for this discrepancy. As this category of events, characterized by poor track quality values, could not be reproduced with a simulation taking into account only the multiple scattering at smaller scattering angles, they could be treated as background, where the meaning of background in this context refers to events that should be avoided from being detected. From this perspective, candidates for the background are events affected by multiple scattering with large angles, nuclear scattering or δ-rays.

The separation of the background from the other events is not a distinct one, since it consists of particles that a-priori are wished to be detected, and although they underwent during the propagation some of the processes mentioned before, it was possible to fit their tracks under acceptable quality criteria, already investigated in chapter 4.2. To separate the background one has to rely on the fact that the discrepancies between the simulation and the measured histograms are located in the prominent tails (tracks which can not be properly described by the fitting procedure) and that quality cuts are effective on the tails even at higher energies, where in principle such rigidity cuts should bring little improvement to the mass histograms. Therefore, one can conclude that by performing loose quality cuts, the excluded events are dominated by background candidates.

There are two reasons why the quality cuts should be kept as loose as possible. The aim of a cut which attempts to separate the background is clearly to leave the good events unaffected as much as possible. Therefore, by studying figures 4.4 - 4.8 it comes out that a loose cut will throw preferentially events from the tails while leaving the heights of the peaks unaffected, where the good events are more probably located.

The second reason is the lower number of events that such a loose cut separates from the data set. On one hand, expression 4.5 of the deflection error is based on a gaussian approximation for the central 98% of the projected angular distribution of the multiple scattering angles. Therefore it is meaningful to assume that the background events due to multiple scattering at large angles are only few percents of the total number of events. On the other hand, at least in the case

of low energies, it is possible that the relative abundance of protons is bigger in the background because they are more affected by multiple scattering but it is difficult to make quantitative estimates about this bias. To estimate the maximum impact of this effect on the ratio one can consider that in the extreme case that all particles in the background are protons, their number should be small in comparison with the total number of particles in the data set such that the ratio is affected to a small extent.

Let us consider for example the case of deuterium. If one considers that a sample contains N_P protons and N_D deuterons and that after applying a loose cut (LC) N_p protons are removed, a simple calculation shows the impact on the original ratio $R = N_D/N_P$ of deuteron-to-proton:

$$R_{LC} = \frac{N_D}{N_P(1 - N_p/N_P)} \tag{4.17}$$

and therefore:

$$\frac{R_{LC}}{R} = \frac{1}{1 - N_p/N_P}. \tag{4.18}$$

If the relation 4.18 is expressed in relative terms one gets that:

$$\frac{R_{LC} - R}{R} = \frac{N_p/N_P}{1 - N_p/N_P}. \tag{4.19}$$

Knowing that N_D/N_P is in the range of a few percents, the ratio N_p/N_P can be approximated with $N_p/(N_P + N_D)$, where this approximation becomes more accurate as N_p decreases with respect to N_P.

However, there are limitations in decreasing the number of excluded events after a loose cut. As looser is the cut as more the background will be affected by the Poisson statistical error in the background bins.

According to these considerations, an event has been defined as belonging to the background if it does satisfy the cut $\chi^2_x \geq 8$ and at least one of other four quality factors criteria, as in the following combination :

$(\chi^2_x \geq 8 \wedge N_x \leq 12)$
$(\chi^2_x \geq 8 \wedge \sigma(\eta) \geq 0.02)$
$(\chi^2_x \geq 8 \wedge N_y \leq 6)$
$(\chi^2_x \geq 8 \wedge \chi^2_y \geq 4)$

coupled with the logical OR operation. The reason for choosing this logical combination, using especially the cut on χ^2_x, can be traced back in figures 4.4 - 4.8 where it can be observed that this cut is the most effective with respect to the background, compared with other quality factors, while leaving the peak

height relatively unchanged. A higher level of coincidence was not possible due to the statistical limitations. The statistical considerations also hinder that greater values than $\chi^2_x = 8$, namely even looser cuts, can be used. Values lower than 8 for the χ^2_x cut have proven to be less efficient in selecting the background at low energies because its shape starts to be dominated clearly by the events with a better mass measurement.

The background fractions determined with these loose cuts represent in fact an estimation of the factor N_p/N_P. They are calculated for each of the energy interval from the original data set and presented in table 4.4. The limit to which the ratio deuteron-to-proton could be biased according to the relation 4.19 is also shown in the last column, in the extreme case that the background consists of protons only.

Energy domain (MeV/nuc)	Fraction background	Maximal isotopic ratio bias
200 ÷ 400	1.69%	1.72%
400 ÷ 600	1.66%	1.69%
600 ÷ 800	1.88%	1.91%
800 ÷ 1000	2.06%	2.11%
1000 ÷ 1200	2.09%	2.14%
1200 ÷ 1200	2.19%	2.22%
1400 ÷ 1600	2.33%	2.39%
1600 ÷ 1800	2.12%	2.16%

Table 4.4: Fractions of the data set representing the background for different energy bins and maximum systematical bias introduced on the isotopic ratios.

As it can be observed, the maximum bias that this choice of the background can introduce to both deuteron-to-proton and triton-to-proton ratios is kept at a level of about 2%. Since the number of protons in the background might have been extremely underestimated and therefore they might be preferentially removed from the simulated mass peak, this bias limit is valid only for one direction. Thus, the true isotopic ratios can therefore only be systematically lower than the values estimated with the described minimization procedure. The slowly increasing background fractions with the energy is probably an effect of a slight overestimation of the effective position resolution for low energies (figure 4.10) which in turn causes slightly better values for the χ^2.

Since the backgrounds are similarly shaped, only an example for one energy bin is presented in figure 4.18 whereas the rest of the energy bins are showed in the appendix B. For a more eloquent comparison, the background has been su-

perimposed on the original mass histogram. The shape of the background, which is of main interest here, was obtained by performing a multiquadric smoothing with Poisson statistics for the background histograms bins [4].

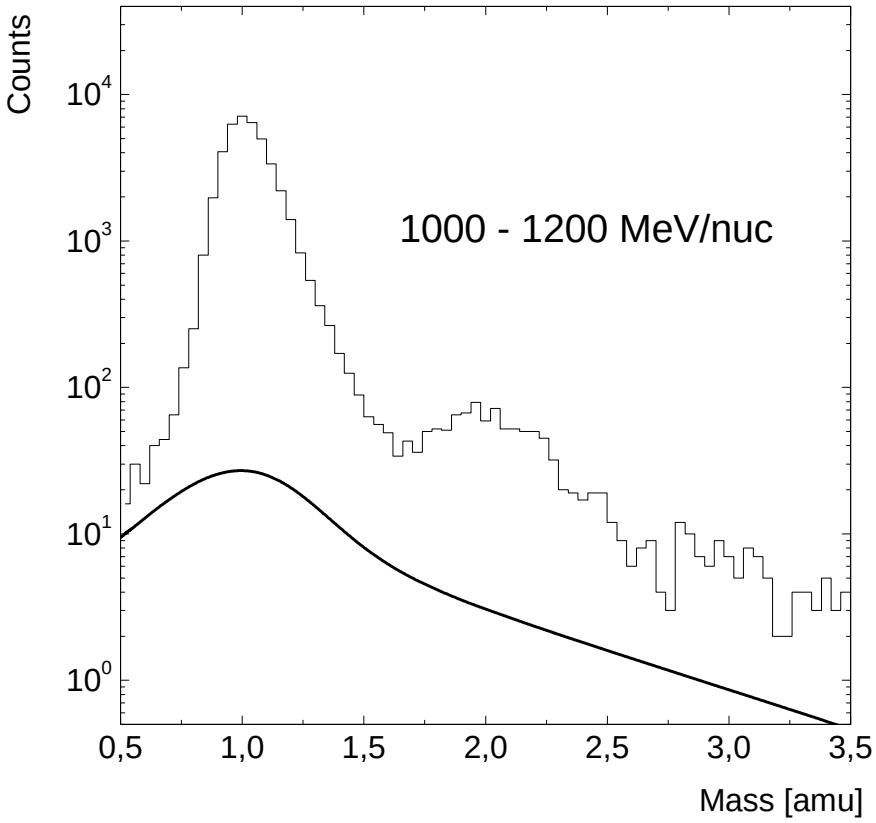

Figure 4.18: Background shape (thick line) superimposed on the measured mass distribution for the energy bin 1000 ÷ 1200 MeV/nuc.

4.4.4 D/P and T/P Ratios Determined with a Simulation Using the Background Shapes

Once the shape of the backgrounds has been empirically determined for each of the energy bins, the simulation performed in section 4.4.2 can be used again in a similar fashion. However, there are some changes to be taken into consideration since we do not deal anymore with deterioration factors. As the background shapes were determined by performing specific track quality cuts, their absolute amplitude in a certain energy bin is not determined. Therefore, before being added to the simulated mass histograms, the background has to be multiplied by an energy dependent factor, which can be found empirically by introducing it as an additional parameter in the simulation. As a consequence, the number of parameters of the simulation, for an energy bin, will be in this case three: deuteron-to-proton and triton-to-proton ratios and the background factor.

Events are simulated according to the measured velocity spectral shape with the afferent time resolution of $\sigma(t)$=159 ps. By choosing to simulate a specific kind of particles, their theoretical rigidity spectrum is consequently known together with the deflection error given by relation 4.11. The distribution of the $\sigma_{track}(\eta)$ is again the sigma-deflection distribution provided by the fitting routine at high energies, as the one in figure 4.11, while the multiple scattering contribution $\sigma_{ms}(\eta)$ is calculated according to the relation 4.7, valid only for small scattering angles. Starting with background factors at 1 and with some reasonable values for the ratios, the same iterative process was applied as in the case of deterioration factors, varying successively the parameters until steady values were reached. In the case of tritium, the particularities from the previous simulation still hold with the remark that in this case the background factors are not variable anymore, being already calculated previously in the case of deuterium.

The table 4.5 groups the results of the simulation, which are also presented graphically in figures 4.19 and 4.20. The maximum possible isotopic bias estimated in section 4.4.3 varies around a constant value of about 2%, smaller than the statistical errors presented in table 4.5. As it was expected, the differences between the ratios determined with the two simulation methods are for all energy bins between the error bars of each other. However, although the ratio does not change significantly by introducing the background shapes, the good agreement between data and simulation (figures 4.19 and 4.20) indicates that this last method provides a more accurate simulation and therefore the ratios obtained in this case are used further on in the calculations.

Energy domain (MeV/nuc)	Ratio $\frac{D}{P} \pm \sigma_{stat} - \sigma_{syst}$	Background factors
200 ÷ 400	0.0502 ± 0.0010 − 0.0009	1.41
400 ÷ 600	0.0350 ± 0.0011 − 0.0006	1.15
600 ÷ 800	0.0272 ± 0.0012 − 0.0005	1.07
800 ÷ 1000	0.0262 ± 0.0013 − 0.0005	1.32
1000 ÷ 1200	0.0232 ± 0.0014 − 0.0005	1.49
1200 ÷ 1400	0.0233 ± 0.0016 − 0.0005	1.47
1400 ÷ 1600	0.0239 ± 0.0019 − 0.0006	1.36
1600 ÷ 1800	0.0255 ± 0.0022 − 0.0006	1.29
Energy domain (MeV/nuc)	Ratio $\frac{T}{P} \pm \sigma_{stat} - \sigma_{syst}$	Background factors
200 ÷ 400	0.00578 ± 0.00038 − 0.00010	1.41
400 ÷ 600	0.00418 ± 0.00035 − 0.00007	1.15
600 ÷ 800	0.00338 ± 0.00036 − 0.00006	1.07
800 ÷ 1000	0.00279 ± 0.00036 − 0.00006	1.32
1000 ÷ 1200	0.00321 ± 0.00035 − 0.00007	1.49
1200 ÷ 1400	0.00267 ± 0.00040 − 0.00006	1.47
1400 ÷ 1600	0.00299 ± 0.00053 − 0.00007	1.36
1600 ÷ 1800	0.00481 ± 0.00074 − 0.00010	1.29

Table 4.5: The deuteron-to-proton and triton-to-proton ratios in the IMAX instrument, determined with the simulation taking the background into account. Both statistical error and the estimated systematical bias are presented.

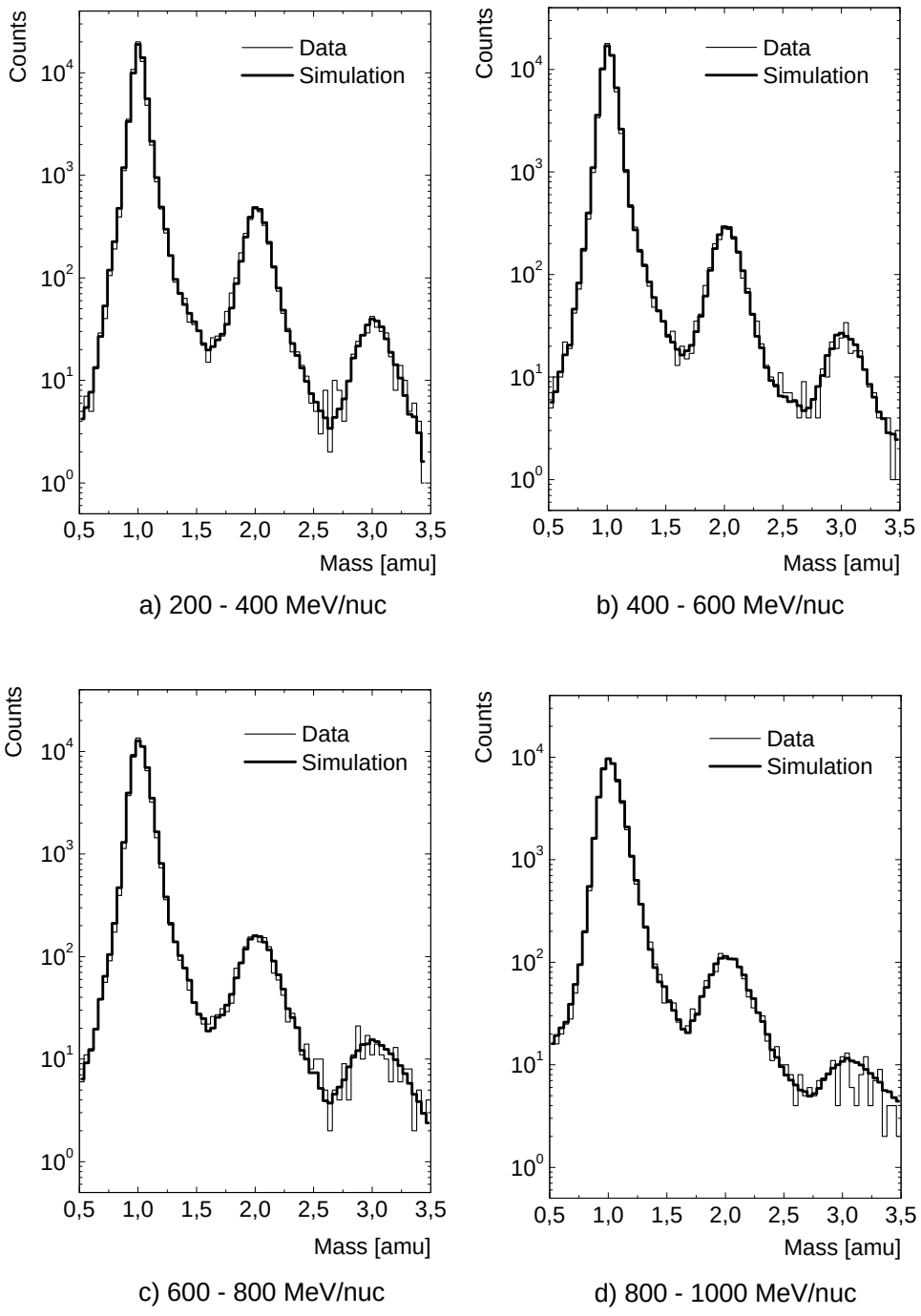

Figure 4.19: The measured and simulated mass histograms using a simulation with background for the energy range $200 \div 1000$ MeV/nuc.

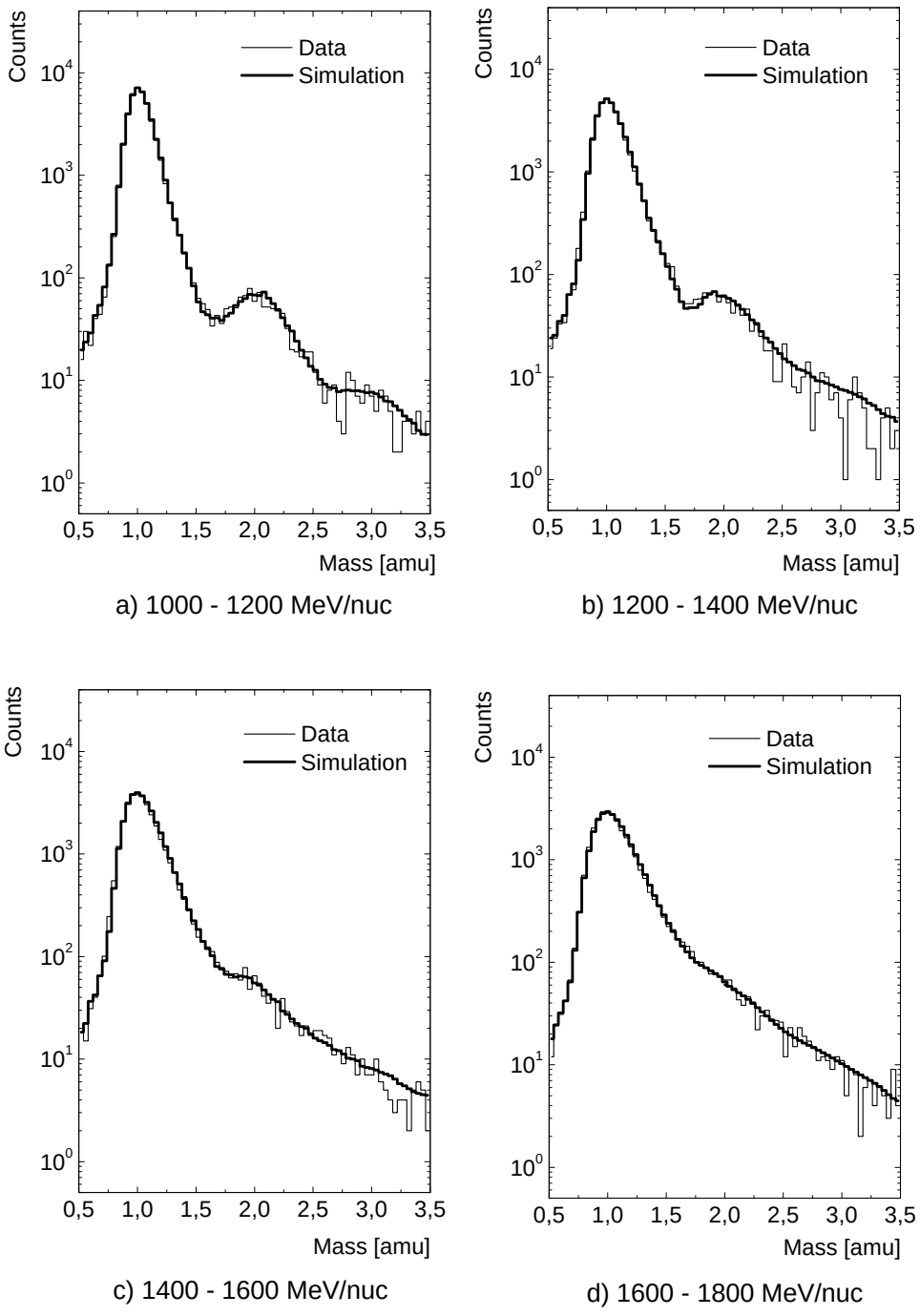

Figure 4.20: The measured and simulated mass histograms using a simulation with background for the energy range $1000 \div 1800\ MeV/nuc$.

Chapter 5

The Isotopic Ratios at the Top of the Atmosphere

This chapter provides the isotopic ratios at the top of the atmosphere (TOA), after dealing with corrections due to the interactions both with the instrument and also with the rest of the Earth atmosphere above the detector. The total flux of deuterons at the top of the instrument (TOI) is obtained by taking into account the interactions with the detector materials. To each of the isotopes three corrections will be applied: correction for the inelastic interactions, for the energy loss and for the geometrical factor. The atmospheric secondary deuteron flux at TOI will be obtained by using an appropriate calculation. The flux of primary deuterons at TOI is then determined by subtracting this secondary component from the total measured flux. The flux of primary deuterons at TOI is corrected thereafter with respect to attenuation and energy loss in the atmospheric overburden. The flux of deuterons at TOA determined this way, together with the fluxes of protons and helium already published, allow us to determine the isotopic ratios at TOA.

5.1 Instrumental Corrections

On their way from the top of the atmosphere to the place where their detection is eventually concluded, namely the bottom scintillator of the IMAX detector, the cosmic rays undergo various interactions with the matter encountered. During the propagation of the particles through the detector material the following effects have to be considered since they affect the isotopic ratio: total inelastic collisions with nuclei of the detector material, the rigidity dependence on the instrument geometrical factor and the energy loss. All those effects are energy-dependent and therefore the energetic spectral shape of the singly charged particles in the instrument have to be taken into consideration. These can be inferred from the measured energetic spectrum for all the particles with Z=1, almost entirely

dominated by protons, multiplied by the isotopic ratios obtained in the previous chapter. The three spectral shapes for protons, deuterons and tritons fluxes in the instrument are presented in figure 5.1.

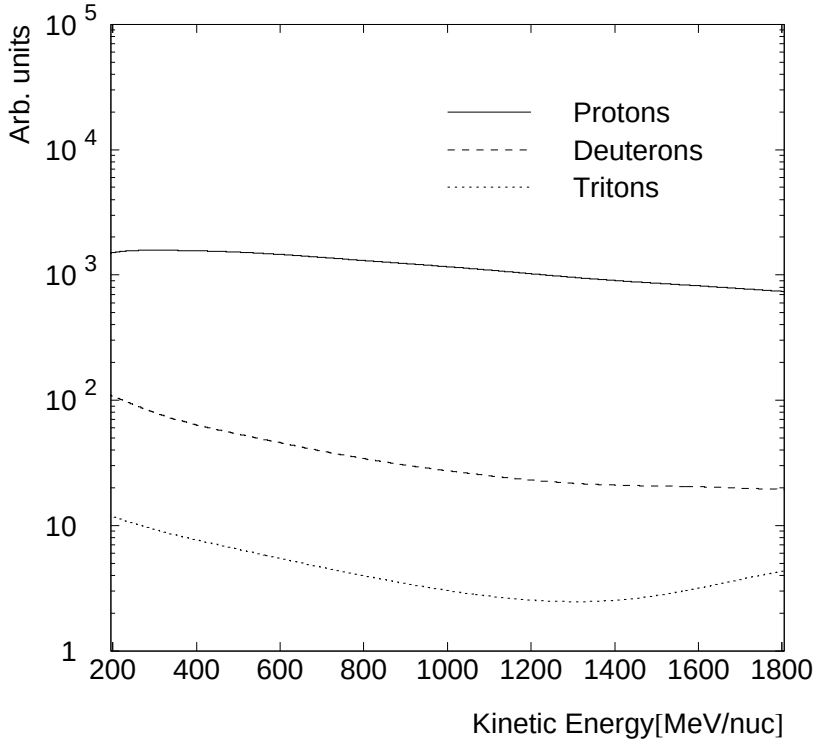

Figure 5.1: Spectral shapes of the proton, deuteron and triton fluxes measured in the instrument.

5.1.1 Corrections due to Total Inelastic Interactions in the Instrument

Once entered the instrument, the incident isotopes can be either destroyed or they can produce other sort of particles following a nuclear collision. Such events can not be properly analyzed with the present instrument, since they are characterized, among others, by different charges in different scintillators or by multiple tracks. In order to remove them, a four-fold charge selection together with geometry and position agreement cuts were applied. However, the incident singly charged nuclei have different nuclear interaction probabilities and since the isotopic ratios of interest at this point are the ones at the top of the instrument,

one has to correct the ratios measured in the instrument with factors depending on their total reaction cross-sections.

The total reaction cross-section σ_R is defined as the total σ_{tot} minus the elastic cross-section σ_{el} for two colliding ions:

$$\sigma_R = \sigma_{tot} - \sigma_{el}. \tag{5.1}$$

An analytical model that can give a reliable total reaction cross-section for the entire energy range from a few MeV/nuc to a few GeV/nuc and for light as well as for heavy systems is still a disputable topic. Most of the semi-empirical models provide an approximate total reaction cross-section in the Bradt-Peters form:

$$\sigma_R = \pi r_0^2 \left(A_P^{1/3} + A_T^{1/3} - \delta \right)^2 \tag{5.2}$$

where r_0 is a constant related to the radius of the colliding ion, δ is either a constant or an energy-dependent parameter and A_P and A_T are the projectile and target mass numbers, respectively.

The Langley Research Center (LaRC) model [48, 81, 82] proposes an universal parametrization method for the total reaction cross-section by adding new parameters that take into account several effects specific for light system collisions:

$$\sigma_R = \pi r_0^2 \left(A_P^{1/3} + A_T^{1/3} - \delta_E \right)^2 \left(1 - R_c \frac{B}{E_{cm}} \right) X_m \tag{5.3}$$

where $r_0 = 1.1\ fm$ and E_{cm} is the colliding system center of mass energy in MeV/nuc. The remaining terms in this equation are energy-dependent, varying also with the type of the colliding particles (see references).

In order to test the agreement between the measurements and the LaRC model, figures D.1 to D.5, presented in the appendix D, show a compilation of the available data on total reaction cross-sections above few MeV/nuc for the interactions involved in this work. The agreement is satisfactory if one takes also into consideration that the same model is able to reproduce the cross-section for light, medium and heavy systems over a wide energy range. On the other hand, it is widely known that the measurements, performed with different experimental techniques, show some disagreements generally attributed to systematic errors and to some inconsistencies in the definition of the total cross-section [8]. These present uncertainties in the total reaction cross section of ion collisions are an important source of inaccuracies for the results presented in this work.

The survival probability of a particle after propagating through all the layers of the different materials shown in table C.1 is given by:

$$P_{surv} = \prod_i e^{-x_i/\lambda_i} \tag{5.4}$$

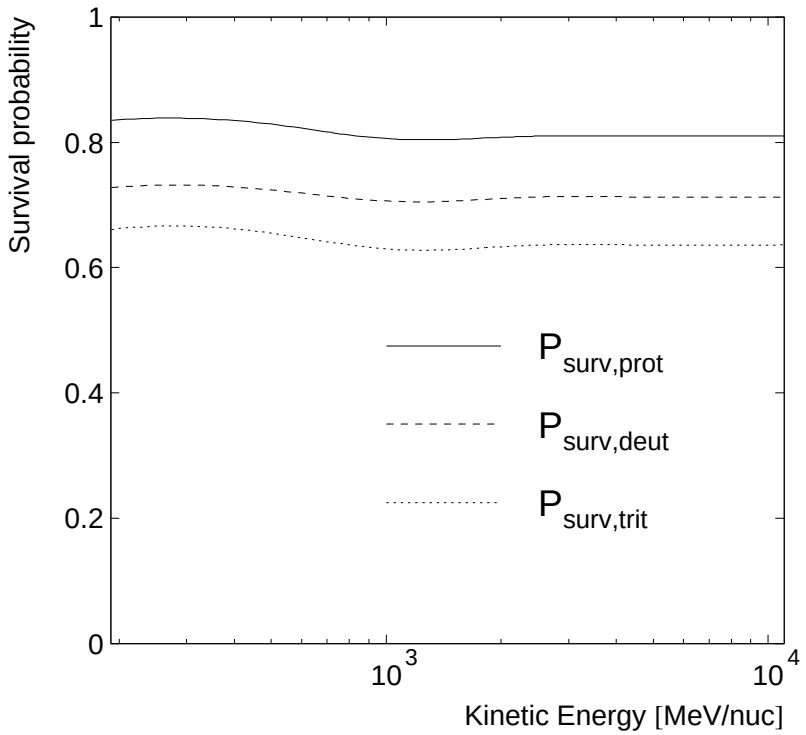

Figure 5.2: Survival probability in the IMAX instrument for protons, deuterons and tritons as a function of kinetic energy.

where x_i is the vertical path (thickness) and λ_i the mean free path in the i-th layer. The latter is defined as :

$$\lambda_i = \frac{m_i}{\sigma_i} \tag{5.5}$$

where m_i is the atomic mass of the i-th material and σ_i the total reaction cross sections of the LaRC model for the corresponding collision (see appendix D).

The survival probabilities in the instrument as a function of kinetic energy for protons, deuterons and tritons are presented in figure 5.2. The spectral shapes presented in figure 5.1 have to be divided by these probability curves in order to obtain the ratios at top of the instrument. One can immediately recognize that due to their bigger total reaction cross sections, the fluxes of deuterons and tritons are more affected during the propagation in the instrument than the protons and therefore the isotopic ratios become bigger at the top of the instrument because of this correction. The uncertainties related to the inelastic cross sections parametrization, as it can be observed in the appendix, are significant and have

been assumed to be 5 % for protons and 10 % for deuterons and tritons in order to be consistent with other similar works [87].

5.1.2 Energy Loss Correction

While propagating through the detector, the particles lose energy according to the Bethe-Bloch formula (3.29), proportionally to the squared charge-to-velocity ratio. The consequence of this dependency is that the isotopes penetrating the instrument with a given velocity, lose different amount of kinetic energy per nucleon, according to their mass. It is therefore expected that the more massive tritons will undergo less kinetic energy per nucleon losses than the lighter protons, providing that the two isotopes penetrate the top-TOF paddle with the same velocity. It follows that the spectral shapes of the isotope fluxes will be different at the top of the instrument (TOI) comparing to the ones at the middle of the instrument (MOI), affecting therefore the ratios.

In order to investigate the impact of this effect on the present analysis, a simulation of the energy loss in the instrument was performed. A set of straight track events consisting of particles of a known kinetic energy per nucleon, mass and charge was propagated through the instrument. Each of the detector materials presented in the table C.1 were divided in 1250 layers of equal path length along which the energy loss was calculated according to the formula 3.29. The correspondence between the kinetic energy at the top of the instrument and at the middle of the instrument is illustrated in figure 5.3.

From figure 5.3 it becomes clear that this effect produces a shift of the isotopic energy spectra depending on the mass but as the energy increases this displacement becomes less and less important. A proton and a deuteron whose energies were measured in the instrument as having the same value of 200 MeV/nuc, had actually different energies at the top of the instrument: 241.7 MeV/nuc and 222.3 MeV/nuc, respectively. This difference decreases with the energy, thus diminishing the impact on the ratio. The same isotopes, whose energies in the instrument are 1800 MeV/nuc, had at the top of the instrument 1821.1 MeV/nuc and 1810.2 MeV/nuc, respectively. Considering in addition the same calculations performed in section 5.2 in the case of a propagation through the atmospheric residual depth, the minimum energy that a proton must have at the top of the atmosphere to reach the bottom-TOF and trigger the instrument is 171 MeV/nuc. In the case of deuterium this energy amounts to 112 MeV/nuc and for tritium is 89 MeV/nuc.

The clearest illustration of this effect on the energetic spectral shapes is for the case of protons, as depicted in figure 5.4. The energy loss correction on the energy domain above 200 MeV/nuc causes a right-displacement of the shape but in the same time an increase of proton number in lower energetic bins. This tendency is similar for all the isotopes but the heavier deuterons and tritons are less affected

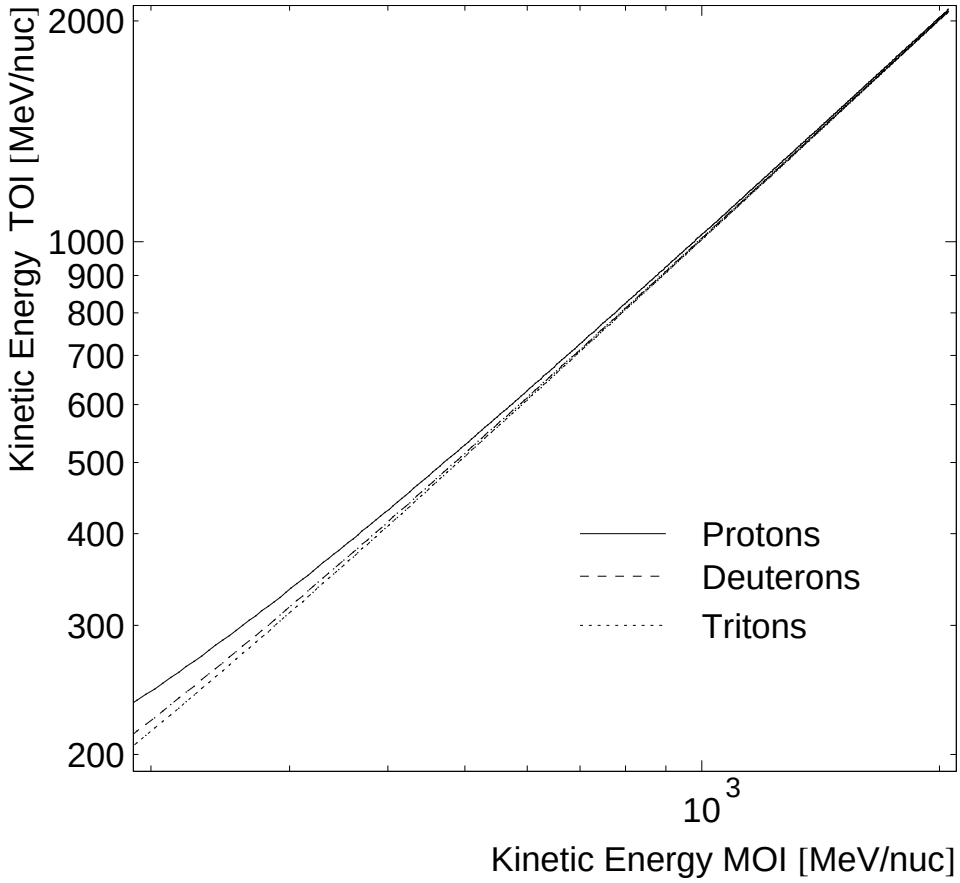

Figure 5.3: Dependence of the kinetic energy per nucleon in the middle of the instrument on the same quantity at the top of the instrument in the case of protons, deuterons and tritons.

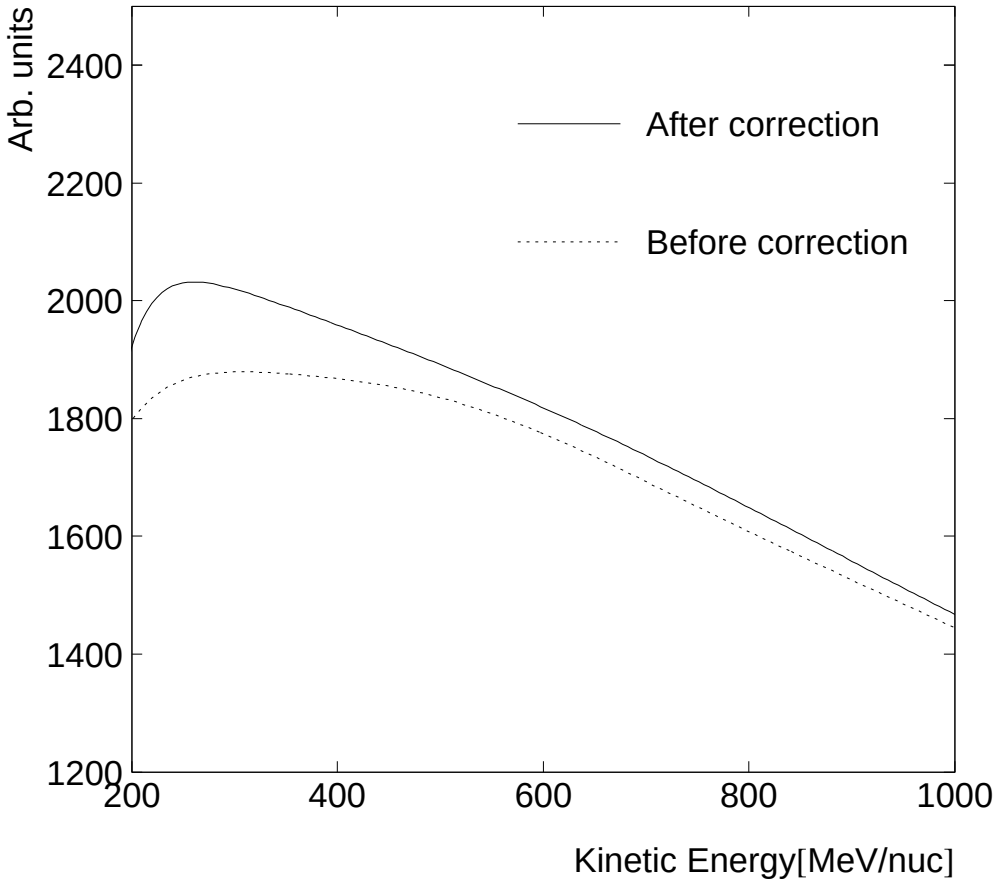

Figure 5.4: Displacement of the energetic spectral shape of protons due to the energy loss correction.

than the protons. Eventually, as the energy increases, the displacement becomes a negligible constant since the energy loss enters in the saturation regime. The former energy bins in which the ratios were obtained until this point will shift accordingly to bigger values, as it will be shown further on.

5.1.3 Geometrical Factor of the Experiment

The geometrical factor of the experiment is another correction factor that has to be taken into account for obtaining the isotopic ratio above the instrument. In the case of a particle telescope, as the IMAX detector, the geometrical factor is defined as the ratio between the measured counting rate and the isotropic flux intensity, as in the following relation:

$$GF = \frac{N}{F} = \int\int\int dA \cos\theta \sin\theta d\theta d\varphi \tag{5.6}$$

where N is the detected count rate, F is the incident flux, dA is an infinitesimal area element, θ is the polar angle of incident particles and φ the azimuthal angle. The integration is performed over the active area of the top-TOF surface and the solid angle subtended by it.

Due to the presence of the magnetic field, which bends the particle track, the geometrical factor is in general rigidity dependent but approaches a constant value for increasing rigidities, where the tracks are essentially straight. In order to calculate the rigidity dependence of the geometrical factor, a Monte Carlo simulation has been performed [62]. Its principle is to simulate N_1 events, namely particles penetrating the top-TOF active layer at a given rigidity and to calculate their tracks through the detector since the magnetic field configuration is known. The tracks that do not reach the bottom-TOF layer are removed from the data set. To assure that the simulated flux is isotropic, the polar angle is varied between 0 and $\pi/2$ and the azimuthal angle between 0 and 2π. Summing up all N_2 accepted events, the geometrical factor becomes:

$$GF(R) = \pi A \cdot \frac{N_2(R)}{N_1} \tag{5.7}$$

where A is the active surface of the top-TOF and R represents the rigidity.

The figure 5.5 shows the variation of the geometrical factor as a function of rigidity. For the purposes of the present analysis it is also useful a representation of the geometrical factor as a function of kinetic energy, where the differences for the three isotopes are easily observable (figure 5.5). Because of the stronger bending of the protons in the magnetic field at a given energy, the geometrical factor of the instrument with respect to them is lower than in the case of the other two isotopes. Therefore, to account for the geometrical factor effect that increase the number of particles at the top of the instrument as the isotopic mass decreases, each of the spectral shapes has to be divided by the corresponding energy-dependent geometrical factor.

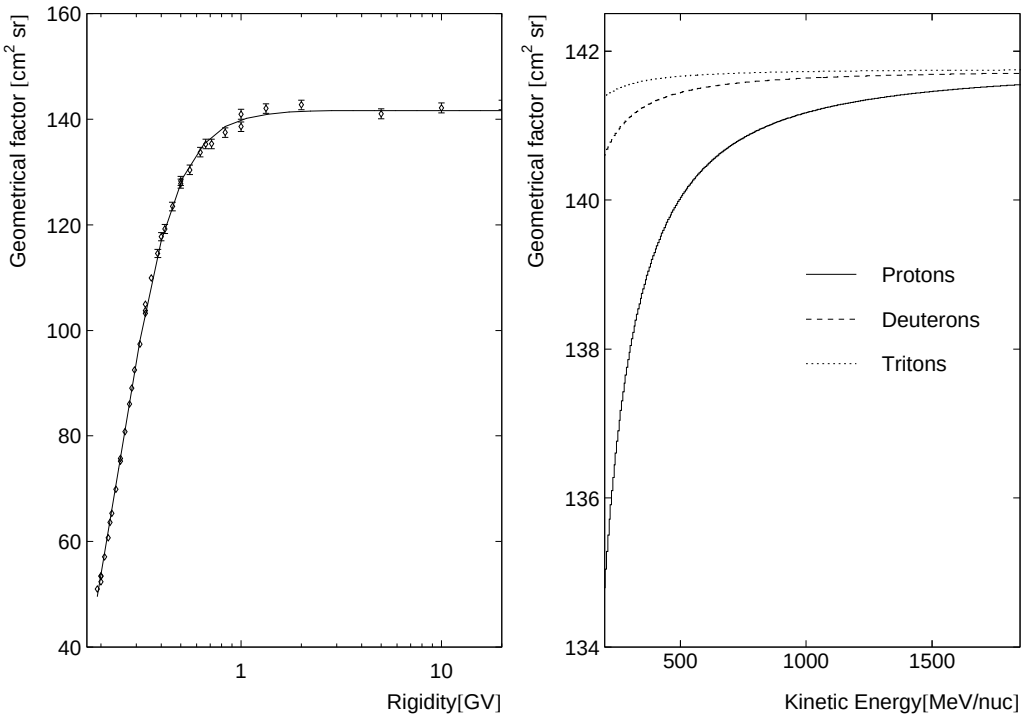

Figure 5.5: Geometrical factor of the IMAX experiment as a function of the rigidity and kinetic energy.

5.1.4 The Isotopic Ratios at the Top of the Instrument

The isotopic ratios at the top of the instrument after performing all three corrections described before are presented in the table 5.1. They are obtained by an integration of the shifted and corrected spectra in the new energetic bins and thereafter by dividing the results.

By comparing the corrected ratios with the ones in the instrument it can be observed a systematical increase for all the energy bins. The correction with respect to the inelastic collisions in the instrument alone amounts at approximately 15% and therefore has the biggest impact on the increase of the ratio. The energy loss correction have a similar impact due to the differences in the spectral shapes of the protons on one side and the other two isotopes on the other side, but because of the spectral shifting, the overall influence on the ratio is essentially negligible. The geometrical factor correction decreases the ratios at the top of the instrument since the lighter protons are strongly deflected by the presence of the magnetic field. However, the strength of this correction hardly amounts to few percents and it decreases abruptly as the energy increases.

Energy domain TOI (MeV/nuc)	Ratio $\frac{D}{P} \pm \sigma_{stat} \pm \sigma'_{syst} - \sigma_{syst}$
241.7 ÷ 430.5	0.0541 ± 0.0011 ± 0.0061 − 0.0009
430.5 ÷ 625.6	0.0391 ± 0.0010 ± 0.0044 − 0.0006
625.6 ÷ 824.7	0.0318 ± 0.0012 ± 0.0036 − 0.0005
824.7 ÷ 1022.1	0.0277 ± 0.0013 ± 0.0031 − 0.0005
1022.1 ÷ 1221.8	0.0258 ± 0.0014 ± 0.0029 − 0.0005
1221.8 ÷ 1421.5	0.0256 ± 0.0016 ± 0.0029 − 0.0005
1421.5 ÷ 1621.3	0.0273 ± 0.0019 ± 0.0030 − 0.0006
1621.3 ÷ 1821.1	0.0290 ± 0.0022 ± 0.0032 − 0.0006
Energy domain TOI (MeV/nuc)	Ratio $\frac{T}{P} \pm \sigma_{stat} \pm \sigma'_{syst} - \sigma_{syst}$
241.7 ÷ 430.5	0.00675 ± 0.00038 ± 0.00076 − 0.00010
430.5 ÷ 625.6	0.00515 ± 0.00035 ± 0.00058 − 0.00007
625.6 ÷ 824.7	0.00413 ± 0.00036 ± 0.00046 − 0.00006
824.7 ÷ 1022.1	0.00349 ± 0.00036 ± 0.00039 − 0.00006
1022.1 ÷ 1221.8	0.00317 ± 0.00035 ± 0.00035 − 0.00007
1221.8 ÷ 1421.5	0.00329 ± 0.00040 ± 0.00037 − 0.00006
1421.5 ÷ 1621.3	0.00382 ± 0.00053 ± 0.00047 − 0.00007
1621.3 ÷ 1821.1	0.00623 ± 0.00074 ± 0.00070 − 0.00010

Table 5.1: The deuteron-to-proton and triton-to-proton ratios at the top of the IMAX instrument. The notation for the errors is the same as in table 4.5, with σ'_{syst} including the errors from the instrumental corrections.

5.2 Atmospheric Corrections

The deuteron-to-proton ratio at the altitude where the IMAX instrument performs the measurement is not equal to the ratio in cosmic rays before reaching the Earth atmosphere. The nuclei incident on $\sim 5\ g{\cdot}cm^{-2}$ of atmospheric overburden are subject to various interactions with the air nuclei, which modify the initial isotopic composition. The flux of the secondary deuterons at TOI is obtained by applying an appropriate propagation calculation of the incident cosmic nuclei at the TOA. Multiplying the measured deuteron-to-proton ratio at TOI by the total flux of protons at TOI previously determined with IMAX [62], the total flux of deuterons can be obtained. Thereafter, the flux of cosmic ray deuterons at TOI can be obtained by subtracting from this flux the atmospheric deuterons. In addition, similar attenuation and energy loss corrections as in the instrumental case have to be performed on the flux of cosmic ray deuterons in order to obtain it at TOA. The ratio D/He and D/P can be then easily inferred by dividing the flux of deuterons determined this way by the fluxes of protons and helium already measured [62].

5.2.1 The Atmospheric Secondary Deuterons

The corrections for the inelastic interactions in the atmosphere are complex because they imply a substantial yield of isotopes from interactions between all cosmic ray primaries and the air nuclei. Therefore, a full correction to the spectra of protons and deuterons require a comprehensive atmospheric propagation calculation which includes the various projectiles, different reaction channels and the appropriate inclusive production cross-section for the secondaries.

For determining the flux of the secondary protons and deuterons at the top of the instrument the calculations developed by Vannuccini, Papini, Grimani and Stephens [70, 83, 84] have been chosen. The following processes have been taken into account for the production of the secondary protons: spallation of cosmic-ray helium and heavier nuclei, slowing down of primary protons resulting from inelastic interactions, recoil nucleons, and evaporation of air nuclei. In the case of the atmospheric deuterium three categories of processes have been considered: production from the air target nuclei, production from incident nucleons through the reaction $\mathrm{P} + \mathrm{P} \rightarrow \mathrm{D} + \pi$ and fragmentation of the incident nuclei.

The inputs needed for such calculations are the primary spectra of the cosmic radiation at the TOA for a solar modulation corresponding to the IMAX flight ($\Phi = 750\ MV$). The absolute fluxes of protons and helium at TOA were actually measured with the IMAX instrument [62] so they could be easily applied here. The heavy nuclei flux ($Z > 2$) at the TOA is scaled from the carbon flux, as an equivalent number of ^{12}C nuclei. Finally, the angular distribution of the

secondaries are integrated over the zenith angle up to 17°, the maximal angular acceptance of the IMAX instrument.

The calculated atmospheric contributions to protons and deuterons flux as well as the total flux of protons ($P_{tot,TOI}$) measured by IMAX at the top of the instrument are gathered in the table 5.2.

Energy domain TOI (MeV/nuc)	$P_{sec,TOI}$ $(m^2 \cdot s \cdot sr)^{-1}$	$D_{sec,TOI}$ $(m^2 \cdot s \cdot sr)^{-1}$	$P_{tot,TOI}$ $(m^2 \cdot s \cdot sr)^{-1}$
241.7 ÷ 430.5	44.04 ± 8.81	3.71 ± 0.74	187.2 ± 1.3 ± 11.7
430.5 ÷ 625.6	20.98 ± 4.20	0.98 ± 0.20	162.4 ± 1.0 ± 10.1
625.6 ÷ 824.7	11.64 ± 2.33	0.63 ± 0.13	142.3 ± 0.8 ± 9.0
824.7 ÷ 1022.1	7.38 ± 1.48	0.49 ± 0.10	121.7 ± 0.6 ± 7.5
1022.1 ÷ 1221.8	5.39 ± 1.08	0.39 ± 0.08	106.4 ± 0.5 ± 6.7
1221.8 ÷ 1421.5	4.17 ± 0.83	0.32 ± 0.06	93.4 ± 0.4 ± 5.8
1421.5 ÷ 1621.3	3.33 ± 0.67	0.26 ± 0.05	82.1 ± 0.5 ± 5.2
1621.3 ÷ 1821.1	2.71 ± 0.54	0.22 ± 0.04	72.2 ± 0.3 ± 4.4

Table 5.2: The calculated fluxes of protons and deuterons, produced and attenuated during the propagation through 5 g/cm^2 of atmospheric depth. The last column represents the total proton flux at TOI measured with IMAX [62].

Using the total flux of protons at the top of the instrument ($P_{tot,TOI}$) and the calculated atmospheric contribution to the deuterium flux ($D_{sec,TOI}$), it is now possible to obtain the primary deuterons at TOI ($D_{pri,TOI}$):

$$D_{pri,TOI} = D_{tot,TOI} - D_{sec,TOI} = (D/P)_{TOI} * P_{tot,TOI} - D_{sec,TOI} \tag{5.8}$$

where the ratio $(D/P)_{TOI}$ is the measured deuteron-to-proton ratio at the top of the instrument. The results are shown in table 5.3.

The flux of secondary deuterons amounts to almost 58% of the primary deuteron flux at TOI for the first energy bin and therefore has an important influence over the ratio D/He at TOA. This contribution then decreases steadily from about 18% in the second energy bin to almost 10% for the last one. Up to a few hundred MeV/nuc the production of deuterium is dominated by the fragmentation of air nuclei whereas for higher energies the spallation of the helium and heavier nuclei is the most important source.

Energy domain TOI (MeV/nuc)	Mean Energy (MeV/nuc)	$D_{pri,TOI} \pm \sigma_{stat} \pm \sigma'_{syst} - \sigma_{syst}$ $(m^2 \cdot s \cdot sr)^{-1}$
241.7 ÷ 430.5	329.1	6.41 ± 0.20 ± 1.50 − 0.16
430.5 ÷ 625.6	524.1	5.38 ± 0.19 ± 0.84 − 0.10
625.6 ÷ 824.7	721.2	3.90 ± 0.17 ± 0.60 − 0.07
824.7 ÷ 1022.1	921.4	2.88 ± 0.16 ± 0.44 − 0.07
1022.1 ÷ 1221.8	1121.4	2.36 ± 0.15 ± 0.36 − 0.05
1221.8 ÷ 1421.5	1321.3	2.08 ± 0.15 ± 0.31 − 0.05
1421.5 ÷ 1621.3	1521.0	1.98 ± 0.16 ± 0.29 − 0.05
1621.3 ÷ 1821.1	1721.8	1.88 ± 0.16 ± 0.27 − 0.04

Table 5.3: The flux of cosmic ray deuterons at the top of the instrument. The error σ'_{syst} also includes the errors on the proton flux at TOI and on the atmospheric deuteron correction.

5.2.2 Attenuation and Energy Loss Correction

The flux of primary deuterons at TOI has to be also corrected with respect to the energy loss and attenuation in the atmospheric overburden, in a similar manner as in the case of the instrumental corrections. The correspondence between the kinetic energy at the top of the instrument and at the top of the atmosphere is illustrated in figure 5.6, in the case of deuterium. The shifting of the energy bins on the deuterons flux introduced by this correction is smaller than in the instrumental case, but in the first energy bins is nevertheless non-negligible.

In order to take into account the attenuation of the deuterons in the atmospheric overburden, similar survival probabilities as in the instrumental correction case have been calculated in the corresponding energy bins, this time considering the propagation through the atmosphere, whose composition is described in the appendix C. Their reciprocal values obtained from averaging the survival probability curves in the energy bins, have to be multiplied by the deuterium flux at TOI, $D_{pri,TOI}$, to obtain the incident flux at the top of the atmosphere, D_{TOA}. The attenuation factors and the estimated 10% systematical error, as in the instrumental case, are presented in the table 5.4.

5.2.3 The D/He_{tot} and D/P Ratios at the TOA

The deuterium flux at the top of the atmosphere, obtained according to relation 5.8 and corrected with respect to attenuation and energy loss in the residual

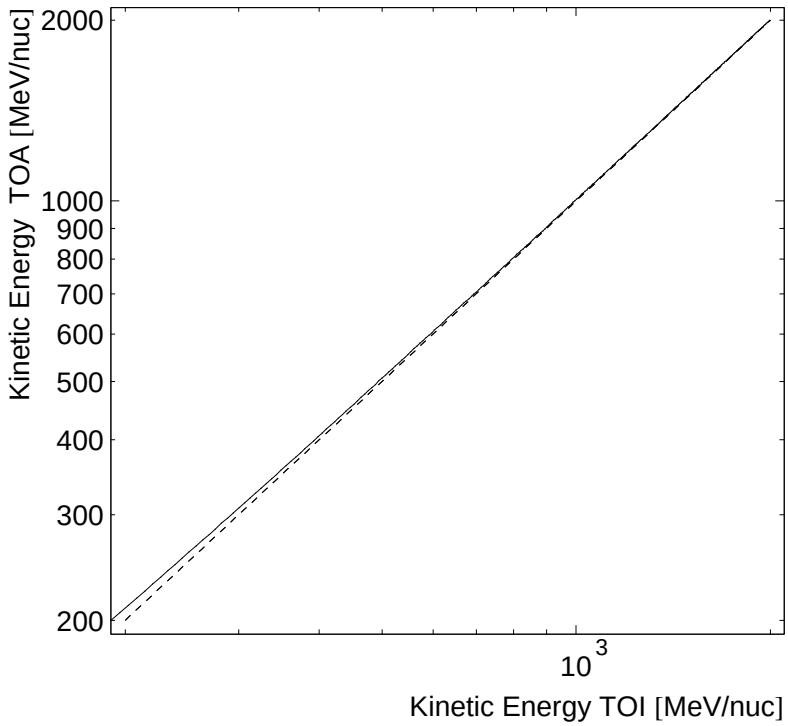

Figure 5.6: Dependence of the kinetic energy per nucleon at the top of the instrument on the same quantity at the top of the atmosphere, in the case of deuterons (solid line), compared with the line of slope 1 (dashed line).

Energy domain TOI (MeV/nuc)	Attenuation factors
241.7 ÷ 430.5	1.1004 ± 0.1100
430.5 ÷ 625.6	1.1043 ± 0.1104
625.6 ÷ 824.7	1.1083 ± 0.1108
824.7 ÷ 1022.1	1.1108 ± 0.1110
1022.1 ÷ 1221.8	1.1119 ± 0.1111
1221.8 ÷ 1421.5	1.1118 ± 0.1111
1421.5 ÷ 1621.3	1.1112 ± 0.1111
1621.3 ÷ 1821.1	1.1108 ± 0.1110

Table 5.4: The attenuation factors due to total inelastic interactions of deuterons with the atmospheric overburden.

atmosphere is presented in the table 5.5.

The fluxes of protons and helium at the top of the atmosphere, already measured with IMAX [62], allow to express now the deuteron-to-proton and deuteron-to-helium ratios. In order to remain consistent with previous measurements, the flux of helium He_{tot} used for calculating the ratio refers to the total flux, namely ${}^3He + {}^4He$. The results are grouped in the tables 5.6 and 5.7.

Energy domain TOA (MeV/nuc)	Mean Energy (MeV/nuc)	$D_{TOA} \pm \sigma_{stat} \pm \sigma'_{syst} - \sigma_{syst}$ $(m^2 \cdot s \cdot sr \cdot GeV \cdot nuc^{-1})^{-1}$
250.8 ÷ 436.7	336.4	37.95 ± 1.19 ± 9.64 − 0.96
436.7 ÷ 631.3	530.5	30.52 ± 1.08 ± 5.65 − 0.54
631.3 ÷ 829.7	726.5	21.73 ± 0.96 ± 3.97 − 0.41
829.7 ÷ 1027.3	926.2	16.21 ± 0.91 ± 2.96 − 0.38
1027.3 ÷ 1226.8	1126.4	13.14 ± 0.83 ± 2.40 − 0.27
1226.8 ÷ 1426.3	1326.2	11.58 ± 0.83 ± 2.09 − 0.27
1426.3 ÷ 1625.9	1525.8	11.03 ± 0.87 ± 1.97 − 0.26
1625.9 ÷ 1825.5	1726.4	10.46 ± 0.88 ± 1.83 − 0.22

Table 5.5: The flux of deuterons at the top of atmosphere. The error σ'_{syst} includes also the error on the atmospheric attenuation correction.

Energy domain TOA (MeV/nuc)	Ratio $\frac{D}{P} \pm \sigma_{stat} \pm \sigma'_{syst} - \sigma_{syst}$
250.8 ÷ 436.7	0.0432 ± 0.0014 ± 0.0118 − 0.0011
436.7 ÷ 631.3	0.0370 ± 0.0013 ± 0.0073 − 0.0006
631.3 ÷ 829.7	0.0301 ± 0.0013 ± 0.0058 − 0.0005
829.7 ÷ 1027.3	0.0257 ± 0.0015 ± 0.0050 − 0.0006
1027.3 ÷ 1226.8	0.0241 ± 0.0015 ± 0.0046 − 0.0005
1226.8 ÷ 1426.3	0.0241 ± 0.0017 ± 0.0406 − 0.0005
1426.3 ÷ 1625.9	0.0260 ± 0.0020 ± 0.0049 − 0.0006
1625.9 ÷ 1825.5	0.0280 ± 0.0024 ± 0.0052 − 0.0006

Table 5.6: The deuteron-to-proton ratio at the top of atmosphere.

Energy domain TOA (MeV/nuc)	Ratio $\frac{D}{He_{tot}} \pm \sigma_{stat} \pm \sigma'_{syst} - \sigma_{syst}$
250.8 ÷ 436.7	0.2247 ± 0.0089 ± 0.0605 − 0.0057
436.7 ÷ 631.3	0.2129 ± 0.0086 ± 0.0437 − 0.0038
631.3 ÷ 829.7	0.1955 ± 0.0091 ± 0.0396 − 0.0037
829.7 ÷ 1027.3	0.1803 ± 0.0107 ± 0.0367 − 0.0042
1027.3 ÷ 1226.8	0.1766 ± 0.0116 ± 0.0356 − 0.0036
1226.8 ÷ 1426.3	0.1890 ± 0.0140 ± 0.0382 − 0.0044
1426.3 ÷ 1625.9	0.2215 ± 0.0179 ± 0.0443 − 0.0052
1625.9 ÷ 1825.5	0.2509 ± 0.02183 ± 0.0494 − 0.0053

Table 5.7: The deuteron-to-helium ratio at the top of atmosphere.

5.2.4 The Ratio $T_{TOI}/^4He_{TOA}$

The tritium nuclei detected by IMAX at the atmospherical depth of 5 $g \cdot cm^{-2}$ are secondary particles produced in the atmosphere mainly as a product of helium interacting with air targets. Considering the measured fluxes of protons at the top of the instrument $P_{tot,TOI}$ and helium at the top of the atmosphere $^4He_{TOA}$ [62], it is now possible to express the ratio triton-to-helium, $T_{TOI}/^4He_{TOA}$ according to the relation:

$$\frac{T_{TOI}}{^4He_{TOA}} = \left.\frac{T}{P}\right|_{TOI} * \frac{P_{tot,TOI}}{^4He_{TOA}} \tag{5.9}$$

where the quantity $\frac{T}{P}|_{TOI}$ has been already presented in table 5.1. The flux of the tritium nuclei at TOI and the ratio $T_{TOI}/^4He_{TOA}$ are presented in the tables 5.8 and 5.9.

The tritium production cross-section for the fragmentation of ^4He on air nuclei can be estimated by using this measured ratio. A specific calculation should be performed by solving propagation equations including the attenuation of both tritium and helium in the atmosphere and their energy loss, as well as considering the flux of heavier nuclei. Therefore, this calculation should also employ the production cross-sections of tritons from the spallation of nuclei with $Z > 2$. These quantities are not well investigated yet and there are important disagreements between the few measurements and models available [90]. Therefore, in the frame of this work these additional calculations have not been performed.

Energy domain TOI (MeV/nuc)	Mean Energy (MeV/nuc)	$T_{TOI} \pm \sigma_{stat} \pm \sigma'_{syst} - \sigma_{syst}$ $(m^2 \cdot s \cdot sr \cdot GeV \cdot nuc^{-1})^{-1}$
241.7 ÷ 430.5	331.0	$6.69 \pm 0.38 \pm 0.86 - 0.10$
430.5 ÷ 625.6	524.1	$4.28 \pm 0.30 \pm 0.55 - 0.06$
625.6 ÷ 824.7	720.9	$2.95 \pm 0.26 \pm 0.38 - 0.05$
824.7 ÷ 1022.1	920.7	$2.15 \pm 0.22 \pm 0.27 - 0.04$
1022.1 ÷ 1221.8	1121.2	$1.69 \pm 0.19 \pm 0.22 - 0.04$
1221.8 ÷ 1421.5	1323.0	$1.54 \pm 0.19 \pm 0.20 - 0.03$
1421.5 ÷ 1621.3	1525.4	$1.57 \pm 0.22 \pm 0.22 - 0.03$
1621.3 ÷ 1821.1	1728.0	$2.25 \pm 0.27 \pm 0.29 - 0.04$

Table 5.8: The flux of tritons at 5 $g \cdot cm^{-2}$ of atmospheric depth. The error σ'_{syst} includes the errors on the proton flux at TOI and on the instrumental correction

Energy domain TOI (MeV/nuc)	Ratio $\frac{T_{TOI}}{^4He_{TOA}} \pm \sigma_{stat} \pm \sigma'_{syst} - \sigma_{syst}$
241.7 ÷ 430.5	$0.0496 \pm 0.0031 \pm 0.0077 - 0.0007$
430.5 ÷ 625.6	$0.0352 \pm 0.0025 \pm 0.0054 - 0.0005$
625.6 ÷ 824.7	$0.0309 \pm 0.0028 \pm 0.0048 - 0.0005$
824.7 ÷ 1022.1	$0.0276 \pm 0.0029 \pm 0.0043 - 0.005$
1022.1 ÷ 1221.8	$0.0260 \pm 0.0029 \pm 0.0041 - 0.0006$
1221.8 ÷ 1421.5	$0.0287 \pm 0.0035 \pm 0.0045 - 0.0005$
1421.5 ÷ 1621.3	$0.0358 \pm 0.0051 \pm 0.0061 - 0.0007$
1621.3 ÷ 1821.1	$0.0612 \pm 0.0074 \pm 0.0096 - 0.0010$

Table 5.9: The ratio of tritons at 5 $g \cdot cm^{-2}$ to ^4He at the top of the atmosphere.

Chapter 6

Conclusions

The balloon-borne cosmic-ray experiment IMAX was flown in 1992 and due to a simultaneous measurement of velocity, rigidity and charge, was able to separate light isotopes in the energy range between 200 and 1800 MeV/nuc. This work describes the analysis of these data in order to obtain the absolute flux of deuterium, the deuteron-to-proton ratio, as well as the deuteron-to-helium and triton-to-helium ratio in the given energy range.

The performances of the individual detectors have been described in detail in the previous chapters as well as the corrections which account for interactions in the instrument and in the residual atmosphere above the balloon, in order to obtain the flux and the ratios at the top of the atmosphere.

Figure 6.1 shows the deuterium flux obtained for this work in comparison to existing data in the literature. All data which are compiled in this figure refer to a solar modulation parameter comparable to the situation when IMAX was flown, estimated to 750 $\pm$ 50 MV [62]. As can be seen within the given errors these measurements agree pretty well (except the one given by Webber [91]) and show a decrease in flux at high energy. These measured fluxes and also the shape of the spectrum follows the theoretical predictions shown on the same plot.

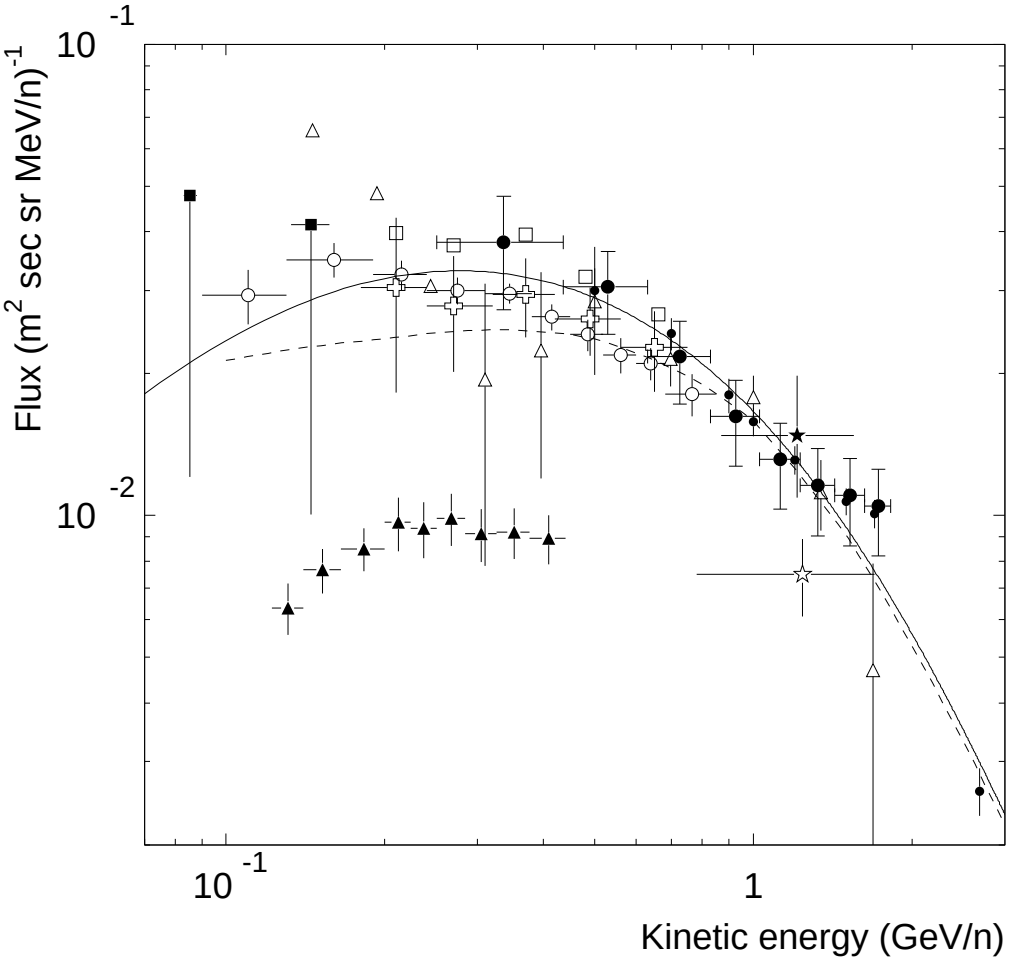

Figure 6.1: Differential energy spectrum of cosmic-ray deuterons measured by IMAX at the top of the atmosphere. The data points are as follows: *filled circles:* IMAX92 (this work), *open cross:* BESS93 [87], *open circles:* AMS98 [54], *open triangles:* CAPRICE94 [26], *open squares:* BESS94 [88], *smaller filled circles:* IMAX92 (deNolfo) [68], *filled star:* Bogomolov75 [13, 15], *opened star:* Bogomolov90 [14, 15], *filled triangles:* Webber89 [91], *filled squares:* Leech78 [55]. The solid line represents the calculated spectrum using the re-acceleration model with a solar modulation parameter of 700 MV [78]. The dashed curve represents the calculated spectrum with a leaky-box model including a solar modulation parameter of 750 MV [92].

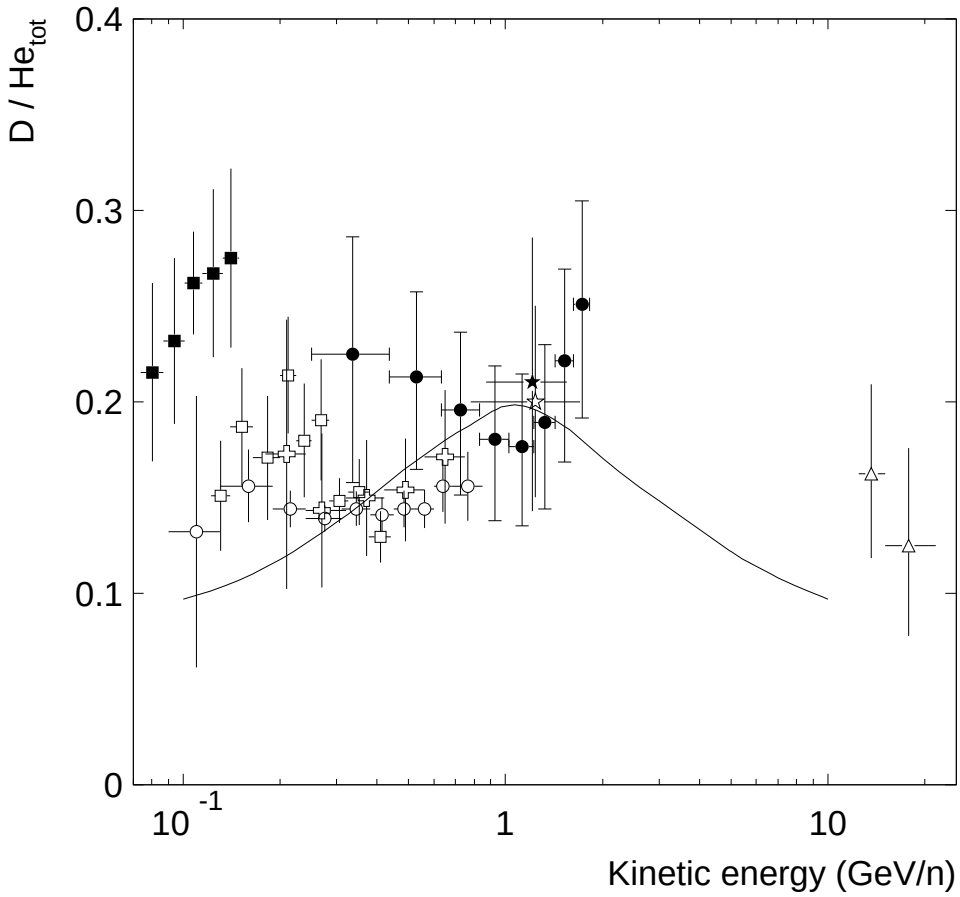

Figure 6.2: D/He_{tot} ratio measured by IMAX at the top of the atmosphere. The data are as follows: *filled circles:* IMAX92 (this work), *open cross:* BESS93 [87], *open circles:* AMS98 [54], *filled star:* Bogomolov75 [13, 15], *opened star:* Bogomolov90 [14, 15], *open triangles:* CAPRICE98 [85], *open squares:* Webber89 [91], *filled squares:* Webber77 [93]. The curve represents the calculated spectrum with a leaky-box model including a solar modulation parameter 750 MV [92].

The D/He ratio is of particular interest since it reflects the total amount of matter traversed by the helium particles. This ratio as obtained from this work is shown in figure 6.2 along with a compilation of other measurements. It can be noticed that these data do not show a clear trend as a function of energy in the covered energy range. They also do not follow the theoretical prediction given by the plotted curve. This calculation is published by Webber [92] and based on the leaky-box propagation model including a solar modulation of 750 MV.

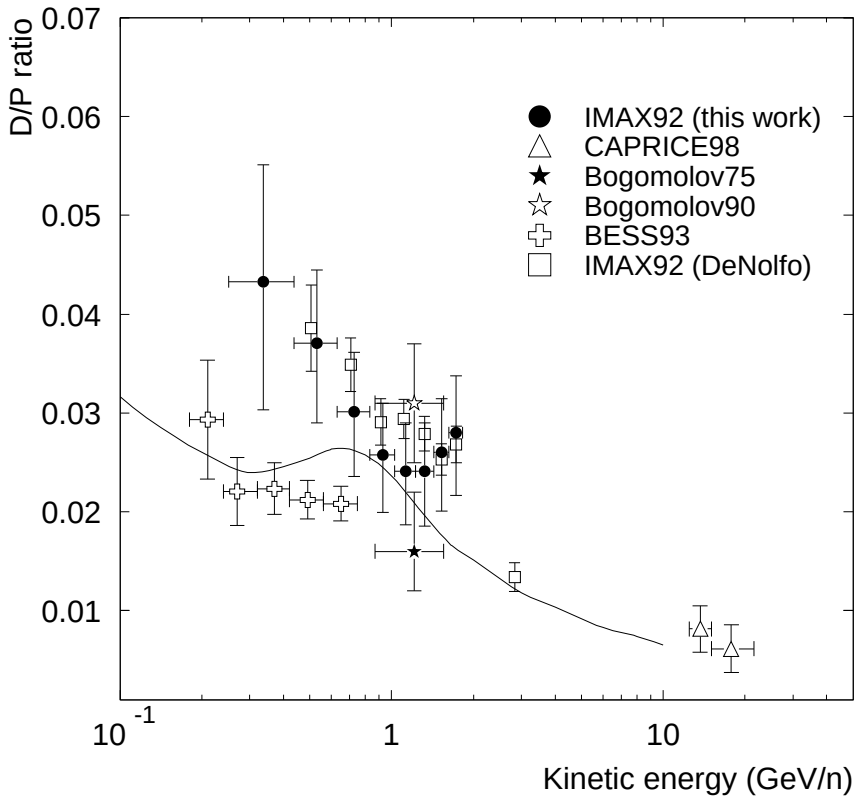

Figure 6.3: D/P ratio measured by IMAX at the top of the atmosphere. The data are as follows: *filled circles:* IMAX92 (this work), *open cross:* BESS93 [87], *filled star:* Bogomolov75 [13, 15], *opened star:* Bogomolov90 [14, 15], *open triangles:* CAPRICE98 [85], *open squares:* IMAX92 (deNolfo) [68]. The curve represents the calculated spectrum using the leaky-box model with a solar modulation parameter of 600 MV [78].

Figure 6.3 shows the D/P ratio provided by this work, together with other measurements. Here again the existing data show a deviation between each other of about 2 σ and it is difficult to determine a clear trend of this ratio as a function of energy. The literature also provides a calculation of this ratio [87] which is shown in the same picture.

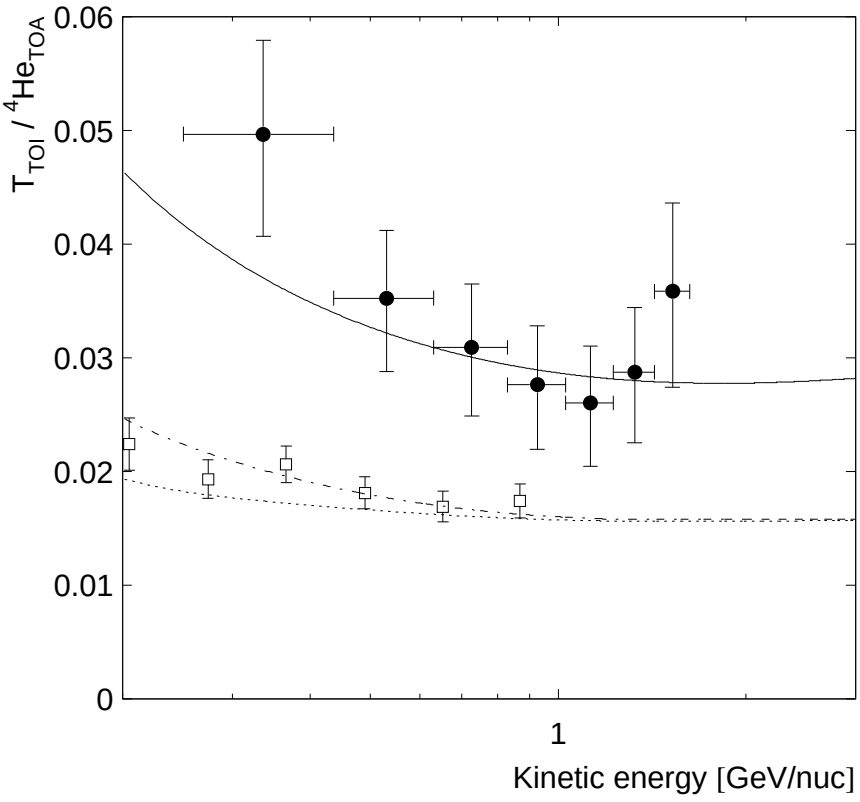

Figure 6.4: $T_{TOI}/{}^4He_{TOA}$ ratio measured by IMAX. Data are as follows: *filled circles:* IMAX92 (this work), *open squares:* BESS98 [66]. The curves represent calculations of this ratio performed by Papini et al. [71] for different atmospheric depths and solar activities as follows: *solid line:* 10 $g \cdot cm^{-2}$ and solar maximum, *dotted-dashed line:* 5 $g \cdot cm^{-2}$ and solar maximum, *dotted line:* 5 $g \cdot cm^{-2}$ and solar minimum.

The ratio $T_{TOI}/{}^4He_{TOA}$ is of particular interest since the amount of tritium measured at the float altitude should reflect the production efficiency mainly from the interaction of the incoming ${}^4He$ particles with the air nuclei. This ratio as obtained in this work is shown in figure 6.4. The only data to which we can compare are those presented by the BESS collaboration [66]. Both instruments flew under conditions of comparable residual atmosphere but with different solar modulation parameters (BESS98 flew close to a solar minimum of $\sim$ 500 MV while IMAX at $\sim$ 750 MV, see also figure E). It can be seen that both data differ considerably between each other (more than 2 σ). Also shown are the theoretical calculations found in the literature [71], for two atmospherical depths: 5 $g \cdot cm^{-2}$ at solar maximum and minimum and 10 $g \cdot cm^{-2}$ at solar maximum. In

the framework of this calculation one can conclude that there are no agreements between our data and the predictions. However one should consider that the calculation includes production cross-sections which are barely known. There are no direct measurements of the most important cross section, ^4He + Air $\longrightarrow$ T + X. The employed cross section in this calculation is based on a scaling to air nuclei from the few available measurements with various targets.

As a conclusion from my work I see that more efforts have to be done for improving the measurement of the ratios, so that they can form a reliable basis for distinguishing between the present theoretical models about the cosmic-rays propagation.

Appendix A

Iterative Procedure for Determining the Rigidity

The iterative fitting procedure applied for the determination of the rigidity is based on successive integrations of the equation of motion 3.4, and aims to minimize the obtained χ^2 of the track by varying the status vector.

The equation 3.4 is numerically integrated starting from the initial position $\vec{r}_0$=$\vec{r}(l_0)$ and thus the next point of the track, after an arbitrary distance Δl, can be calculated as:

$$\vec{r}(l_0 + \Delta l) = \vec{r}\,(l_0) + \frac{1}{2} \cdot \left(\frac{d\vec{r}}{dl}(l_0 + \Delta l) + \frac{d\vec{r}}{dl}(l_0) \right) \cdot \Delta l \tag{A.1}$$

with

$$\frac{d\vec{r}}{dl}(l_0 + \Delta l) = \frac{d\vec{r}}{dl}(l_0) + \frac{d^2\vec{r}}{dl^2}(l_0) \cdot \Delta l. \tag{A.2}$$

Therefore:

$$\vec{r}(l_0 + \Delta l) = \vec{r}\,(l_0) + \frac{d\vec{r}}{dl}(l_0) \cdot \Delta l + \frac{1}{2}\frac{\eta}{c} \left(\frac{d\vec{r}}{dl}\,(l_0) \times \vec{B}\,(\vec{r_0}) \right) \cdot \Delta l^2\,. \tag{A.3}$$

Instead of the vector $d\vec{r}/dl|_{\vec{r}_0}$ it is more convenient to use the angles determined by the projection of the unit vector of the velocity with the XZ and YZ planes. Also, only two initial coordinates are needed for the position vector $\vec{r}_0$ because the z-coordinate can be chosen as the one of a measurement layer. Therefore the status vector used for the numerical integration of the equation of motion is $\vec{\alpha} = (x_0, y_0, (dx/dz)_{\vec{r}_0}, (dy/dz)_{\vec{r}_0}, \eta)$. With this vector and the chosen integration step of $\Delta l = 2\ cm$, points x_i and y_i of the track are calculated at every coordinates z_i of the measurement layers, according to the relation A.3. This allows to compute the χ^2 of the track already presented in section 3.1.2:

$$\chi^2\,(\vec{\alpha}) = \sum_{i=1}^{N_x} \left(\frac{x_i\,(\vec{\alpha}) - x_{mi}}{\sigma(x_{mi})} \right)^2 + \sum_{i=1}^{N_y} \left(\frac{y_i\,(\vec{\alpha}) - y_{mi}}{\sigma(y_{mi})} \right)^2 \tag{A.4}$$

where x_{mi} and y_{mi} represent the measured points in the i-th layer and $N_{x,y}$ the number of hits in the X and Y view, respectively. The position resolution σ varies with respect to the measured points since it varies with the drift path according to figure 3.4.

The goal of the fitting procedure is to find the status vector which minimizes the χ^2 function, which could be done at least in principle by varying all the five parameters for every track until the lowest value of the chi-square is found. However, since this requires a considerable volume of computations, Solmitz and Burkhardt [32] have proposed a minimizing procedure for the $\chi^2(\vec{\alpha})$. The procedure is iterative and is based on a Taylor series expansion of $\chi^2(\vec{\alpha})$ around an initial value $\vec{\alpha_0}$:

$$\chi^2(\vec{\alpha}) = \chi^2(\vec{\alpha_0}) + \sum_{j=1}^{5} \frac{\partial \chi^2}{\partial \alpha_j}(\vec{\alpha_0}) \cdot \Delta\alpha_j + \frac{1}{2} \sum_{j,k=1}^{5} \frac{\partial^2 \chi^2}{\partial \alpha_j \partial \alpha_k}(\vec{\alpha_0}) \cdot \Delta\alpha_j \Delta\alpha_k \quad \text{(A.5)}$$

where :

$$\begin{aligned} \vec{\alpha_0} &= (\alpha_{01}, ..., \alpha_{0j}, ..., \alpha_{05}) \\ \vec{\alpha} &= (\alpha_1, ..., \alpha_j, ..., \alpha_5) \\ \Delta\alpha_j &= \alpha_j - \alpha_{0j} \ . \end{aligned} \quad \text{(A.6)}$$

The condition for minimum is :

$$\frac{\partial \chi^2}{\partial \alpha_i}(\vec{\alpha}) = 0 \ \ \forall i. \quad \text{(A.7)}$$

By applying this condition to the relation A.5, the solution for the minimum becomes:

$$\vec{\alpha} = \vec{\alpha_0} - Z^{-1} \cdot V \quad \text{(A.8)}$$

where the matrixes V and Z are defined as:

$$\begin{aligned} V &= \left(\frac{\partial \chi^2}{\partial \alpha_l}(\vec{\alpha_0}) \right)_{l=1,5} \\ Z &= \left(\frac{\partial^2 \chi^2}{\partial \alpha_l \partial \alpha_j}(\vec{\alpha_0}) \right)_{l,j=1,5} . \end{aligned} \quad \text{(A.9)}$$

The advantage of using this minimization method is its iterative nature. The procedure starts with a first estimate $\vec{\alpha_0}$ of the status vector, from which a new estimate is evaluated according to the relation A.8. The so-determined status vector is only an approximation of the real minimum because higher order terms of the series A.5 are neglected. However, if one uses this value for the calculation of a new minimizing status vector, the new value will represent a better approximation of the searched minimum. This procedure stops when the difference in the components of two consecutive status vectors is lower than the following values:

$$\vec{\alpha} - \vec{\alpha_0} < (10\ \mu m, 10\ \mu m, 0.1\ mrad, 0.1\ mrad, 3 \cdot 10^{-3}\ GV^{-1}) \ . \quad \text{(A.10)}$$

The status vector which starts the iterations is chosen by performing a straight track fitting from which only the coordinates of this track in the first measurement layer are saved. Accordingly, $\vec{\alpha_0}$ will be $(x_1, y_1, (dx/dz)_1, (dy/dz)_1, 0.005GV^{-1})$. After each iteration the status vector components will be replaced by a better deflection and better calculated coordinates of the track in the first layer therefore the notation refers also to subsequent iterations.

According to the χ^2 from the relation A.4, one gets for elements of the one-dimensional matrix V:

$$\left(\frac{\partial\chi^2}{\partial\alpha_l}(\vec{\alpha_0})\right)_{l=1,5} = 2\sum_{i=1}^{N_x}\frac{x_i - x_{mi}}{\sigma^2(x_{mi})}\cdot\frac{\partial x_i}{\partial\alpha_l}(\vec{\alpha_0}) + 2\sum_{i=1}^{N_y}\frac{y_i - y_{mi}}{\sigma^2(y_{mi})}\cdot\frac{\partial y_i}{\partial\alpha_l}(\vec{\alpha_0}). \quad \text{(A.11)}$$

An analogue derivation for equation A.9, neglecting second order terms, yields for the elements of matrix Z:

$$\left(\frac{\partial^2\chi^2}{\partial\alpha_l\partial\alpha_j}(\vec{\alpha_0})\right)_{l,j=1,5} = 2\left[\sum_{i=1}^{N_x}\frac{1}{\sigma^2(x_{mi})}\frac{\partial x_i}{\partial\alpha_l}\frac{\partial x_i}{\partial\alpha_j}(\vec{\alpha_0}) + \sum_{i=1}^{N_y}\frac{1}{\sigma^2(y_{mi})}\frac{\partial y_i}{\partial\alpha_l}\frac{\partial y_i}{\partial\alpha_j}(\vec{\alpha_0})\right] \quad \text{(A.12)}$$

The explicit values of the partial derivatives which appear in the equation A.11 and equation A.12 are presented in the following table:

Index l	α_l	$\partial x_i/\partial\alpha_l$	$\partial y_i/\partial\alpha_l$
1	x_1	1	0
2	y_1	0	1
3	$(dx/dz)_1$	$z_i - z_1$	0
4	$(dy/dz)_1$	0	$z_i - z_1$
5	η	$\frac{x_i - x_1 - (z_i - z_1)(dx/dz)_1}{\eta}$	$\frac{y_i - y_1 - (z_i - z_1)(dy/dz)_1}{\eta}$

Table A.1: Partial derivatives for the elements of matrixes Z and V

Appendix B

Simulation-related Plots

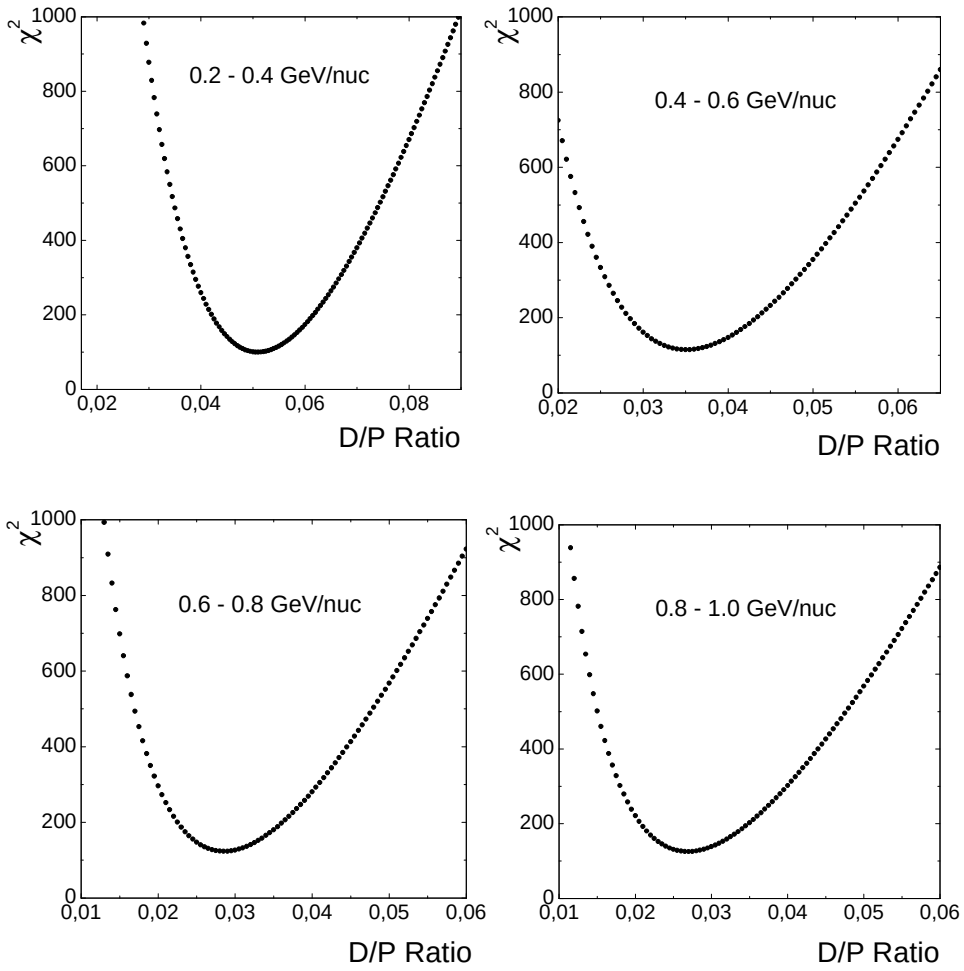

Figure B.1: The χ^2 dependency on the ratio D/P of the simulated mass histograms for the energy range $0.2 \div 1.0$ GeV/nuc.

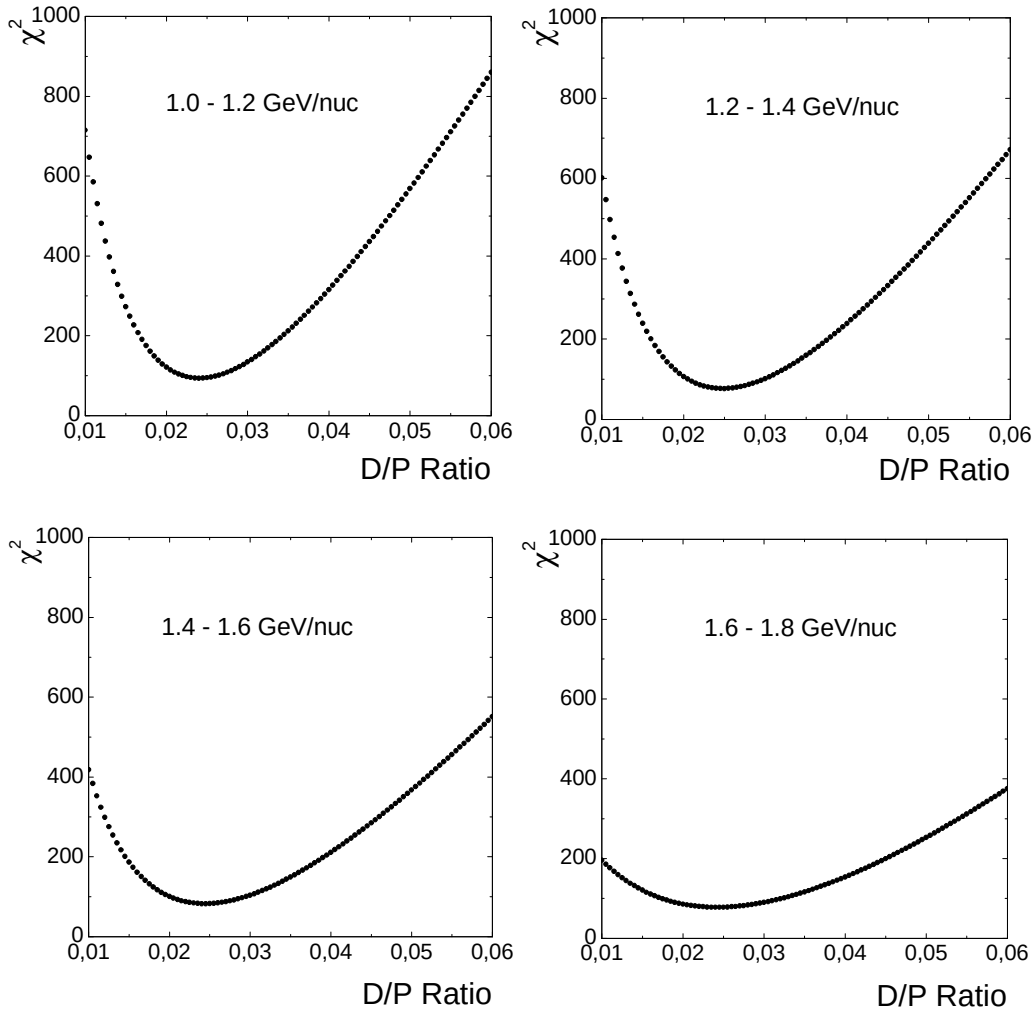

Figure B.2: The χ^2 dependency on the ratio D/P of the simulated mass histograms for the energy range $1.0 \div 1.8$ GeV/nuc.

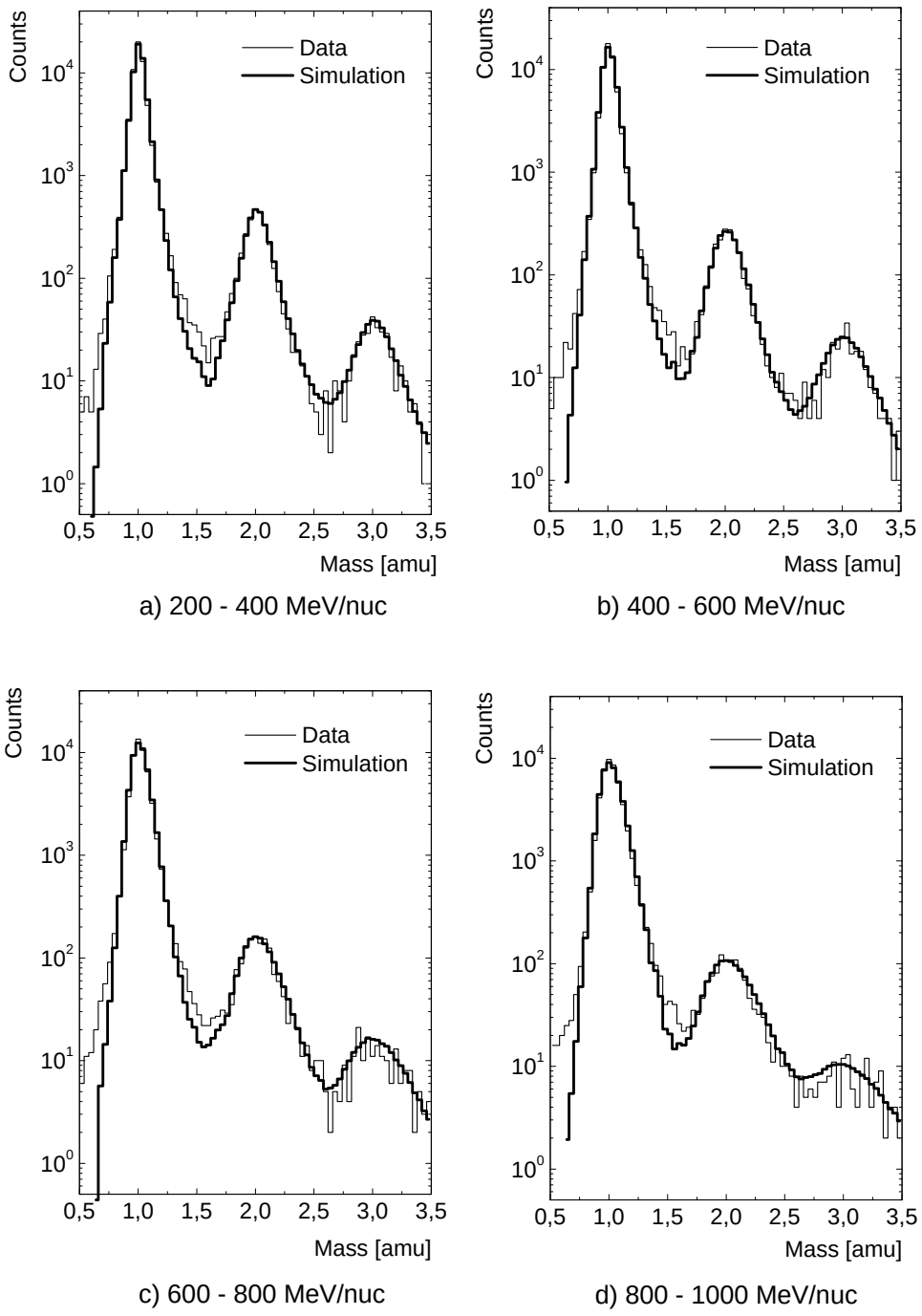

Figure B.3: The measured and simulated mass histograms using deterioration factors for the energy range $200 \div 1000$ MeV/nuc.

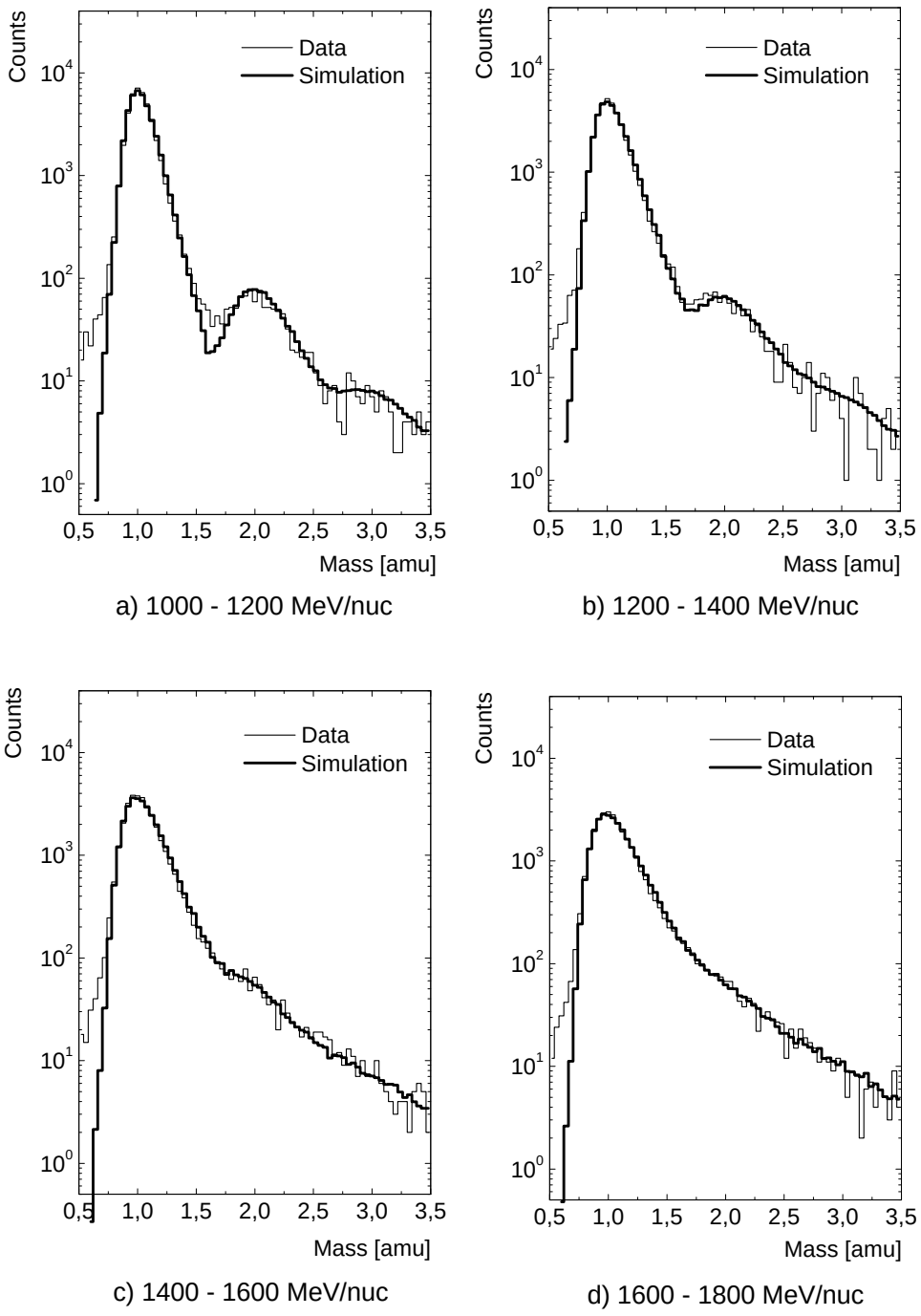

Figure B.4: The measured and simulated mass histograms using deterioration factors for the energy range $1000 \div 1800\ MeV/nuc$.

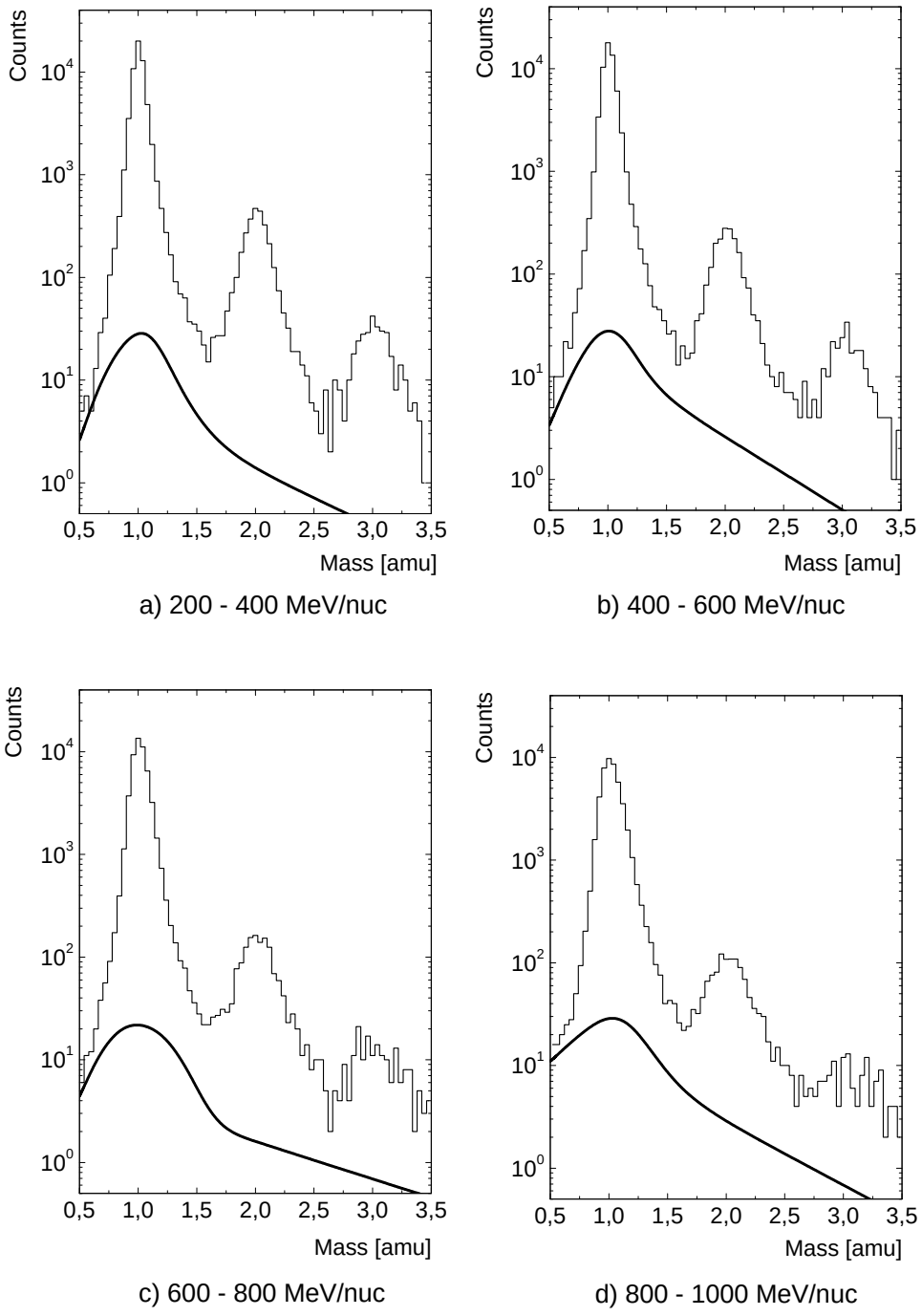

Figure B.5: Background shapes (thick line) superimposed on the measured mass distributions for the energy range $200 \div 1000\ MeV/nuc$.

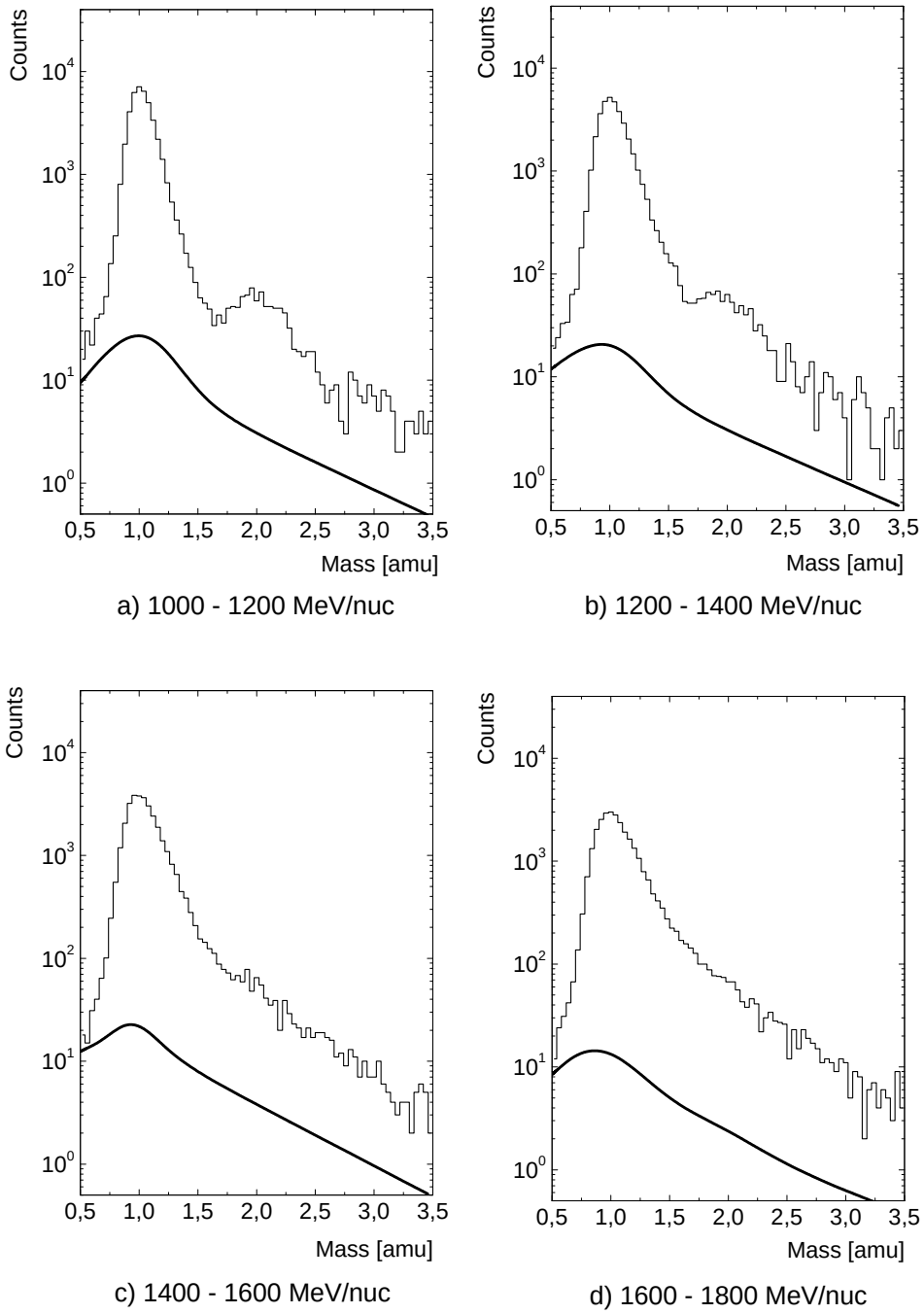

Figure B.6: Background shapes (thick line) superimposed on the measured mass distributions for the energy range $1000 \div 1800\ MeV/nuc$.

Appendix C

IMAX Detector Grammages

The isotopic ratios in the instrument have to be corrected for interactions by taking into account the atmosphere and the IMAX detector materials and thicknesses. Table C.1 lists the materials accounted for in this analysis, from the top of the atmosphere to the bottom-TOF. The materials are broken down into major chemical components. In the last column it is presented the vertical path length in g/cm^2, calculated from the material thickness and density.

In order to approximate the atmosphere, 5.04 g/cm^2 consisting of 78.5% nitrogen, 21.0% oxygen and 0.5% argon have been considered. This atmospheric depth corresponds to the most probable zenith angle detected by IMAX, which amounts to 7° and to an averaged atmospheric depth of 5 $g \cdot cm^{-2}$ during the experiment [72].

The spreader aluminium bar from which the payload itself was suspended is averaged at 0.88 g/cm^2 spread over the top of the instrument (TOI). The plastic scintillator materials are treated as polystyrene and the aerogel Cherenkov radiators are treated as SiO_2. The total vertical path length from the top of the atmosphere to the bottom TOF is 23 g/cm^2 of which 17.08 g/cm^2 is the IMAX payload. The middle of the instrument (MOI) is defined as the top of the tracking system for the purpose of calculating the average energy of a particle as it travels from the top-TOF to the bottom-TOF. The total IMAX vertical path length from the middle of the instrument to the top is 9.95 g/cm^2.

	Material	Symbol	A	Density $[g/cm^3]$	Thickness [cm]	Vertical Path $[g/cm^2]$
Atmosphere	Air	N	14.01			3.925
		O	16.00			1.05
		Ar	39.95			0.025
Spreader bar	Aluminium	Al	26.98	2.70		0.88
Gatorfoam		C_{11}	12.01	0.15	1.00	0.15
		H_{11}	1.00	0.01	1.00	0.01
		N	14.01	0.02	1.00	0.02
Dome	Aluminium	Al	26.98	2.70	0.23	0.62
Top TOF	BC-420	C	12.01	0.95	1.00	0.95
		H	1.00	0.08	1.00	0.08
C1 radiator	Teflon	C	12.01	0.52	2.06	1.07
		F	19.00	1.64	2.06	3.38
C1 walls	Aluminium	Al	26.98	2.70	0.10	0.27
S1 scintillator	BC-400	C	12.01	0.95	1.27	1.21
		H	1.00	0.08	1.27	0.10
S1 walls	Aluminium	Al	26.98	2.70	0.10	0.27
C3 radiator	Aerogel	Si	28.09	0.10	9.00	0.86
		O_2	16.00	0.11	9.00	0.98
C3 walls	Aluminium	Al	26.98	2.70	0.29	0.78
DC Copper	Copper	Cu	63.55	8.96	0.01	0.13
DC Mylar	Mylar	C_{10}	12.01	0.87	0.05	0.04
		H_8	1.00	0.06	0.05	0.00
		O_4	16.00	0.46	0.05	0.02
DC Tungsten	Tungsten	W	183.85	19.30	0.01	0.14
DC CO_2		C	12.01	$5.40{\cdot}10^{-4}$	66.00	$3.56{\cdot}10^{-4}$
		O_2	16.00	$1.44{\cdot}10^{-3}$	66.00	$9.49{\cdot}10^{-2}$
MWPC Mylar	Mylar	C_{10}	12.01	0.87	0.03	0.02
		H_8	1.00	0.06	0.03	0.00
		O_4	16.00	0.46	0.03	0.01
MWPC Steel		Fe	56.85	7.87	$6.56{\cdot}10^{-3}$	0.05
MWPC Argon		Ar	39.95	$1.78{\cdot}10^{-3}$	28.80	$5.13{\cdot}10^{-2}$
C2 radiator	Aerogel	Si	28.09	0.10	9.00	0.86
		O_2	16.00	0.11	9.00	0.98
C2 walls	Aluminium	Al	26.98	2.70	0.29	0.78
S2 scintillator	BC-408	C	12.01	0.95	1.78	1.69
		H	1.00	0.08	1.78	0.14
S2 walls	Aluminium	Al	26.98	2.70	0.32	0.86
Bottom TOF	BC-420	C	12.01	0.95	1.00	0.95
		H	1.00	0.08	1.00	0.08
IMAX N_2 Atmosphere	Nitrogen	N_2	14.01	$1.25{\cdot}10^{-3}$	132.50	$1.66{\cdot}10^{-1}$

Table C.1: IMAX Detector Grammages.

Appendix D

Cross-Section Compilation

The LaRC model to parameterize the total reaction cross section of ion collisions, being a semi-empirical model, contains several terms that need to be tuned for each type of reaction, based on the available measurements. In the original papers only few of the reactions of interest in this work were investigated and therefore one needs additional compilations of data in order to test the model for other reactions.

In this appendix are grouped measurements of the total reaction cross section available in the literature about the collisions involving protons, deuterons and tritons as projectiles on the existent nuclei targets in the instrument and the atmosphere. The tables D.1 to D.8 show the collected cross-section values, their corresponding energies together with the references. These values are plotted in figures D.1 to D.5 as a function of the projectile kinetic energy per nucleon. The superimposed curves on each of those plots, apart from figure D.1a, are obtained from the LaRC universal parametrization method.

The data for the total inelastic reactions of the type proton-nucleus are relatively abundant in the literature and therefore the LaRC model could be checked for all of the nuclei presented in table C.1. The total inelastic cross section for the process ${}^1H+{}^1H$ could not be described satisfactorily by the LaRC model and therefore another parametrization has been chosen [80], shown in figure D.1a. This parametrization is of the form:

$$\begin{array}{lcll} \sigma_{pp}^{ine}(E_p) & = & 0 & E_p \leq 0.3GeV \\ \sigma_{pp}^{ine}(E_p) & = & \frac{\sigma_{pp}^{hil}}{1+2.62\cdot 10^{-3}\cdot E_p^{-C_p}} & 0.3GeV < E_p < 3GeV \\ \sigma_{pp}^{ine}(E_p) & = & \sigma_{pp}^{hil} & E_p \geq 3GeV \end{array} \tag{D.1}$$

where σ_{pp}^{hil} is defined according to [42]:

$$\sigma_{pp}^{hil} = 32.2\left[1 + 0.0273 \cdot U + 0.01 \cdot U^2 \cdot \Theta(U)\right] \tag{D.2}$$

and the rest of appearing terms are:

$$\begin{aligned} \Theta(U) &= \begin{cases} 0 & U < 0 \\ 1 & U \geq 0 \end{cases} \\ U(E_p) &= \ln\left(\frac{E_p}{200}\right) \\ C_p(E_p) &= 17.9 + 13.8 \cdot \ln E_p + 4.41 \cdot \ln^2 E_p. \end{aligned} \tag{D.3}$$

Collision type	Reference and symbol	Kinetic energy (MeV/n)	σ_R (mb)
$^1H + ^1H$	[25] ♦	410	3.9 ± 2.1
		460	6 ± -
		489	4.6 ± 2
		500	6.9 ± 2
		528	6 ± 3
		540	9.1 ± 2.1
		560	8.87 ± 0.66
		580	12.6 ± 2.1
		600	13.6 ± 2.1
		620	15.6 ± 2.1
		640	16.8 ± 2.1
		657	18 ± -
		660	18.4 ± 1.5
		810	24.3 ± 1.5
		941	23 ± 3
		$18{\cdot}10^3$	29.8 ± 1.4
	[39] ◊	650	16.7 ± 0.6
	[45] ★	1000	20.3 ± 3
	[5] △	$23.5{\cdot}10^3$	32.3 ± 0.4
	[18] ○	$60{\cdot}10^3$	31.7 ± 0.8

Table D.1: Total reaction cross sections reference list for proton-proton collisions.

Collision type	Reference and symbol	Kinetic energy (MeV/n)	σ_R (mb)
$^{1}H + ^{12}C$	[23] ◁	9.88	195 ± 47
		10.4	434 ± 58
		10.72	318 ± 61
		13.7	380 ± 43
		19.4	401 ± 24
	[59] □	40	371 ± 11
		49.5	345 ± 13
		60.8	310 ± 13
	[46] ▲	65	295.5 ± 7.7
	[50] ▷	99.1	245 ± 7
	[76] ○	231	215.2 ± 5.4
		345	218.8 ± 5.1
		464	228.5 ± 5.1
		552	229.2 ± 5.4
	[2] ★	847	258 ± 6
	[8] ■	860	209 ± 22
	[45] ▼	1000	258 ± 17
	[35] ●	1091	257 ± 7
		3365	265 ± 15
	[27] ▽	705	232.5 ± 13.08
		959	247 ± 13.93
		1091	241 ± 13.59
		1225	247 ± 13.93
		1499	248 ± 13.98
		1778	245 ± 13.81
		2062	247 ± 13.93
	[12] ◊	5000	248 ± 2
		6000	249 ± 2
		7000	256 ± 2
		8000	251 ± 2
		9000	250 ± 2
	[34] △	$20{\cdot}10^3$	247 ± 2
		$40{\cdot}10^3$	246 ± 2
		$60{\cdot}10^3$	252 ± 4

Table D.2: Total reaction cross sections reference list for proton projectiles on carbon target.

Collision type	Reference and symbol	Kinetic energy (MeV/n)	σ_R (mb)
$^{1}H + {}^{14}N$	[21] ■	22.9	533 ± 39
		28.9	474 ± 26
		35.9	446 ± 19
		43	408 ± 18
		49	368 ± 21
$^{1}H + {}^{16}O$	[8] ◊	13.1	373 ± 20
		231	295 ± 12
		345	282 ± 14
		464	288 ± 15
		552	290 ± 15
	[46] □	65	365 ± 15
	[20] ♦	26.6	517 ± 14
		25.6	524 ± 18
		24.1	553 ± 14
		20.9	524 ± 16
		18.8	531 ± 18
	[45] ■	1000	296 ± 50
$^{1}H + {}^{19}F$	[8] ♦	24.9	676 ± 22
		27.4	654 ± 20
		30.4	626 ± 19
		34.3	596 ± 18
		36.9	579 ± 18
		39.3	552 ± 18
		43.3	532 ± 18
		46.3	522 ± 20
	[12] ◊	$50{\cdot}10^3$	355 ± 5
		$60{\cdot}10^3$	350 ± 5
		$70{\cdot}10^3$	348 ± 5
		$80{\cdot}10^3$	347 ± 5
		$90{\cdot}10^3$	358 ± 5
	[50] ★	99.1	353 ± 10

Table D.3: Total reaction cross sections reference list for proton projectiles on ^{14}N, ^{16}O and ^{19}F targets.

Collision type	Reference and symbol	Kinetic energy (MeV/n)	σ_R (mb)
$^{1}H + ^{27}Al$	[8] ▷	8.8	674 ± 45
		9.9	656 ± 28
		10.1	704 ± 28
		10.4	610 ± 26
		860	394 ± 10
	[2] ◁	847	432 ± 10
		1091	473 ± 15
	[76] ○	234	399.6 ± 44.5
		348	402.1 ± 35.6
		466	423.9 ± 22.3
		554	433.2 ± 13.4
	[59] ■	40	645 ± 35
		60	499 ± 27
	[56] ★	29	775 ± 37
	[27] ▼	705	418 ± 23.6
		959	435 ± 24.5
		1091	434 ± 24.5
		1225	443 ± 25
		1499	441 ± 24.9
		1778	438 ± 24.7
		2062	439 ± 24.8
	[57] ▲	24.8	733 ± 20
		30.4	709 ± 18
		36.9	651 ± 16
		43.2	615 ± 16
		46.3	600 ± 17
	[50] ♦	99.7	430 ± 12.04
	[34] ◇	$20{\cdot}10^3$	447 ± 4
		$40{\cdot}10^3$	441 ± 6
		$60{\cdot}10^3$	455 ± 7
	[12] □	$50{\cdot}10^3$	445 ± 4
		$60{\cdot}10^3$	457 ± 4
		$70{\cdot}10^3$	453 ± 4
		$80{\cdot}10^3$	458 ± 4
		$90{\cdot}10^3$	465 ± 4

Table D.4: Total reaction cross sections reference list for proton projectiles on ^{27}Al target.

Collision type	Reference and symbol	Kinetic energy (MeV/n)	σ_R (mb)
$^{1}H + ^{28}Si$	[57] □	24.7	771 ± 24
		30.5	720 ± 22
		36.8	685 ± 20
		43.2	643 ± 19
		47.8	626 ± 19
	[46] ◊	65.5	554.7 ± 15.2
$^{1}H + ^{56}Fe$	[8] □	8.9	680 ± 50
		9.7	760 ± 31
		10	747 ± 47
		10.7	833 ± 29
		11.2	828 ± 29
		34	902 ± 72
		98	747 ± 21
		180	662 ± 19
		230	685 ± 13
		345	679 ± 12
		463	701 ± 13
		552	702 ± 12
	[12] ◊	5000	752 ± 7
		6000	766 ± 7
		7000	757 ± 7
		8000	763 ± 7
		9000	755 ± 7
	[59] ♦	40	991 ± 43
		60.8	899 ± 32
	[58] ■	20.8	1118 ± 34
		24.8	1101 ± 25
		29.7	1055 ± 24
		34.8	1014 ± 29
		39.7	1005 ± 29
		44.9	925 ± 21
		47.8	903 ± 32

Table D.5: Total reaction cross sections reference list for proton projectiles on ^{28}Si and ^{56}Fe target.

Collision type	Reference and symbol	Kinetic energy (MeV/n)	σ_R (mb)
$^{1}H + {}^{40}Ar$	[21] ◊	22.9	1015 ± 36
		28.9	995 ± 34
		35.9	964 ± 31
		42.9	926 ± 19
		46.9	875 ± 22
	[6] ■	1000	570 ± 70
$^{1}H + {}^{63}Cu$	[8] □	8.8	735 ± 30
		9.5	740 ± 32
		10.2	798 ± 31
		10.9	853 ± 28
		28	1024 ± 35
		77	746 ± 21
		95	774 ± 22
		113	751 ± 25
		133	779 ± 23
		134	752 ± 68
		185	746 ± 75
		225	768 ± 17
		290	717 ± 72
		860	728 ± 17
	[50] ♦	99	835 ± 23
	[73] ■	16.4	955 ± 64
	[12] ▲	5000	818 ± 8
		6000	828 ± 7
		7000	840 ± 7
		8000	836 ± 7
		9000	835 ± 7
	[76] ▼	548	777 ± 17
		459	775 ± 17
		340	751 ± 17
		225	761 ± 17
	[34] ★	$20{\cdot}10^3$	794 ± 9
		$30{\cdot}10^3$	811 ± 9
		$40{\cdot}10^3$	794 ± 10
		$50{\cdot}10^3$	806 ± 10
		$60{\cdot}10^3$	812 ± 13

Table D.6: Total reaction cross sections reference list for proton projectiles on ^{40}Ar and ^{63}Cu target.

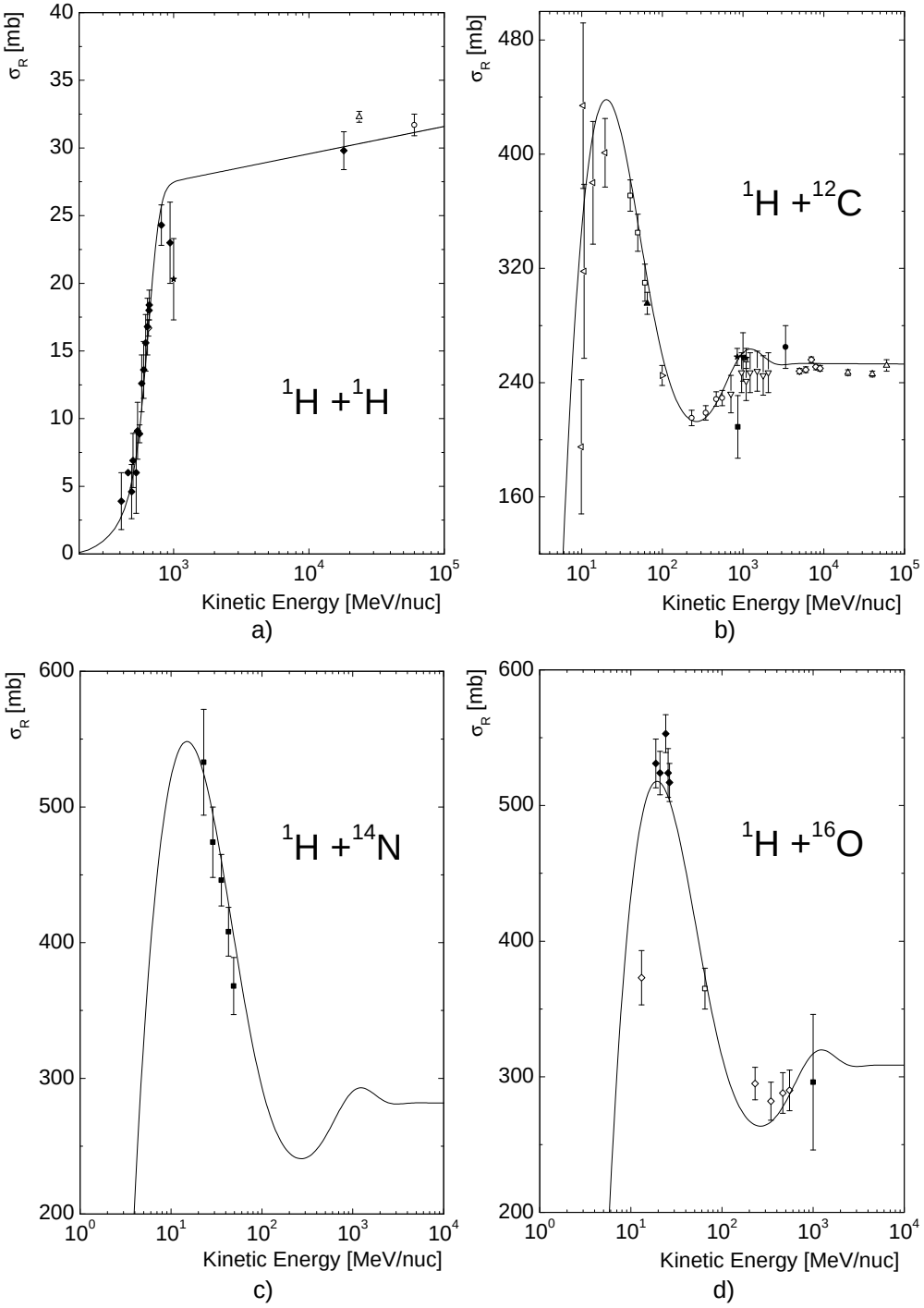

Figure D.1: Total reaction cross-section for ^{1}H projectiles on ^{1}H,^{12}C,^{14}N and ^{16}O targets. The curves are obtained with the LaRC model, except for a), where a parametrization of Tan and Ng has been used [80].

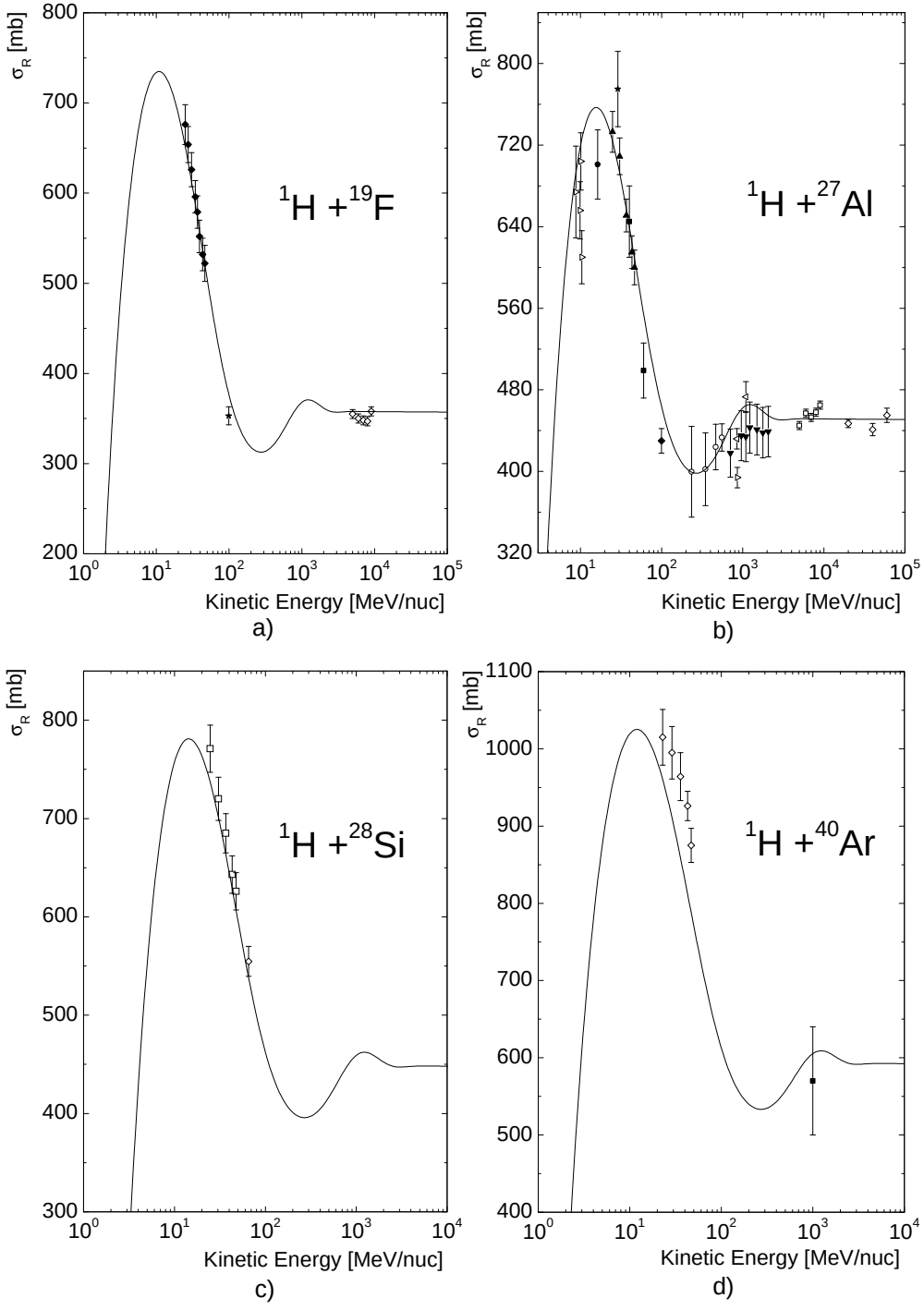

Figure D.2: Total reaction cross-section for ^{1}H projectiles on ^{19}F,^{27}Al,^{28}Si and ^{40}Ar targets. The curves are obtained from the LaRC model.

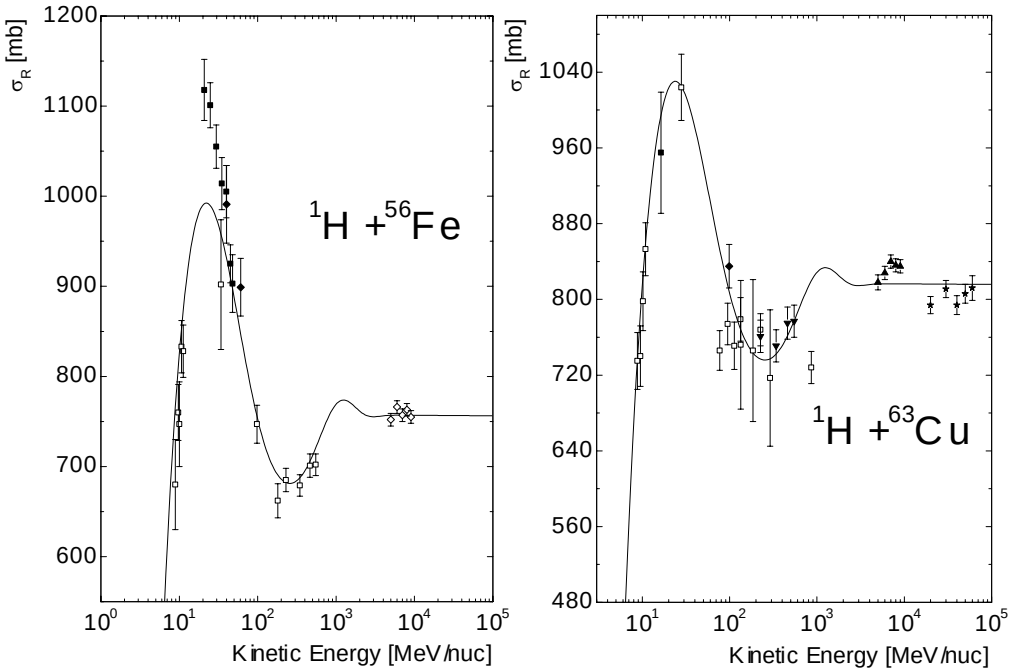

Figure D.3: Total reaction cross-sections for ^{1}H projectiles on ^{56}Fe and ^{63}Cu targets. The curves are obtained with the LaRC model.

Among the nuclei type presented in table C.1, only total reaction cross section measurements for collisions of the type deuteron-proton and deuteron-carbon in the relevant energy range for this analysis are available, presented in table D.7. In the case of a carbon target (figure D.4), the LaRC model describes very approximatively the low energy domain, but in the high energy case the agreement becomes better. For the rest of the collisions d + X, only the target charge and atomic number are allowed to vary while the parameters of the LaRC model are considered constant. There are no measurements available for other targets to test if this approach describes correctly the data or represents only an approximation.

For the case of triton-nucleus collisions, measurements of the total reaction cross section in the energy range of interest are not available. There are only two values for the total cross section in the case of triton-proton collision, which are shown in figure D.5 and table D.8. The targets for which there are no data available are treated as in the deuterium case. In addition, to overcome the lack of measurements, it is accustomed to use the data of the isobar ^{3}He. The differences within the LaRC model between the two cases, ^{3}H and ^{3}He, shown in figure D.5, are not significant for the energy domain studied in this analysis and thus the agreements with the measurements might have a certain relevance.

Collision type	Reference and symbol	Kinetic energy (MeV/n)	σ_R (mb)
$^2H + ^1H$	[19] ∘	22.9	150 ± 12
		24.9	148 ± 11
		26.1	153 ± 12
		27.1	139 ± 9
		28.8	142 ± 9
		30.1	141 ± 9
		31.9	133 ± 9
		33.9	130 ± 8
		35.9	127 ± 7
		37.8	125 ± 7
		39.5	119 ± 7
		42	126 ± 7
		44	121 ± 6
		46	120 ± 6
	[49] △	457.5	55.3 ± 0.9
		534.5	58 ± 1
		610.5	64.7 ±
		680.5	69.7 ± 1
		779	70.6 ± 1
		817.5	70.5 ± 0.9
		899	73.2 ± 0.9
		976.5	74 ± 1
		1076	73.3 ± 1
		1122.5	74.8 ± 1.1
$^2H + ^{12}C$	[3] ▼	37.9	836 ± 24
		65.5	678 ± 15
		97.4	600 ± 17
	[24] ■	650	346 ± 9
	[86] ♦	1000	459 ± 19
	[47] ★	870	411 ± 21
		2100	426 ± 22
	[35] △	3365	400 ± 20
	[38] □	3400	380 ± 20

Table D.7: Total reaction cross sections reference list for deuterium projectiles on proton and carbon targets.

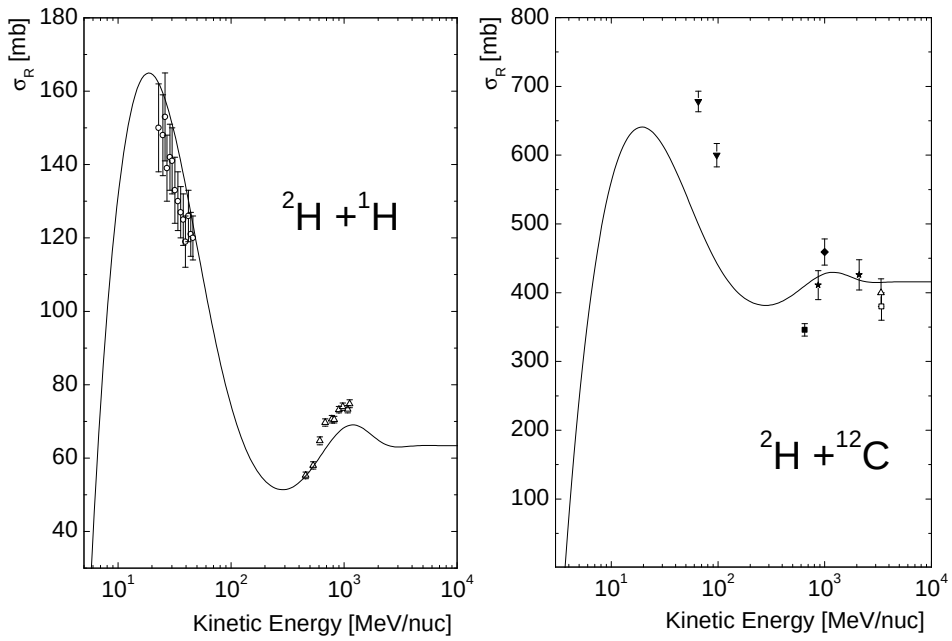

Figure D.4: Total reaction cross sections for deuterium projectiles on proton and carbon targets. The curves are obtained with the LaRC model.

Collision type	Reference and symbol	Kinetic energy (MeV/n)	Total σ (mb)
$^{3}\mathrm{H} + {}^{1}\mathrm{H}$	[10] •	318	85.7 $\pm$ 2.2
	[1] □	967	111.4 $\pm$ 5.67
$^{3}\mathrm{He} + {}^{1}\mathrm{H}$	[11] ■	975	125.2 $\pm$ 6.43
	[29] ★	3360	118 $\pm$ 6.02
$^{3}\mathrm{He} + {}^{12}\mathrm{C}$	[79] ◊	790	550 $\pm$ 5
$^{3}\mathrm{He} + {}^{27}\mathrm{Al}$	[79] ▲	790	850 $\pm$ 9

Table D.8: Total cross sections reference list for ^{3}H and ^{3}He projectiles on proton, carbon and aluminium targets.

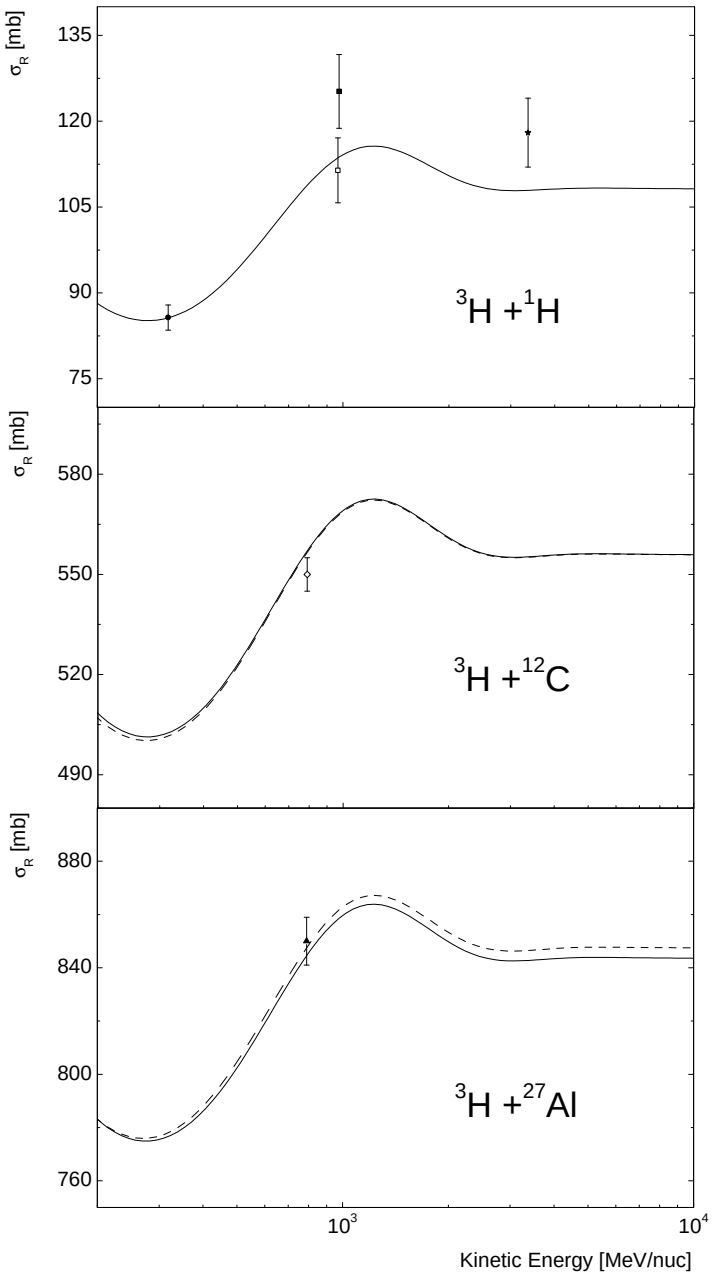

Figure D.5: Total cross sections for ^3H and ^3He projectiles on proton, carbon and aluminium targets (see table D.8 for references). The curves are the total reaction cross sections obtained from the LaRC model for ^3H (full line) and ^3He (dashed line).

Appendix E

Climax Neutron Monitor Flux

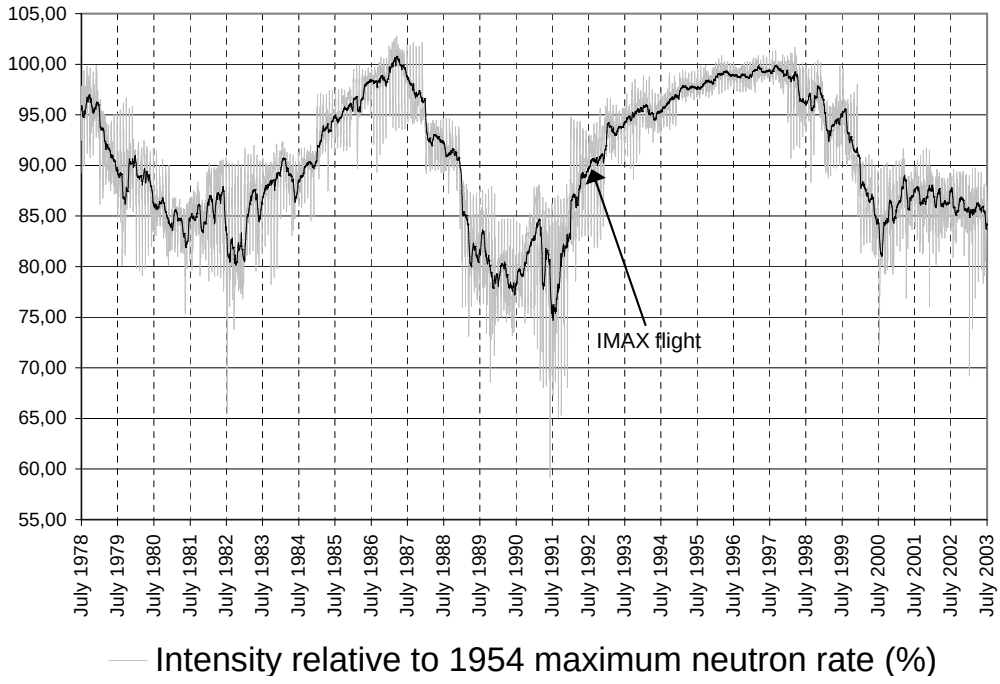

Figure E.1: Climax Neutron Monitor Flux (Courtesy of the National Science Foundation Grant ATM-9912341, University of Chicago). The shaded regions represents the daily fluctuations while the dark line represents a monthly moving average. The neutron rate is negatively correlated with the solar activity and solar modulation parameter.

Bibliography

[1] Abdullin, S.K., et al., 1989, *Cross-Sections of Tritium Interactions with Protons and H-3 P Elastic Scattering at 5 GeV/c*, Yadernaya Fizika, 49, 169

[2] Afonasiev, V. F., et al., 1988, Yadernaya Fizika, 47, 1656

[3] Auce, A., et al., 1996, *Reaction Cross-Sections for 38, 65, and 97 Mev Deuterons on Targets from Be-9 to Pb-208*, Physical Review C, 53, 2919

[4] Allison J., 1993, *Multiquadratic Radial Basis Functions for Representing Multidimensional High Energy Physics Data*, Computational Physics Communications, 77-377, 395

[5] Amaldi, U., et al., 1973, *The Energy Dependence of the Proton Proton Total Cross-Section for Center-Of-Mass Energies Between 23 and 53 GeV*, Physics Letters B, 44, 112

[6] Bakanov, L.V., et al., 1983, *Proton + Ar-40 Reaction Cross-Section at 1GeV*, Journal of Physics, G9, L43-L46

[7] Barlow, R. J., 1989, *Statistics: A Guide to the Use of Statistical Methods in the Physical Sciences*, John Wiley, New York

[8] Bauhoff, W., 1986, *Tables of Reaction and Total Cross Sections for Proton-Nucleus Scattering Below 1 GeV*, Atomic Data and Nuclear Data Tables 35, 429-427

[9] Bethe, H. A., 1953, *Molière's Theory of Multiple Scattering*, Physical Review 89, 1256

[10] Blinov, A.V., et al., 1982, *Study of Differential Cross-Sections for the Reactions H-3(P, N)He-3 and H-3(P, P)H-3 at the Triton Momentum of 2.5-GeV/c*, Yadernaya Fizika, 35, 523

[11] Blinov A.V., et al., 1985, *Study of the Mechanism of the He-3 P —¿ P P D Reaction At He-3 Momentum of 5-GeV/c*, Yadernaya Fizika, 41, 1440

[12] Bobchenko, B. M., et al., 1979, *Measurement of Total Inelastic Cross Sections for Interaction of Protons with Nuclei in the Momentum Range from 5 to 9 GeV/c*, Soviet Journal of Nuclear Physics, 30(6)

[13] Bogomolov, E. A., et al., 1979, *A Stratospheric Magnetic Spectrometer Investigation of the Singly Charged Component Spectra and Composition of the Primary and Secondary Cosmic Radiation*, Proceedings 16$^{\text{th}}$ International Cosmic Ray Conference (ICRC 79), Kyoto 1, 330

[14] Bogomolov, E. A., et al., 1995, *The Deuterium Cosmic Ray Intensity from Balloon Measurement in Energy Range 0.8-1.8 GeV/nucl.*, Proceedings 24$^{\text{th}}$ International Cosmic Ray Conference (ICRC 95), Rome 2, 598

[15] Bogomolov, E. A., et al., 2002, *Antiprotons and Deuterons in the Galactic Cosmic Rays*, 18$^{\text{th}}$ Europeans Cosmic Rays Symposium, Moscow, OG1.1

[16] Brandt, S., 1997, *Statistical and Computational Methods in Data Analysis*, Springer Verlag, New York

[17] Bremmerich, M., 1992, *Simulation der Elektronendrift in hexagonalen Driftkammerzelllen und experimenteller Test eines Prototyps*, Diplomarbeit, Universität Siegen

[18] Bromberg, C., et al., 1977, *Cross-Sections and Charged Particle Multiplicities in Pi+ P and P P Collisions at 60-GeV/c*, Physical Review D, 15, 64

[19] Carlson, R.F., et al., 1973, *Proton-Deuteron Total Reaction Cross-Sections in the Energy Range (20-50) MeV*, Lettere al Nuovo Cimento, 8, 319

[20] Carlson, R.F., et al., 1975, *Proton Total Reaction Cross Sections For the Doubly Magic Nuclei O-16,Ca-40 and Pb-208 in the Energy Range 20-50 MeV*, Physical Review C, Nuclear Physics, 12, 1167

[21] Carlson, R.F., et al., 1985, *Measurements of Proton Total Reaction Cross Sections for 6Li, 7Li, 14N, 20Ne and 40Ar between 23 and 49 Mev*, Nuclear Physics, Section A, 445, 57

[22] Christian, P., 1991, *Test einer Driftkammer mit hexagonaler Zellstruktur im homogenen Magnetfeld*, Diplomarbeit, Universität Siegen

[23] Dicello J.F., Igo G., 1970, *Proton Total Reaction Cross Sections in the 10-20 MeV Range-Calcium-40 and Carbon-12*, Physical Review C, 2, 488

[24] Dutton, L.M.C., et al., 1965, Physics Letters, 16, 331

[25] Flaminio, V., et al., 1984, *Compilation of cross sections*, CERN-HERA 84-01

[26] Finetti, N., *PhD Thesis*, Universita degli Studi di Perugia, Italy

[27] Gachurin, V.V., et al., 1985, *Measurement of Total Inelastic Cross-Sections of the Interaction of Protons and Pi+ Mesons on Nuclei in the Momentum Range from 1.35-GeV/c to 3.75-GeV/c*, ITEP-59-1985

[28] Gaisser, T.K., 1990, *Cosmic Rays and Particle Physics*, Cambridge University Press

[29] Glagolev, V.V., et al., 1993 *Cross-Sections of the Interactions of He Nuclei with Protons*, Zeitschrift fuer Physik C, 60, 421

[30] Golden, R.L., et al., 1978, *A magnetic spectrometer for cosmic ray studies*, Nuclear Instruments and Methods in Physics Research, 148, 179

[31] Golden, R.L., et al., 1979, Physical Review Letters, 43, 1196

[32] Golden, R.L., et al., 1991, *Performance of a Ballon-Borne Magnet Spectrometer*, Nuclear Instruments and Methods in Physics Research, A306, 366

[33] Göbel, H., 2001, *Bestimmung des Isotopenverhltnisses von $^{10}Be/^{9}Be$ in der kosmischen Teilchenstrahlung mit dem Ballonexperiment ISOMAX im Energiebereich von 263 - 1032 MeV/Nukleon*, Dissertation, Universität Siegen

[34] Gorin, V. F., et al., 1973, *Nuclear Absorption Cross-Sections for Pions, Kaons, Protons, and Anti-Protons in the Momentum Range 6-60 GeV/c*, Yadernaya Fizika, 18, 336

[35] Grigalashvili, N.S., et al., 1988, *Inelastic Cross-Sections and Multiplicities of Secondary Charged Particles Produced in Collisions of Relativistic Nuclei with Carbon and Tantalum at 2.3-A-GeV/c and 4.2-A-GeV/c*, Yadernaya Fizika, 48, 476

[36] D.E. Groom et al., 2000, Review of Particle Physics, The European Physical Journal, C15, 1

[37] Grupen C., 1999, *Particles Detectors*, Cambridge University Press

[38] Gulkanyan G.R., et al., 1989, YERE-1150-27-89

[39] Guzhavin, V.M., et al., 1964, Zhurnal Eksperimental'noi i Teoreticheskoi Fiziki, 46, 1245

[40] Hagiwara, K, et al., 2002, *Particle Data Group*, Physical Review D66, 010001, 206

[41] Hams, T., 2002, *Bestimmung der Isotopenverhltnisse für die Elemente Lithium, Beryllium und Bor im Energiebereich bis zu 1.3 GeV/Nukleon in der galaktischen kosmischen Teilchenstrahlung mit dem Ballonflug-Experiment ISOMAX1998*, Dissertation, Universität Siegen

[42] Hillas, A.M., 1979, ‚Proceedings 16$^{\text{th}}$ International Cosmic Ray Conference (ICRC 79), Kyoto, 6-13

[43] Hof, M., et al., 1994, *Performance of drift chambers in a magnetic rigidity spectrometer*, Nuclear Instruments and Methods in Physics Research, A345, 561-569

[44] Hof, M., 1996, *Messung von Antiprotonen in der kosmischen Strahlung in einem Energiebereich von 3,7 bis 19 GeV mit dem Ballonflugexperiment MASS2*, Dissertation, Universität Siegen

[45] Igo, G, et al., 1967, Nuclear Physics, B3, 181

[46] Ingemarsson, A, et al., 1999, *Reaction Cross Sections for 65 MeV Protons on Targets from 9Be to 208Pb*, Nuclear Physics A, 653, 341

[47] Jaros, J., et al., 1978, *Nucleus-nucleus total cross sections for light nuclei at 1.55 and 2.89 GeV/c per nucleon*, Physical review C, 18, 5

[48] John, S., et al., 1993, *Geometric Model from Microscopic Theory for Nuclear Absorption*, NASA Technical Paper, 3324

[49] Katayama, N., et al., 1985, *Measurement of D P Cross-Sections in the Momentum Range 2 GeV/c - 3.7 GeV/c*, Nuclear Physics A, 438, 685

[50] Kirkby P., Link W.T., 1966, *Faraday-Cup Measurement of Proton Total Reaction Cross Sections at 100 MeV*, Canadian Journal of Physics, 44, 1847-62

[51] Kremer, J., 1995, *Testmessungen an Spurdetektor und am Flugzeitsystem des ISOMAX Experimentes*, Diplomarbeit, Universität Siegen

[52] Lacy J.L., Lindsey R.S., 1973, Nuclear Instruments and Methods, 119, 483

[53] Labrador, A.W., *Measurement of the Galactic Cosmic Ray Antiproton Flux from 0.25 GeV to 3.11 GeV with the Isotope Matter Antimatter Experiment (IMAX)*, Ph.D. Thesis, California Institue of Technology

[54] Lamanna, G., *Measurement of deuteron spectra in Low Earth Orbit with the Alpha Magnetic Spectrometer*, Proceedings of ICRC 2001: 1614

[55] Leech H.V. and O'Gallagher J.J., 1978, *The Isotopic Composition of Cosmic-Ray Helium from 123 to 279 MeV per Nucleon: A New Measurement and Analysis*, The Astrophysical Journal, 221:1110-1123

[56] Makino, M.Q., et al., 1964, *Total Reaction Cross Sections For 29 MeV Protons*, Nuclear Physics, 50, 145

[57] McGill W.F., et al., 1974, *Measurements of the Proton Total Reaction Cross Section for Light Nuclei Between 20 and 48 MeV*, Physical Review C, 10, 2237

[58] McCamis, R.H., et al., 1986, *A Study of Proton Total Reaction Cross Sections for Several Medium-Mass Nuclei Between 20 and 48 MeV*, Canadian Journal of Physics, 64, 685

[59] Menet, J.J., et al., 1971, *Total-Reaction-Cross Section Measurements for 30-60-Mev Protons and the Imaginary Optical Potential*, Physical Review C, Nuclear Physics, 4, 1114

[60] Menn, W., 1991, *Messung von Teilchenbahnen in einem von hochenergetischen Schwerionen mit einer mit CO_2 gefllten Driftkammer*, Diplomarbeit, Universität Siegen

[61] Menn, W., 1995, *Messung der Antiprotonen in der kosmischen Strahlung mit dem IMAX-Experiment in einem Energiebereich von 0.25-3.2 GeV/Nukleon*, Dissertation, Universität Siegen

[62] Menn, W., et al., 2000, *The Absolute Flux of Protons and Helium at the Top of the Atmosphere Using IMAX*, The Astrophysical Journal 533, Issue 1, 281

[63] Mitchell, J.W., et al., 1993, *The Isotope Matter-Anitmatter Experiment Time-of-Flight System*, Proceedings 23$^{\text{rd}}$ International Cosmic Rays Conference, Calgary, 2, 627

[64] Mitchell, J.W., et al., 1996, *Measurement of 0.253.2 GeV Antiprotons in the Cosmic Radiation* Physical Review Letters, 76, 3057

[65] Montanet, L., et al., 1994, Physical Review, D50, 1173

[66] Myers, Z.D., et al., 2003, *Detecting* ^{3}H *with the BESS Spectrometer*, Proceedings of ICRC 2003: 1793

[67] Neuhaus, J., 1989, *Messung von Teilchenspuren in einem Schwerionen-Experiment mit einer Drift-Influenzkammer*, Diplomarbeit, Universität Siegen

[68] de Nolfo, G. A., et al., 2000, *A measurement of Cosmic Ray Deuterium from 0.5-2.9 GeV/nucleon*, AIP Conference Proceedings, 528

[69] *Numerical Recipes in Fortran*, Cambridge University Press, 1993

[70] Papini P., Grimani C., Stephens S.A., 1996, *An estimate of the secondary-proton spectrum at small atmospheric depths*, Il Nuovo Cimento, Vol.19 C, 367

[71] Papini, P., et al., 1993, *Spectra of* Helium^3 *and Tritium at Small Atmospheric Depths*, Proceedings 23$^{\text{rd}}$ International Cosmic Rays Conference, Calgary, 1, 499

[72] Pfeifer, C., 1995, *Die Wechselwirkung einfallender Protonen der kosmischen Strahlung in der Erdatmosphere im Hinblick auf sekundre Antiprotonenproduktion*, Dissertation, Universität Siegen

[73] Pollock R.E., Schrank G., 1965, *Proton Total Reaction Cross Sections at 16.4 MeV*, Physical Review B, 140, 575

[74] Reimer, O., 1995, *Messung der leichten Isotope in der kosmischen Strahlung mit dem IMAX-Experiment in einem Energiebereich von* $0,2-1,8$ *GeV/Nukleon*, Dissertation, Universität Siegen

[75] Reimer, O., et al., 1998, *The Cosmic-Ray 3He/ 4He Ratio from 200 MeV per Nucleon to 3.7 GeV per Nucleon*, The Astrophysical Journal, 496, 490-502

[76] Renberg, P.U., et al., 1972, *Reaction Cross Sections for Protons in the Energy Range 220-570 MeV*, Nuclear Physics A, 183, 81

[77] Sauli F., Peisert A., 1984, CERN-Report, 84-08

[78] Seo E.S., Ptuskin V.S., 1994, *Stochastic Reacceleration of Cosmic Rays in the Interstellar Medium*, The Astrophysical Journal, 431:705-714

[79] Tanihata, I., et al., 1985, *Measurements of Interaction Cross Sections and Radii of He Isotopes*, Physics Letters B, 160, 380

[80] Tan L.C., Ng L.K., 1983, *Parametrization of Hadron Inclusiv Cross-Section in p-p Collisions Extended to Very Low Energies*, Journal of Physics, G9:1289-1308

[81] Tripathi, R.K., et al., 1997, *Universal Parametrization of Absorption Cross Sections*, NASA Technical Paper, 3621

[82] Tripathi, R.K., et al., 1999, *Universal Parametrization of Absorption Cross Sections for Light Systems*, NASA Technical Paper, TP-1999-209726

[83] Vannuccini, E., et al., 2001, *An estimate of the secondary ^2H spectrum produced by cosmic rays in the atmosphere*, Proceedings of ICRC 2001 : 4181

[84] Vannuccini, E., et al., 2003, *The secondary deuterium spectrum at small atmospheric depths*, Proceedings of ICRC 2003: 2077

[85] Vannuccini, E., et al., 2003, *Measurement of the Deuterium Flux in the Kinetic Energy Range 12-22 GeV/n with the CAPRICE98 Experiment*, Proceedings of ICRC 2003: 1801

[86] Viryasov, N.M., et al., 1991, *Pi-Meson Production in the Interaction of Deuterons at 1-GeV per Nucleon with Carbon and Beryllium Extended Targets*, Joint Institute for Nuclear Research, JINR-P1-91-455

[87] Wang, J.Z., et al., 2002, *Measurement of Cosmic-Ray Hydrogen and Helium and their Isotopic Composition with the BESS Experiment* The Astrophysical Journal, 564:244-259

[88] Wang, J.Z., et al., 2001, *Isotopic Measurements of Cosmic-Rays hydrogen and helium during 1997 solar minimum*, Prepared for 26th International Cosmic Ray Conference (ICRC 99), Salt Lake City, Utah, 17-25 Aug 1999

[89] Wang, J.Z., et al., 1999, *Measurement of Cosmic Ray H and He Isotopes in a Series of Annual Balloon Flights*, Prepared for 26th International Cosmic Ray Conference (ICRC 99), Salt Lake City, Utah, 17-25 Aug 1999

[90] Webber, W.R., 1990, *New Measurements of the Cross Sections of ^4He into ^2H and ^3He and their implication for ^2H and ^3He Production in Cosmic Rays*, American Institute of Physics, Conf. Proc. 203, 294

[91] Webber, W.R., et al., 1991, *A Measurement of the Cosmic-Ray ^2H and ^3He Spectra and $^2H/^4He$ and $^3He/^4He$ Ratios in 1989*, The Astrophysical Journal, 380:230-234

[92] Webber, W.R., 1997, *^3He and ^2H Measurement and what they tell us about Cosmic Ray Propagation in the Galaxy*, Adv. Space Res., Vol. 19, No. 5, 755-758

[93] Webber W.R., Yushak S.M., 1983, *A Measurement of the Energy Spectra and Relative Abundance of the Cosmic-Ray H and He Isotopes Over a Broad Energy Range*, The Astrophysical Journal, 275:391-404

Acknowledgements

This place is surely too small to express in words my good thoughts to all the people that left in a way or another their fingerprint on this work.

First and foremost, my thanks go to my research coordinator, prof. dr. Manfred Simon. During the five years which I spent in his research group, including the work for the degree Diplom Physiker, he helped me invaluably through his guidance, his patience and his experienced advices. The numerous discussions about the scientific aspects of my thesis as well as about other collateral aspects that are important ingredients of an appropriate working atmosphere were always enlightening and essential in the progress of the work. I would also like to thank him for the opportunity to hold exercise classes, which were a very stimulating experience for me.

Dr. Wolfgang Menn is a key-piece of this work, because of his rich experience with balloon experiments and with data analysis. He followed my steps carefully and provided me with many invaluable suggestions. A very peaceful working atmosphere was also assured by my office colleague, Dr. Alexander Molnar. I benefited a lot from his theoretician formation, by having numerous discussions about many theoretical aspects connected to my work and to physics, in general.

Fortunately for me, in the same time I commenced the work for this thesis, Dr. Massimo Boscherini joined our group as a graduate student. His warm and friendly company has helped me to overcome easier the inherent difficulties of studying and living abroad.

Apart of that, all of the former or actual group members that I had the pleasure to meet or to work with during the last five years contributed to my actual scientist formation. I would mention here Dr. Michael Hof, Dr. Thomas Hams, Dr. Holger Göbel and Bernd Dostal.

A special thank has to go to Elena Vannuccini and Paolo Papini from the INFN Firenze for providing the "technical assistance" in using their model about the atmospheric deuteron production.

I have to express my gratitude to prof. dr. Hans Dieter Dahmen for the decisive help at the beginning of my study period in Siegen but also for many useful advices during my graduation. Prof. dr. Paul Sterian has inspired me during the studies in Romania with more self-confidence for which I will remain grateful to him.

I thank to my parents for making me being as I am and for choosing in the key moments of my evolution the right balance between persuasion and freedom of choice. Florina Constantinescu's life-long friendship was a ground base in many moments during the years and I am also grateful to her parents for the unconditioned support.

My final gratitude goes to PG, for the strength to resist two years of almost daily phone conversations.